Acta Geodaetica et Geophysica Hungarica

VOLUME 33, NUMBER 1, 1998

**PROCEEDINGS OF THE
INTERNATIONAL BEACON SATELLITE SYMPOSIUM 97**
SOPRON, 30 JUNE–5 JULY 1997
HUNGARY
PART II

GUEST EDITORS
P BENCZE and R LEITINGER

AGG 33 (1) 1–153 (1998) HU ISSN 1217–8977

ACTA GEODAETICA ET GEOPHYSICA HUNGARICA
A Quarterly Journal of the Hungarian Academy of Sciences

Acta Geodaetica et Geophysica Hungarica (AGG) publishes original reports and reviews on geodesy and geophysics in English.

AGG is published in yearly volumes of four issues by

AKADÉMIAI KIADÓ
H-1117 Budapest, Prielle K. u. 19–35

Manuscripts and editorial correspondence should be addressed to

AGG Editorial Office
Geodetical and Geophysical Research Institute
H-9401 Sopron, P.O. Box 5
Phone: (36-99) 314-290
Fax: (36-99) 313-267
E-mail: actagg@ggki.hu
Internet: http://www.ggki.hu/agg/

Subscription information

Orders should be addressed to

AKADÉMIAI KIADÓ
H-1519 Budapest, P.O. Box 245

REPORT DOCUMENTATION PAGE

Form Approved OMB No. 0704-0188

1. AGENCY USE ONLY (Leave blank)	2. REPORT DATE	3. REPORT TYPE AND DATES COVERED
	20 June 1998	Conference Proceedings

4. TITLE AND SUBTITLE Proceedings of the International Beacon Satellite symposium 98, Acta Geodaetica et Geoiphysica Hungarica, v. 33, no. 1, 1998.	5. FUNDING NUMBERS F6170897W0094
6. AUTHOR(S) P. Bencza and R. Leitinger, Guest Editors	
7. PERFORMING ORGANIZATION NAME(S) AND ADDRESS(ES) Institute of Meteorology and Geophysics Karl Franzens University of Graz Graz Austria	8. PERFORMING ORGANIZATION REPORT NUMBER N/A
9. SPONSORING/MONITORING AGENCY NAME(S) AND ADDRESS(ES) EOARD PSC 802 BOX 14 FPO 09499-0200	10. SPONSORING/MONITORING AGENCY REPORT NUMBER CSP 97-1046
11. SUPPLEMENTARY NOTES	
12a. DISTRIBUTION/AVAILABILITY STATEMENT Approved for public release; distribution is unlimited.	12b. DISTRIBUTION CODE A

13. ABSTRACT (Maximum 200 words)

The Final Proceedings for International Beacon Satellite Symposium 1997, 30 June 1997 - 5 July 1997. This is an interdisciplinary conference. Topics include Ionospheric Tomography, Electron Content, Ionospheric Models, Scintillation Modelling, Radio Wave Propagation.

14. SUBJECT TERMS Space Science, Tomography, Radio Propagation	15. NUMBER OF PAGES 153
	16. PRICE CODE N/A

17. SECURITY CLASSIFICATION OF REPORT	18. SECURITY CLASSIFICATION OF THIS PAGE	19, SECURITY CLASSIFICATION OF ABSTRACT	20. LIMITATION OF ABSTRACT
UNCLASSIFIED	UNCLASSIFIED	UNCLASSIFIED	UL

Proceedings of the International Beacon Satellite Symposium 97
Sopron, 30 June – 5 July, 1997
Hungary

Part II

Editors

P Bencze and R Leitinger

Programme Committee

R Leitinger Chairman
J A Klobuchar
P V S Rama Rao
P Bencze

Local Organizing Committee

P Bencze
L Bányai
K Kovács
F Märcz
G Sátori

CONTENTS

Acta Geod. Geoph. Hung., Vol. 33(1), pp. 3–8 (1998)

NIGHTTIME ENHANCEMENTS IN IEC AT LOW LATITUDES — A STUDY WITH REFERENCE TO F REGION DYNAMICS

D S V V D PRASAD[1], P V S RAMA RAO[1], P SRI RAM[1], K NIRANJAN[1]

The nighttime enhancement (NTE) in the ionospheric electron content (IEC) are observed over Waltair (17.7°N) and Calcutta (22°N), when the equatorial F region rises to higher altitudes during the post-sunset hours over Kodaikanal (10°N). No significant enhancement is seen at either of the stations if the altitude of the F region near the equatorial region is confined to lower altitudes. In addition to the altitude rise at the equatorial region, an earlier post-sunset reversal in the meridional neutral wind direction from poleward to equatorward also seems to be a requisite condition for the enhancements in IEC to occur at off-equatorial regions. The observed features are discussed in the light of the F region dynamics.

Keywords: equatorial F region height; ionosonde; ionospheric electron content; meridional neutral wind; satellite beacon

1. Introduction

Sudden increase in the upward drift of plasma at the equator during post-sunset hours is found to be responsible for many ionospheric phenomena observed in the equatorial anomaly region during late evening hours, viz., the occurrence of irregularities, NTE in IEC. During the period of sunspot maximum years substantial redevelopment of anomaly in the late evening hours is observed after the initial diurnal decay in IEC in the after-noon hours. It is known that the vertical transport of plasma perpendicular to the magnetic field-lines is governed primarily by $\mathbf{E} \times \mathbf{B}$ drifts and along the field-lines at the equator by diffusion and meridional neutral winds giving rise to a normal F region anomaly during daytime (Martyn 1955, Appleton 1960). However, at sub-tropical latitudes, a post-sunset increase in the ionisation is often observed, which is also basically due to the equatorial plasma transport governed by $\mathbf{E} \times \mathbf{B}$ and neutral winds (Anderson and Klobuchar 1983, Balan and Bailey 1995). The latitudinal extent of such enhancements in IEC is attributed to the maximum height rise of the F layer over the magnetic equator as well as to the direction of meridional neutral winds (Garg et al. 1983, Balan and Bailey 1995). A possible qualitative explanation regarding the strength and the latitudinal extent of the post-sunset movement of ionisation anomaly under the influence of $\mathbf{E} \times \mathbf{B}$ drift and meridional wind is presented in this paper.

[1]Department of Physics, Andhra University, Visakhapatnam 530 003, India

2. Data

IEC data obtained at a low latitude station, Waltair (17.7°N, 83.3°E) during October 1989 – November 1990 (average Rz = 150) is used to study the characteristics of the nighttime enhancements. Simultaneous data on IEC obtained at Waltair and Calcutta, an anomaly crest station (22.6°N, 88.4°E) during October–November 1989 (Rz = 150) is used to study the latitudinal extent of the nighttime enhancements (NTE) in IEC. The ionosonde data obtained at Kodaikanal (10°N) is used to evaluate the variation in the F region altitude over the magnetic equator, for three typical days considered in the present study. The meridional neutral wind velocities are computed from the F region height variations at Kodaikanal (10°N) and Ahmedabad (23°N).

3. Results

3.1 Association of NTE in IEC over Waltair with equatorial F layer height variations

The IEC variations at Waltair quite often show significant nighttime enhancements during the post-sunset hours centred around 2200 hrs IST particularly during the high sunspot activity periods. Since the occurrence and the magnitude of these enhancements in IEC show large day-to-day variability, a case study is made in an effort to identify the possible mechanisms responsible for such increases. Typical nocturnal plots showing the IEC variations with nighttime enhancement (16th May, 1990) and without nighttime enhancement (31st May, 1990) are presented in Fig. 1a. On 16th May 1990, the nighttime increase in IEC started from 2100 hours, while on 31st May 1990, the IEC decreased monotonically without any nighttime enhancement. The corresponding h'F variations at Kodaikanal (Fig. 1b) on 16th May show that (when the NTE in IEC is present at Waltair), there is a sharp rise in the F region altitude at the magnetic equator starting from 1800 hrs IST attaining a peak altitude of 570 km between 2000–2100 hrs IST. But, on 31st May 1990, the F region attained a lower altitude of 450 km at the magnetic equator (when there is no NTE in IEC at Waltair). Also, the sharp rise in the altitude of the F region seen on 16th May is absent on 31st May 1990.

3.2 Latitudinal extent of NTE in IEC and the F layer height variations at the equator

To specify the strength of the NTE in IEC, an index basing on the extent of the enhancements, is determined by taking the ratio between the post-sunset peak value of the enhanced IEC at Calcutta and at Waltair. The IEC variations during three typical days (10th, 3rd and 4th November, 1989) with different values of NTE index are presented in Fig 2. On 10th November, 1989 (Fig. 2a), the NTE index is found to be 2.67 where the post-sunset increase in IEC is more significant at Calcutta (with peak occurrence around 2100 hrs IST), whereas the increase is less and occurred an hour later (at 2200 hrs IST) at Waltair. On 3rd November, 1989

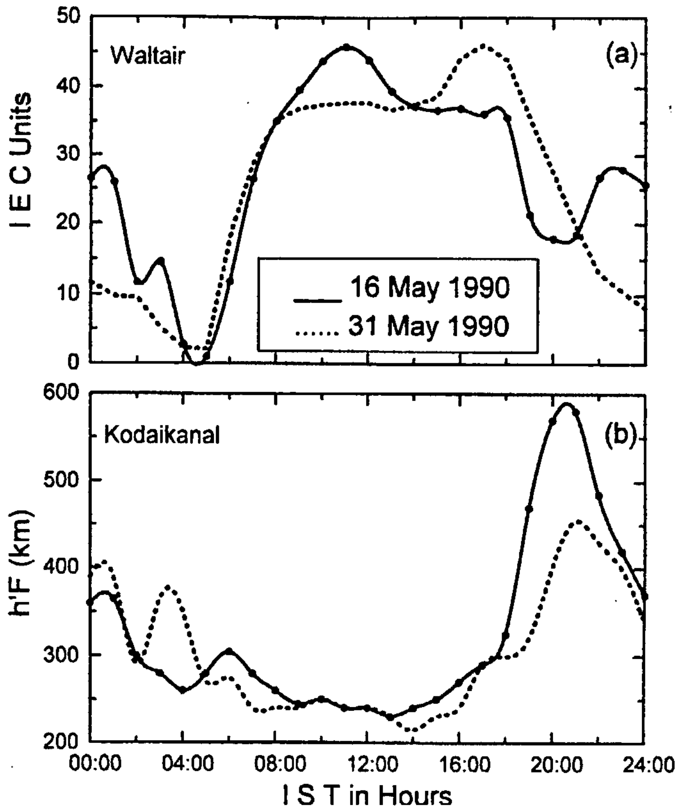

Fig. 1. Typical variation of a) IEC at Waltair with post-sunset enhancement and monotonic decrease and b) corresponding F layer height at Kodaikanal

(Fig. 2b), the NTE index is found to be 1.97 and the post-sunset peak value in IEC at Waltair is more pronounced (around 2100 hrs IST) than at Calcutta (around 2000 hrs IST). On 4th November, 1989 (Fig. 2c), there is no enhancement in IEC at Calcutta, but a pronounced enhancement in IEC is observed at Waltair around 2200 hrs IST.

The corresponding F region altitude variations (h'F) at Kodaikanal during the above three days are presented in Fig. 3. When the NTE is seen both at Calcutta and Waltair with a higher NTE index (2.67 on 10th Nov '89), the F region at Kodaikanal rises to 470 km. On 3rd November 1989, when the NTE index is 1.97 the peak altitude of F layer at Kodaikanal is 380 km. When the NTE in IEC is present only at Waltair (on 4th November, 1989) the F region altitude at Kodaikanal is 350 km. Thus, it is clear that whenever the peak altitude of the F region at the magnetic equator is higher during the post-sunset hours, the NTE index is larger and the anomaly is more pronounced at higher latitudes (Calcutta). From a study of the data of 12 typical days during the period of October-November 1989 it is estimated that, if the maximum altitude at the magnetic equator is around 400 km,

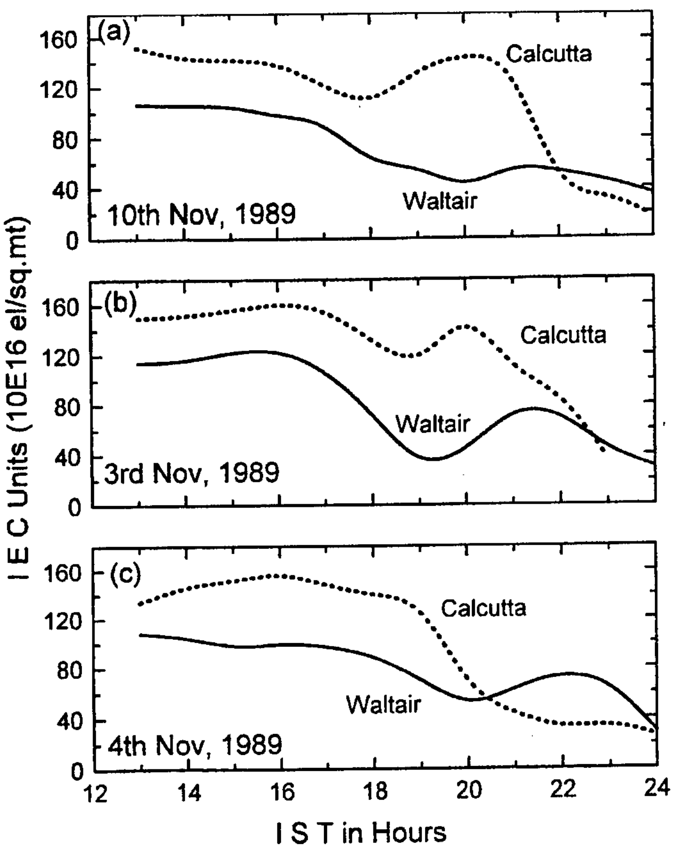

Fig. 2. Typical cases of NTE in IEC at Waltair and Calcutta

the NTE index goes up to 2 units and if the maximum altitude is above 500 km the NTE index is around 2.5 units. Thus it may be inferred that the higher the maximum altitude attained by the F layer at equatorial region, the higher is the NTE index.

3.3 Meridional wind variation during the presence and absence of NTE in IEC

The vertical drift of F region around the equatorial latitudes is mainly electrodynamic ($\mathbf{E}\times\mathbf{B}$) in nature, while the vertical drift at off-equatorial latitudes is effected by the direction of the meridional neutral winds besides the $\mathbf{E}\times\mathbf{B}$ drift. To study the meridional wind variations which effect the F region ionisation at low latitudes, the meridional wind velocity components are calculated using the F layer altitude variations at the equatorial (Kodaikanal, 10°N) and off-equatorial (Ahmedabad, 23°N) stations, following the method proposed by Krishna Murthy et al. (1990). The meridional wind variations calculated during the three typical days considered above (10th, 3rd and 4th November, 1989) are presented in Fig. 3b. The wind

pattern is almost similar upto 1900 hrs IST during all the three days. However, the time of reversal in the wind direction from poleward (−ve values) to equatorward (+ve values) is earlier (around 1915 hrs IST) by 30–45 minutes on 10th and 3rd Nov '89, when the NTE in IEC is present at both the stations. While on 4th Nov '89, when the NTE in IEC occurred only at Waltair, the reversal in the wind direction from poleward to equatorward is delayed and occurs later (around 2000 hrs IST).

4. Discussion

When the F region at the equator is at its peak altitude, the plasma tries to move downward along the field lines and towards sub-tropical latitudes. This movement ceases soon after the F region drift becomes downward. When there is large downward drift during evening hours, the prevailing meridional wind, which is equatorward around that time, tries to push the plasma along the filed lines towards the equator from the anomaly crest regions (Balan and Bailey 1995). This process is termed as the reverse movement of the fountain (Rama Rao et al. 1980, Balan and Bailey 1995) and leads to the reverse flow of plasma resulting in a strong pre-midnight increase in $N_{\max}$ and IEC at sub-tropical latitudes.

In the present study, it is observed that if the peak altitude attained by the F layer at equatorial region is higher and if the reversal in the wind direction is earlier, then the NTE index is larger. By the time the F region at Kodaikanal reaches the maximum altitude (1800–1900 hrs IST, see Fig. 3a) on 10th and 3rd Nov '89, the wind at low latitudes is poleward (Fig. 3b), which may result in the development of a prominent post-sunset anomaly in the ionisation (Garg et al. 1983). However, about 30 minutes later, the wind becomes equatorward, which pushes the ionisation up along the field lines towards the equator causing the reverse movement of the anomaly towards equator (Garg et al. 1983, Balan and Bailey 1995). On 4th Nov '89, when the F region at Kodaikanal reaches the maximum altitude around 2000 hrs IST, the poleward wind is almost minimised and hence might have restricted the movement of ionisation anomaly to a narrow belt around the magnetic equator, and hence the NTE in IEC on this day is seen only at Waltair. The occurrence of secondary peak during the post-sunset hours in IEC appearing first at Calcutta (anomaly crest station) and later at Waltair (low latitude station) indicates the reverse movement of the plasma (Balan and Bailey 1995). However, if the F region maximum altitude is lower at the equator and the wind remains poleward for longer time (i.e. the reversal in the wind direction is delayed), the development of the anomaly during the post-sunset hours is confined only to lower latitudes (Fig. 2c).

Acknowledgements

Authors thank Prof. A Dasgupta of Calcutta University for providing the IEC data of Oct–Nov, 1989. One of the authors, PSR thanks CSIR (Govt. of India) for awarding the research associateship.

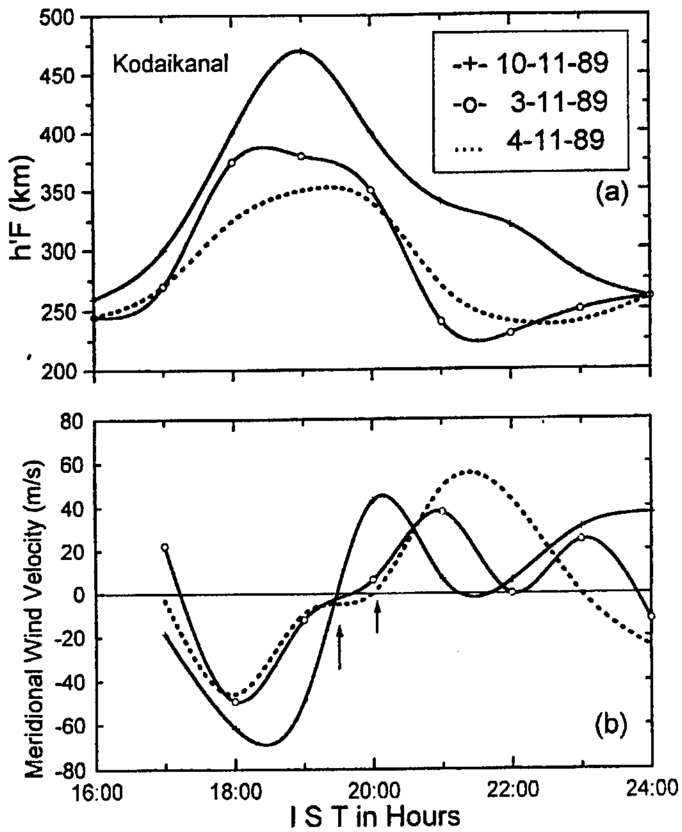

Fig. 3. Variation of a) h'F at Kodaikanal and b) meridional wind velocity at low latitudes

References

Anderson D N, Klobuchar J A 1983: *J. Geoph. Res.*, 88, 8020–8026.

Appleton E V 1960: Equatorial Anomaly, P3, Elsevier, Amsterdam

Balan N, Bailey G J 1995: *J. Geoph. Res.*, 100, A11, 21421–21432.

Garg S C, Singh L, Tyagi T R, Somayajulu Y V 1983: In: Proc. of the Int. Beacon Sat. Symp., New Delhi, 359–373.

Krishna Murthy B V, Hari S , Somayajulu V V 1990: *J. Geoph. Res.*, 95, 4307–4310.

Martyn D F 1955: In: Proc. Cambridge Conference, London, 254–263.

Rama Rao P V S, Ramana Rao B V, Nru D, Rao B V P S, Rao M S 1980: *Adv. Space. Res.*, 8, 153–160.

Acta Geod. Geoph. Hung., Vol. 33(1), pp. 9–17 (1998)

SOLAR AND MAGNETIC ACTIVITY CONTROL ON THE VHF IONOSPHERIC SCINTILLATIONS AT LOW LATITUDE

SUSHIL KUMAR[1], P K PUROHIT[1], A K GWAL[1]

Solar and magnetic activity effects on VHF night-time ionospheric scintillations recorded during three and half year at Bhopal, a station near the northern crest of the equatorial anomaly in the Indian region have been presented. The night time diurnal scintillation occurrence decreases with decrease in solar activity. Monthly mean scintillation occurrence changes according to solar activity during E- and D-months but not so during J-months. The magnetic activity shows seasonal effect on scintillations and, in general, inhibits the scintillation occurrence in pre-midnight period and enhances little in post-midnight period especially after 03h IST. For most of the severe magnetic storms in which D_{st} goes below -125 nT and recovery phase starts in post-midnight - dawn local time sector, strong post-midnight scintillations which sometimes extend for several hours beyond the local sunrise, are observed.

Keywords: geomagnetic activity; irregularities; scintillations; spread-F

1. Introduction

The radio wave scintillation technique is a simple and convenient method of studying the ionospheric electron density irregularities. At low latitudes the scintillation is basically a night-time phenomenon associated with spread-F seen as diffuse F region traces in ionograms. It is generally agreed that, after the local sunset, the bottomside F region over the magnetic equator is subjected to gravitational Rayleigh-Taylor (R-T) mechanisms hence the irregularities known as plasma bubbles are generated which rise to the topside of ionosphere due to non-linear evolution of EXB drifts, and produce the scintillations at the stations situated off the magnetic equator in discrete patches. Dabas and Reddy (1986) have reported that scintillation activity up to 23°N magnetic latitude in the Indian region during high solar activity is controlled by the generation of F region irregularities. It has been shown that plasma bubbles have the large N-S extent of more then 2000 km on either side of magnetic equator and are strongly field aligned (Weber et al. 1982). With an increasing intetest in understanding of the behaviour of ionospheric irregularities at the magnetic equator, some excellent efforts have been made to examine the solar and magnetic activity control of the occurrence of scintillations associated with ionospheric irregularities at equatorial and low latitudes (Aarons et al. 1980, DasGupta et al. 1981, Rastogi et al. 1981, DasGupta et al. 1985, Dabas et al. 1989). Rastogi et al. (1990) for Indian equatorial stations showed a very large decrease in scintillation activity with decrease in solar activity, whereas for the American sector they found low dependence of scintillations on sunspot number. Dabas et

[1]Space Plasma Laboratory, Department of Physics, Barkatullah University, Bhopal–462 026, India

al. (1989) considering the scintillation data from a chain of stations extending from the equator to 21°N magnetic latitude along 94°E longitude in the Indian zone and at Lunping (14.09°N dip lat.) in far eastern zone, have observed that with increase in magnetic activity, the scintillation occurrence increases in post-midnight periods in all the longitude sectors while the pre-midnight phenomenon is dependent on season as well as on longitude.

In India, a network of radio wave scintillation recording stations, commissioned by the Department of Science and Technology, Govt. of India, New Delhi, was established as a part of *All India Coordinated Programme on Ionospheric Thermospheric Studies* (AICPITS), to understand the daily, latitudinal, longitudinal, solar and magnetic activity variations of scintillations. The data recorded during Phase I of the AICPITS offer us an excellent opportunity to present a study on the solar and magnetic activity effects on VHF scintillations recorded at Bhopal, a station near the equatorial anomaly crest in the Indian region.

2. Experimental data

Radio signals at 244 Mhz from September 1988 to December 1991 and at 250 MHz from October 1992 to February 1993 were received at Bhopal (23.5°N, 77.6°E, sub-ionospheric points for FLEETSAT at 400 km; 21.6°N, 77.2°E, dip lat. 16.5°N) using a simple eleven element Yagi-Uda antenna and indigenously fabricated VHF receiver. A single channel strip chart recorder was used for recording the amplitude of signals. The 244 MHz signal could not be recorded from February 1992 to september 1992 due to non-availability of this signal and it took sometime to modify the receiver capable of receiving the 250 MHz signal. The above periods of scintillation observations correspond to higher solar activity phase of solar cycle 22 with its maxima in 1989. Quarter hourly scaling of scintillations having peak-to-peak fluctuations > 1 dB forms the basis of data for analyses.

3. Results

3.1 Solar activity variation of scintillations

To study the effect of solar activity on scintillations, the diurnal variation of scintillation occurrence has been plotted in Fig. 1 wherein mean sunspot numbers have been indicated on respective curves. It can be seen that peak scintillation occurrence at around 2200 IST, was 20% during 1989, 15% during 1990, 13% during 1991 and 10% during October 1992 to February 1993 which indicates a strong dependence of scintillation activity on solar activity. Pathak et al. (1995) working on 244 MHz scintillations at Rajkot located in the anomaly crest region in India have shown the similar trend of decrease in night-time scintillation occurrence from 1989–1991 but the occurrence at Rajkot was larger as compared to that at Bhopal. It is mainly due to the fact that at Rajkot the scintillations of magnitude $> .5$ dB were taken for analysis whereas in this paper the scintillations > 1 dB have been considered. It can not be accounted for the longitudinal difference because the magnetic declination angles at Bhopal and Rajkot are nearly the same. The

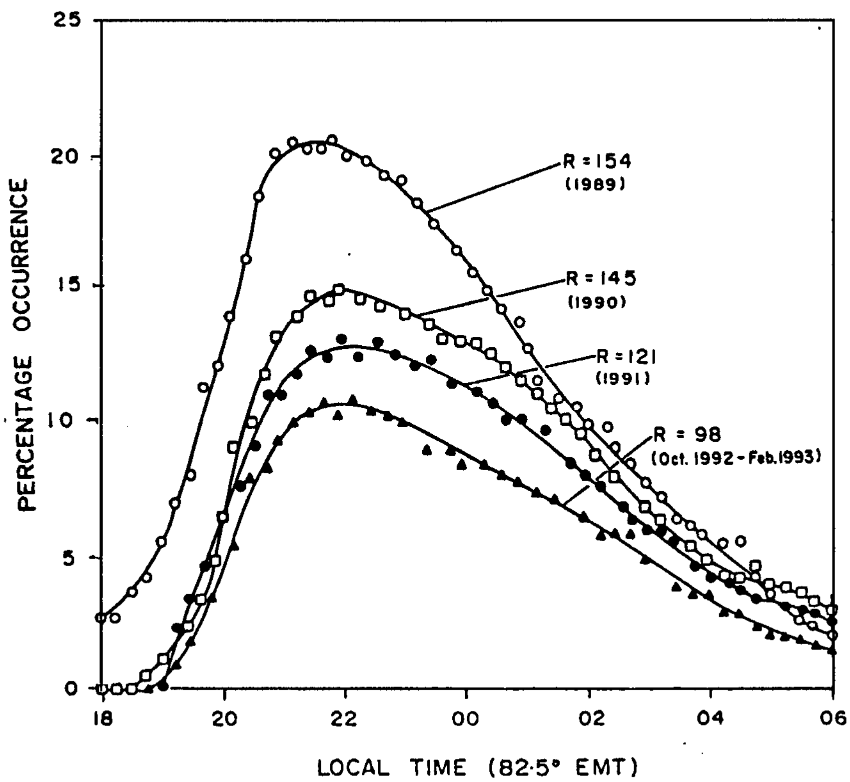

Fig. 1. Nocturnal variation of percentage occurrence of scintillations during 1989, 1990, 1991 and October 1992 to February 1993 with respect to averaged sunspot numbers

difference in magnetic dip angle at these two stations is approximately 1°. Month-to-month variation of mean percentage occurrence of scintillations for the years 1988–1991, the annual sunspot number (R) being 98, 154, 145 and 121, has been plotted together with the sunspot number in Fig. 2. It is clearly seen from this figure that there is an increase in scintillation activity corresponding to the increase in sunspot numbers during E- and D-months. During the decreasing phase of solar activity the scintillations are found to decrease, during E- and D-months. But during J-months there is no significant change in occurrence of scintillations with change in solar activity. Another feature of interest is that although the scintillation activity changed with the solar activity but the equinoctial maxima are always most prominent in every year during 1989–1991. The positive association of scintillation activity with sunspot number (Fig. 2) is in good agreement with results reported by Rastogi et al. (1990) for equatorial stations in the Indian region and by Pathan et al. (1991) for the Indian low latitude station Karur (3.4°N dip lat.) during E- and D-months. The solar activity effects reported here are consistent with previous results by DasGupta et al. (1981) and Pathak et al. (1995) for the Indian anomaly crest stations Calcutta (23°N, 88.5°E) and Rajkot (22.3°N, 70.7°E) respectively for all the three seasons.

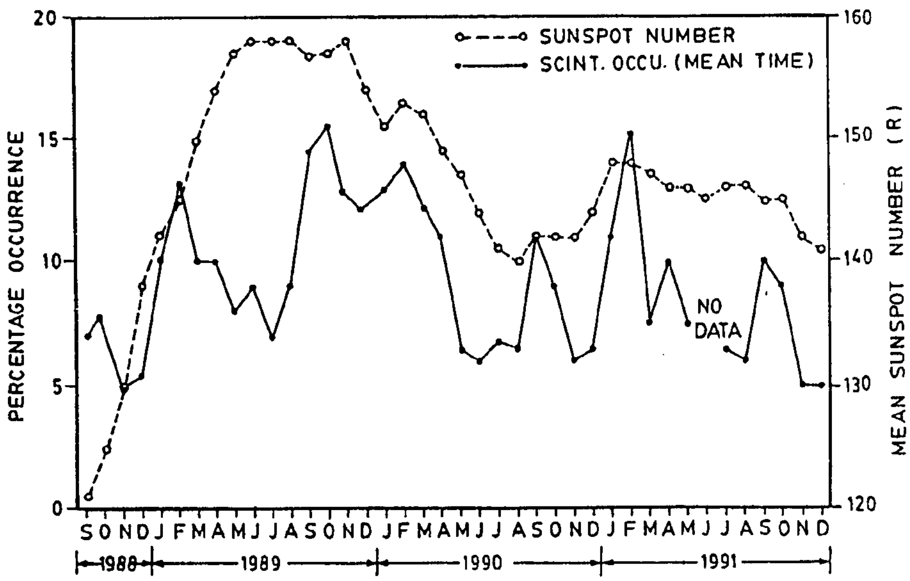

Fig. 2. Monthly variation of percentage occurrence of scintillations averaged for night-time 1800 to 0600 hrs and mean sunspot numbers

3.2 Magnetic activity effects on scintillations

Percentage occurrence of scintillations has been taken for five international quiet (Q) and five international disturbed (D) days from every month's from September 1988 to December 1991. The occurrence of scintillations between 18 hrs to 06 hrs (82.5°EMT) on Q- and D-days for three seasons; E-months, D-months and J-months and their annual average are shown in Fig. 3. It is obvious from this figure that due to geomagnetic disturbances, the scintillations are inhibited in pre-midnight period and are increased in post-midnight period, especially after the 0300 hrs IST, during E- and D-months. The degree of suppression of scintillations in pre-midnight on D-days during E-months is larger as compared to that during D-months. But during J-months on D-days the scintillations are first increased in early pre-midnight period then decreased and again increased in post-midnight period. The annual geomagnetic disturbance effect shows a clear suppression of scintillations in pre-midnight and in early post-midnight periods (before 0300 IST) whereas in post-midnight period (after 0300) the scintillations are increased.

To understand the variation of scintillation activity under magnetic storm conditions, the D_{st} index which is the measure of ring currents at low latitudes, has been used as a measure of magnetic activity. The general features of the storms for which scintillation data are available have been given in Table I. The night 0 is the night of storm onset and night 1 and night 2 are next two nights following the onset day. The behaviour of scintillation activity on 13 March 1989 has been presented in Fig. 4.

Storm of 13 March 1989 — This particular storm of 13 March 1989 was one of

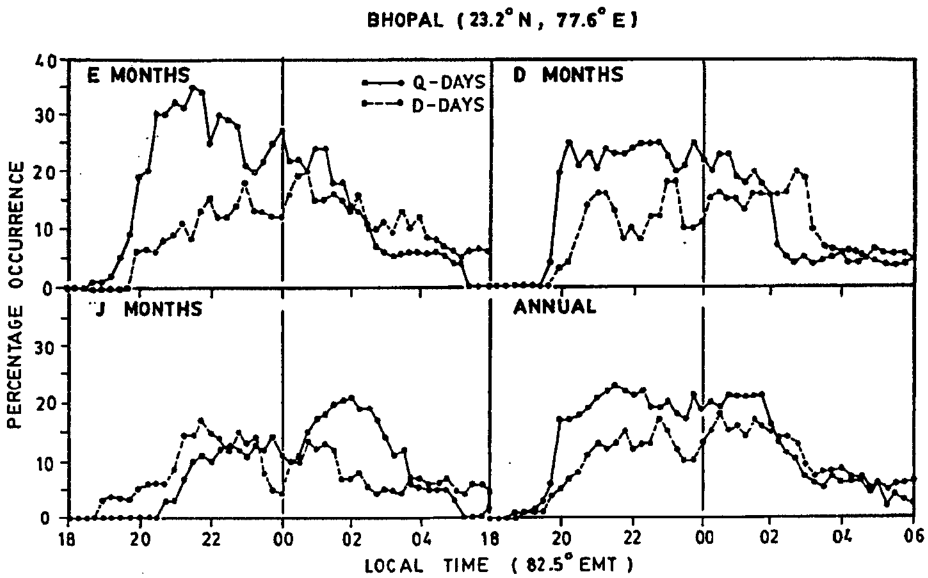

Fig. 3. Nocturnal variation of percentage occurrence of night-time scintillations on geomagnetically quiet and disturbed days for different seasons of the year

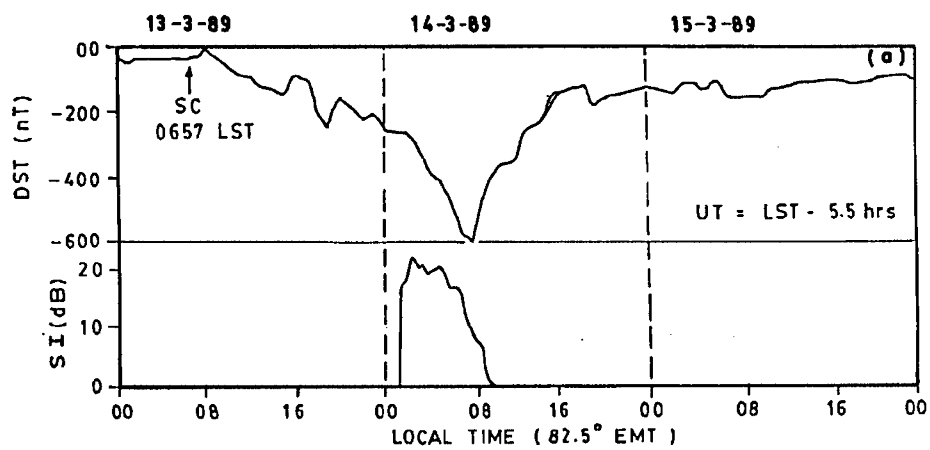

Fig. 4. Scintillation activity connected with the geomagnetic storm of 13 March, 1989 as indicated by equatorial D_{st} variations

the most severe events in the recent years. The D_{st} value had its lowest value -599 nT at 0630 IST on March 14. A_p index was 246 on March 13. The K_p index varied from 60 to 90 between the first and the eighth 3-hour period. The sum of K_p on March 13 was 650. From the curve in Fig. 4 it can be noted that a very strong scintillation activity with fast fading rate extending well beyond the local sunrise, was observed. This storm was accompanied by major polar cap absorption events, extensive proton precipitation and the usual red auroras (Campbell 1996). The

Table I. Nighttime scintillation activity connected with geomagnetic storms in which D_{st} decreases below −75 nT and the recovery phase lasts from post-midnight to dawn in the local morning time sector

S. No.	Storm day	Sudden commencement	Recovery phase day: time (UT)	Min DST (nT)	Night 0 pre	Night 0 post	Night 1 pre	Night 1 post	Night 2 pre	Night 2 post
1	17 Dec 1988	1826	18 Dec 0100	−75	–	–	–	–	–	–
2	25 Dec 1988	0400	25 Dec 1900	−84	–	–	ND	ND	–	–
3	11 Jan 1989	1205	11 Jan 2200	−132	–	O	–	–	O	O
4	20 Jan 1989	1130	20 Jan 2000	−122	O	O	ND	ND	O	O
5	13 Mar 1989	0127	14 Mar 0100	−599	–	O	–	–	O	O
6	27 Mar 1989	1342	29 Mar 2200	−131	ND	–	–	–	–	–
7	21 Aug 1989	1416	21 Aug 2200	−87	O	–	O	–	–	–
8	17 Nov 1989	0925	17 Nov 2300	−266	–	O	–	O	O	–
9	25 Mar 1990	0000	25 Mar 0000	−116	O	O	O	–	–	–
10	27 Nov 1990	0230	27 Nov 2200	−136	O	O	–	–	O	–
11	24 Mar 1991	0300	25 Mar 0100	−77	O	O	–	O	–	–
12	04 Apr 1991	1121	04 Apr 2200	−298	–	–	–	ND	–	–
13	04 Jun 1991	0377	05 Jun 2100	−213	–	O	–	O	–	O
14	30 Aug 1991	0701	30 Aug 2100	−111	–	–	–	–	–	–
15	01 Nov 1991	1100	01 Nov 2000	−192	–	–	–	–	–	–

IST = UT + 5.5 Hrs
O: Scint. Present; –: No Scint.; ND: No Data

auroral zone was displaced to mid-latitudes; there were simultaneous electric power-line outages (from current induction) throughout the province of Quebec, Canada, and northern USA implying that maximum field effects were located around those locations (Allen et al. 1989). Aarons and GasGupta (1984) have reported similar event of post-midnight scintillation extending into daytime at Huancayo near the magnetic equator and Ascension Island near the anomaly crest region. DasGupta et al. (1985) studied a number of post-midnight scintillation events extending into daytime and reported them to be related to the maximum negative excursion of horizontal intensity of the geomagnetic field occurring in the 0000–0600 hrs local time.

The intense scintillations with fast fading rate observed during the recovery phases of these storms, show the generation of new intense and fast moving irregularities as the depth of fading is an indication of intense irregularity and higher fading rate indicates the faster motion of irregularities. From the Fig. 4 and Table I it can be shown that for most of the storms the recovery phase of which starts in the post-midnight to dawn local time sector, and D_{st} decreases below −125 nT, the probability of occurrence of scintillation activity is enhanced from post-midnight to local morning hours. During the main phase of the storms the night-time scintillation activity remains unaffected. Under severe magnetic storm conditions, the pre-midnight scintillations which are rarely observed may be due to residuals of drifting clouds of irregularities which have been generated before the storm onset.

4. Discussion

The gravitational Rayleigh-Taylor (R-T) mode which includes electric field and neutral wind terms is believed to be the primary source for the generation of irregularities over the magnetic equator. The geometry of field lines and ray path from FLEETSAT (73°E) to Bhopal indicate that irregularities must rise over the magnetic equator to about 800 km or more to produce the scintillations. The irregularities which cause scintillations at the locations like Bhopal drift eastward with the velocity ranging from 180 m/s to 55 m/s during the night and ranging from 120 m/s to 50 m/s in case of geomagnetic disturbances (Kumar et al. 1995).

DasGupta et al. (1981) studied the solar activity control of the occurrence of 136 MHz scintillations at Calcutta (16.5°N dip lat.), a station near the anomaly crest region in the Indian zone, and found that the occurrence of scintillations during E- and D-months increases with solar activity while remains virtually constant during J-months. Rastogi et al. (1990) and Pathan et al. (1991) showed a strong dependence of equatorial scintillations on the sunspot number in the Indian region. Pathan et al. (1992) have shown that occurrence of scintillations at Bombay (13.4°N dip. lat.), a temperate latitude station, is more controlled by solar activity than at Trivandrum (0.3°N dip. lat.), an equatorial station in the Indian region. They also reported the occurrence of scintillations at Bombay to be of equatorial origin during all the seasons. Recently Pathak et al. (1995) have shown that at another Indian anomaly crest station Rajkot (15.3 dip. lat. ° E) scintillation occurrence increases with solar activity during equinoxes and winter whereas it decreases in summer with solar activity. The three stations Rajkot, Bhopal and Calcutta cover almost the entire anomaly belt in the Indian region, therefore, based on the results published from Rajkot and Calcutta, and the results presented here one may now conclude that characteristics of scintillations in the anomaly crest region during E- and D-months are similar to that seen at equatorial stations whereas the scintillations occurring during J-months may be due to mid latitude irregularities. The mid-latitude ionospheric scintillations do not occur so often as the equatorial or high latitude scintillations (Aarons 1982), and do not show significant variation with solar activity. The scintillations during J-months may also be due to sporadic-E or bottomside spread-F.

The strong and fast scintillations on VHF signals pre-midnight are associated with range type spread-F whereas weak and slow scintillations in post-midnight are due to frequency type of spread-F (Huang 1970, Chandra and Rastogi 1974). During high sunspot years, the range type spread-F is maximum pre-midnight and frequency type spread-F post-midnight. As the scintillations at Bhopal station seem to have equatorial origin during E- and D-months, therefore, the inhibition of scintillation activity pre-midnight in case of magnetically disturbed conditions may be due to the suppression of equatorial range type of spread-F in pre-midnight period in magnetically disturbed conditions. Rastogi et al. (1978) studied the effects of geomagnetic disturbance on equatorial spread-F and found that occurrence of range type spread-F is decreased on disturbed days in pre-midnight hours during E- and D-months. Whereas the occurrence of frequency type spread-F is decreased

practically in the night hours during E- and D-months, during J-months, they noted the increase of frequency spread-F in the post-midnight period. Farley et al. (1970) suggested the idea of a threshold height above which the F layer has to rise before the irregularities associated with spread-F can be generated. The inhibition of the occurrence of spread-F or scintillations at low latitude on geomagnetically disturbed days in the pre-midnight period is due to the reduction of the post-sunset rise of the F layer in the equatorial region as the increase in geomagnetic activity limits the height of rise of the F layer and reduces the probability of occurrence of the equatorial spread-F (Alex and Rastogi 1987).

The strong post-midnight scintillations associated with severe magnetic storms are explained in terms of the reversal of the equatorial ionospheric electric field. This electric field plays a significant role in the growth of irregularities near the magnetic equator, and is affected by high latitude and magnetospheric electric fields and current systems during magnetic storm conditions. During magnetic disturbances the coupling of high latitude and magnetospheric current systems with the equatorial electric field possibly causes the reversal of electric field from a westward to an eastward direction (Gonzales et al. 1979). The high latitude electric fields penetrate to low latitude and can produce large perturbations in low the latitude electric field. Nopper and Carovillano (1978) have shown from model calculations that during the disturbed periods only high latitude current systems may produce significant perturbations even reversals of the equatorial electric field pattern and the reversals are most pronounced in the midnight - dawn sector. Chandra et al. (1995) recently have shown that it is the high latitude electric field which during magnetic storms penetrates to low and equatorial latitudes and leades to the generation of F region irregularities extending into daytime. The eastward electric field post-midnight may eventually lead under the favourable conditions to the generation of irregularities near the magnetic equator which subsequently rise to the topside ionosphere in the form of large plasma bubbles and produce the scintillations at the stations situated off the magnetic equator with a certain time delay. At local sunrise, the large conductivity of the E region prevents the growth of plasma bubble by short circuiting the electric field but sometimes it takes several hours for the bubbles to decay thereby they cause scintillations even after sunrise as indicated by Fig. 4. Scintillations not associated with magnetic storms lead us to say that not all the reversals are accompanied by irregularities. There may be some other components which must be present simultaneously for the generation of irregularities and these components could be neutral winds and large scale plasma density gradients which are also necessary for the R-T mode to be operative. The relative contributions of ionospheric and magnetospheric currents in the storm time affecting low latitudes vary with station location and not all the geomagnetic storm effects to which the high latitude ionosphere responds drastically, reach low latitudes.

Acknowledgements

One of the authors (SK) sincerely acknowledges to the Council of Scientific and Industrial Research (CSIR), Govt. of India, New Delhi and M.P. Council of Science and Technology (MPCST), Bhopal, India, for financial support for presenting the paper in IBSS'97.

References

Aarons J 1982: *Proc. IEEE*, 70, 360–373.

Aarons J, DasGupta A 1984: *Radio Sci.*, 19, 731–739.

Aarons J, Mullen J P, Koster J R, da Silva R F, Madeiros J R, Bushby A, Pantoza J, Lanat J, Paulson M R 1980: *J. Atm. Terr. Phys.*, 42, 861–866.

Alex S, Rastogi R G 1987: *Ann. Geophys.*, 5, 83–88.

Allen J, Frank L, Sauer H, Reiff P 1989: *Trans. Amer. Geophys. Un.*, 70, 1479–1488.

Campbell W H 1996: *J. Atm. Terr. Phys.*, 58, 1171–1187.

Chandra H, Rastogi R G 1974: *Current Sci.*, 43, 567–568.

Chandra H, Vyas G D, Pathan B M, Rao D R K 1995: *J. Atm. Terr. Phys.*, 57, 1273–1285.

Dabas R S, Reddy B M 1986: *Radio Sci.*, 21, 453–462.

Dabas R S, Lakshmi D R, Reddy B M 1989: *Radio Sci.*, 24, 563–573.

DasGupta A, Maitra A, Basu S 1981: *Radio Sci.*, 16, 1455–1458.

DasGupta A, Maitra A, Das S K 1985: *J. Atm. Terr. Phys.*, 47, 911–916.

Farley D T, Balsley B B, Woodman R F, McClure J P 1970: *J. Geoph. Res.*, 75, 7199–7216.

Gonzales C A, Kelly M C, Fejer B G, Vickrey J F, Woodman R F 1979: *J. Geoph. Res.*, 84, 5803–5812.

Huang C M 1970: *J. Geoph. Res.*, 75, 4833–4841.

Nopper R W, Carovillano R L 1978: *Geophys. Res. Lett.*, 5, 699–702.

Pathak K N, Jivrajani R D, Iyer K N 1995: *Ann. Geophys.*, 13, 730–739.

Pathan B M, Koarkar P V, Rastogi R G, Rao D R K 1991: *Ann. Geophys.*, 9, 126–132.

Pathan B M, Rastogi R G, Rao D R K 1992: *J. Geomag. Geoelectr.*, 44, 129–142.

Rastogi R G, Vyas G D, Chandra H 1978: *Proc. Ind. Acad. Sci.*, 87, 109–113.

Rastogi R G, Mullen J P, Mackenzie E 1981: *J. Geoph. Res.*, 86, 3661–3664.

Rastogi R G, Koparkar P V, Pathan B M 1990: *J. Geoph. Res.*, 42, 1–10.

Sushil Kumar, Gwal A K, Pathan B M, Rao D R K 1995: *Ann. Geophys.*, 13, 724–729.

Weber E J, Brinton H C, Buchau J, Moore J G 1982: *J. Geoph. Res.*, 87, 10503–10513.

Acta Geod. Geoph. Hung., Vol. 33(1), pp. 19–24 (1998)

SATELLITE BEACON AND IONOSONDE MEASUREMENTS OF IONOSPHERIC IRREGULARITIES OVER INDIA DURING THE EQUINOCTIAL MONTH OF SEPTEMBER 1991

P V S RAMA RAO[1], P SRI RAM[1], P T JAYACHANDRAN[1], D S V V D PRASAD[1]

The spread-F and scintillation observations made at ten Indian stations covering 8 to 25°N geographic latitudes during the equinoctial month of September 1991 are used to study the occurrence characteristics of ionospheric irregularities and their association with the changes in the virtual height of the F layer at an equatorial station, Trivandrum (0.3°S dip). No event of scintillation occurrence is observed at off-equatorial latitudes (within the anomaly crest region) without their prior occurrence at the equatorial station (Tiruchendur, 2.3°N dip which is close to Trivandrum). However, the duration of scintillations at far equatorial stations (10 to 20°N dip) are, sometimes, longer than the durations at the near equatorial stations (0 to 10°N dip). On such occasions, the onset of scintillations and spread-F is prior to the post-sunset reversal of the height of the F layer (h'F) from upward to downward direction at the equatorial station, Trivandrum. But, if the duration of the irregularities is longer at equatorial latitudes and decreases towards higher latitudes, the onset of irregularities is observed to coincide with the time of post-sunset reversal in h'F at Trivandrum. These two types of irregularities are interpreted to be generated by the two different instability mechanisms, namely $\mathbf{E} \times \mathbf{B}$ drift and RT instability respectively.

Keywords: ionosonde; satellite beacon; scintillations; spread-F; virtual height

Introduction

The equatorial ionospheric F region irregularities are known to be generated by gravitational Rayleigh-Taylor instability mechanism (GRTI) in association with the $\mathbf{E} \times \mathbf{B}$ (cross-field) instability mechanism. There appears to exist a basic difference in the occurrence of the above two mechanisms, namely when the gradient in the electron density (∇n) is anti-parallel to the gravity (g) and perpendicular to the earth's magnetic field $\overline{\mathbf{B}}$ the RTI operates, when ∇n is parallel to gravity the $\mathbf{E} \times \mathbf{B}$ instability operates. As the ionospheric irregularities are generated over the magnetic equator and move along the magnetic field-lines, an attempt has been made to study the occurrence of spread-F and scintillations at different latitudes from equator to anomaly crest region in association with the virtual height of F region (h'F) variations at the magnetic equator, so as to see the effect of these two phenomena in the generation of ionospheric irregularities.

[1]Department of Physics, Andhra University, Visakhapatnam 530 003, India

Data

Digital ionosondes (KEL) are operated at Trivandrum (0.3°S dip), Waltair (20°N dip) and Ahmedabad (32°N dip) during September 1991 from which the spread-F occurrence and h'F parameters are taken. Amplitude scintillations at 250 MHz radio beacon signal from FLEETSAT were recorded at Tiruchendur (8.6°N), Payyanur (12°N), Anantapur (14.5°N), Nuzvid (16.8°N), Waltair (17.7°N), Bombay (19°N), Ujjain (23.3°N) and Varanasi (25.2°N) during the same period.

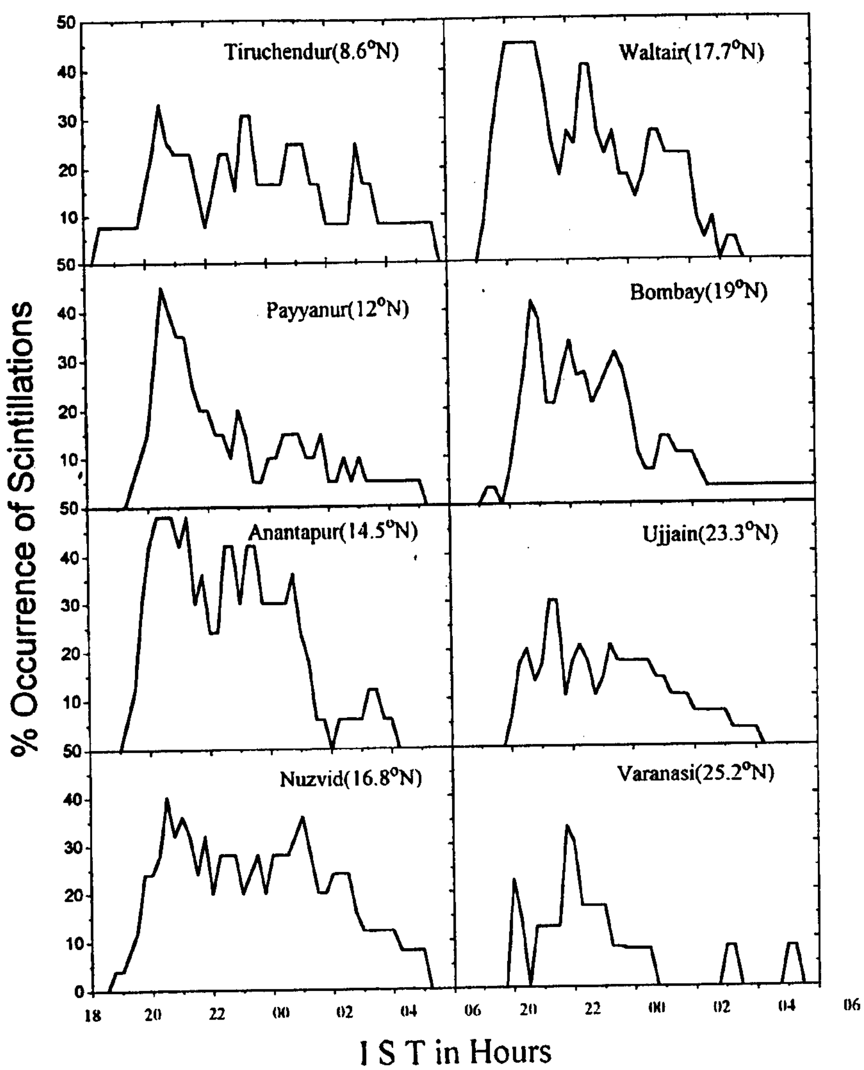

Fig. 1. Percentage occurrence of scintillations (250 MHz) at various stations during September 1991

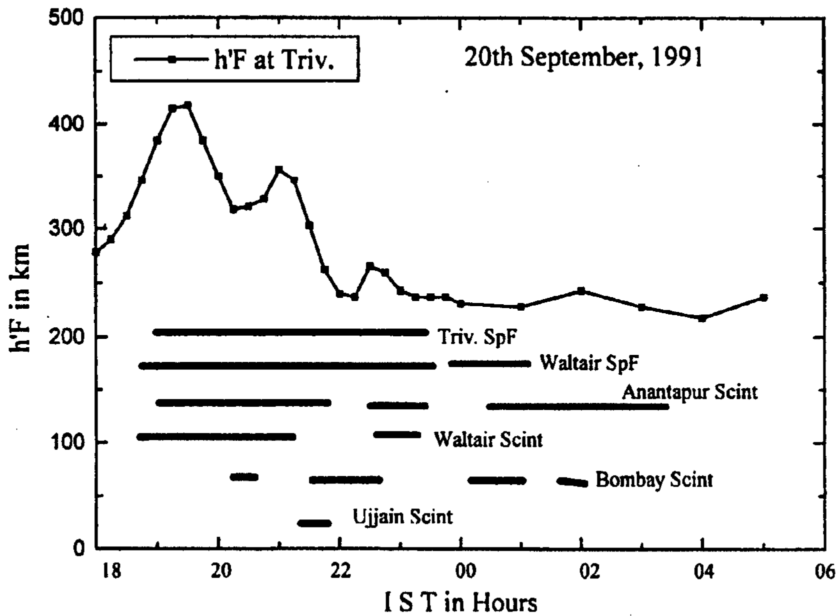

Fig. 2. Onset of irregularities coinciding with the post-sunset reversal in h'F at Trivandrum

Results

The monthly average percentage occurrence of scintillations from all the above mentioned eight stations are computed and presented in Fig. 1. The peak occurrence of scintillations is observed at all the stations (except at Tiruchendur) about an hour after the sunset followed by a gradual decrease with local time. The peak percentage occurrence also gradually decreased with the increase of latitude. At Varanasi (beyond the crest of the anomaly) the scintillation occurrence during the post-midnight hours is almost absent.

The onset of scintillations is found to generally 'coincide with' or 'follow' the post-sunset reversal in h'F variation at Trivandrum (an equatorial station). However, on two occasions, it is seen that the occurrence of irregularities started well ahead of the post-sunset reversal of h'F at Trivandrum. To study the observed differences in the onset of irregularities (spread-F and scintillations) a comparison is made with reversal time of h'F on some typical days. On 20th September 1991 (Fig. 2), the onset of spread-F at Trivandrum coincided with the post-sunset reversal in h'F at Trivandrum (an equatorial station). On this day the amplitude scintillations are observed for long duration up to the latitude of Bombay (19°N), while at Ujjain (23.3°N) the scintillations are observed only for about 30 minutes duration. Though the occurrence of spread-F and scintillations at the stations shown in this figure is significant during the pre-midnight hours, they are not so prominent during the post-midnight hours. Similar feature is also seen on 19th September 1991 (Fig. 3).

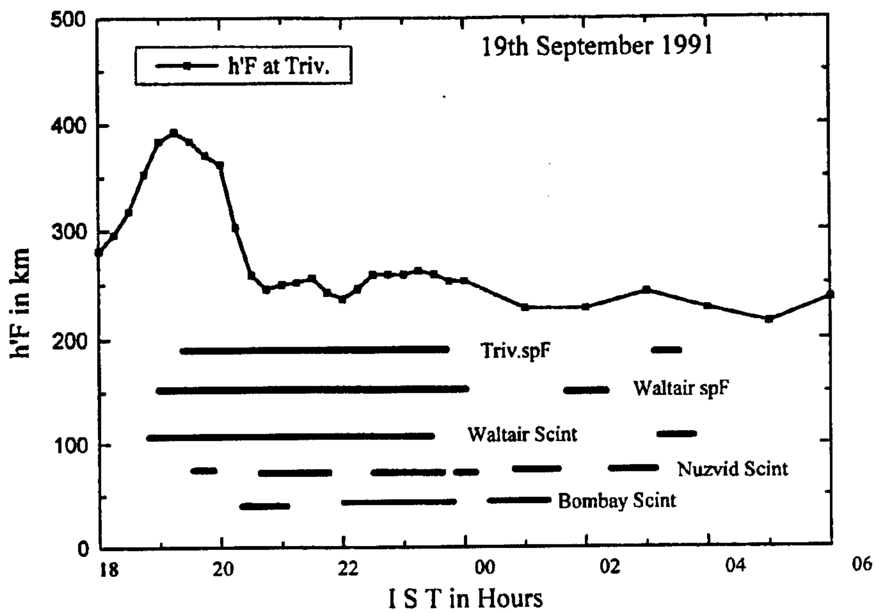

Fig. 3. Onset of irregularities coinciding with the post-sunset reversal in h'F at Trivandrum

In the other type of occurrence of irregularities where the onset preceded the post-sunset reversal in h'F at Trivandrum (on 17th and 21st September 1991, Figs 4 and 5), the occurrence of irregularities is almost similar in durations during pre- and post-midnight periods. On these days, the scintillations are observed for longer durations even at Ujjain on 17th September 1991 (Fig. 4), while on 21st September 1991 (Fig. 5), there is spread-F during the post-midnight hours at Trivandrum and Waltair and scintillations occurred for longer durations even up to Bombay (19°N) and significant scintillations are observed even at Ujjain and Varanasi.

Discussion

The various diagnostic techniques established that the equatorial spread-F (ESF) irregularities occur over a wide range of scale sizes from a few tens of kilometres to a few centimetres and as such it has become evident that no single instability mechanism can account for the observed wide range of scale sizes (Krishna Murthy 1993). By considering all the possible sources for the growth of ESF irregularities, Krishna Murthy (1993) has given a comprehensive equation for the generalised RT growth rate as:

$$\begin{aligned}\gamma &= (1/M)[(g/\nu_{in}L) + (E_x/BL) + (U\nu_{in}/\Omega_i L) + \\ &+((1/M)-1)(W/L) + ((1/M)-1)(U/l)],\end{aligned}$$

where g is acceleration due to gravity, E_x is the eastward electric field, B is the magnetic field, L is the gradient scale length (equal to $N(dN/dh)^{-1}$), U is the zonal

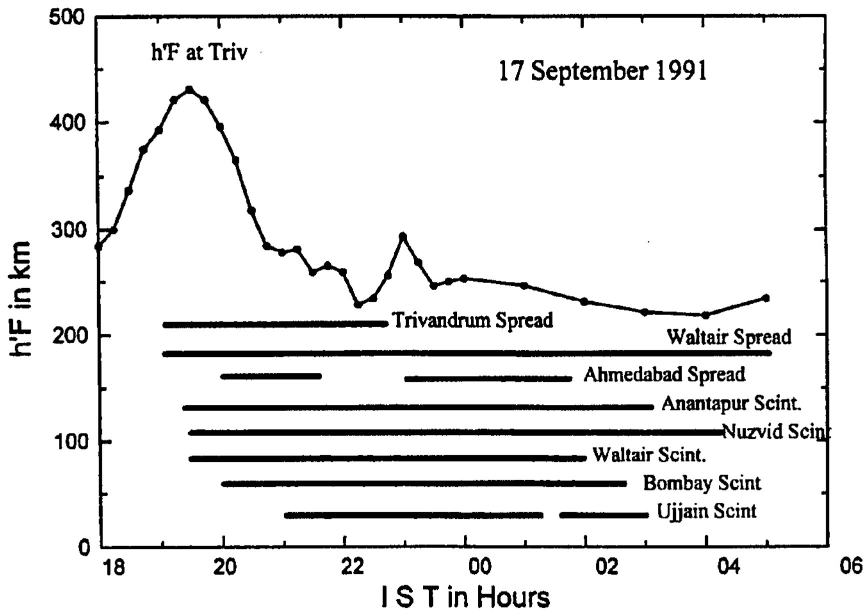

Fig. 4. Onset of irregularities preceding the post-sunset reversal in h'F at Trivandrum

wind, ν_{in} is the ion-neutral collision frequency, M is the shorting factor depending on the conductivities of the E and F layers, W is the vertical winds and l is equal to $[(1/N)(dN/dy)]^{-1}$ where y is the element length in E-W direction. In the above equation, the first term represents the growth rate due to collisional instability, the second term to electric field, third term to zonal wind and density gradient, fourth term to the vertical wind and the fifth term to zonal wind. The first four terms depend on the vertical gradient of the electron density while the fifth term depends on the horizontal density gradient (Krishna Murthy 1993). The effect of the last two terms becomes maximum when the integrated Pederson conductivities of the E and F regions become equal. This situation arises before or just after sunset, when the E region conductivity is still significant and thus is comparable to that of the F region. These mechanisms (corresponding to the last two terms of the above equation) may thus account for the early onset of ESF, provided U and W are in proper direction with respect to g (Krishna Murthy 1993).

The gravitational RT instability mode is reported to be stable at latitudes beyond the anomaly crest regions, while $\mathbf{E} \times \mathbf{B}$ mode is unstable at all latitudes when the electric fields are eastward (Maruyuma 1990). However, the plasma analogy of the classical gravitational RT instability occurs when the acceleration due to gravity g is anti-parallel to the electron density gradient, (n with both of them perpendicular to the magnetic field $\mathbf{B}$. Such a situation always exists in the equatorial bottomside F region. Hence in the present study, when the onset of irregularities coincide or follows the reversal in h'F, the above condition of RT instability holds good. In this case, the irregularities generated are confined to midnight hours and

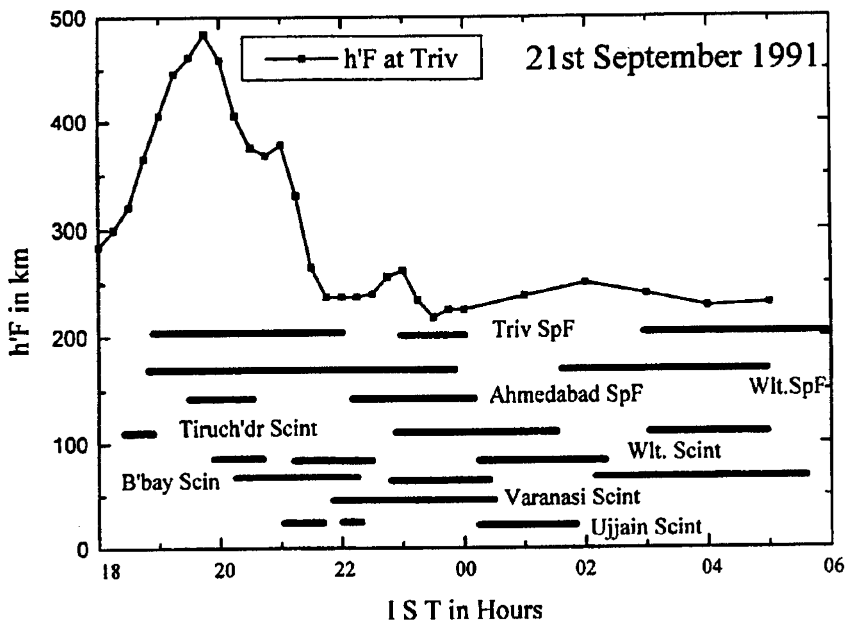

Fig. 5. Onset of irregularities preceding the post-sunset reversal in h'F at Trivandrum

are restricted to lower latitudes. In the other case, when the onset of irregularities preceded the reversal in h'F (i.e., ∇n is parallel to g) at an equatorial station, the horizontal gradient (just after sunset) might also effect (last two terms of the above equation) the growth-rate of the irregularities. These irregularities triggered by the $\mathbf{E} \times \mathbf{B}$ instability aided by the general RT instability mechanism, provide a condition favourable for the sustenance of irregularities for longer durations, hence the occurrence of irregularities is seen well beyond the midnight period as well as beyond the anomaly crest region.

Acknowledgements

The present work is carried-out under the AICPITS programme of Dept. of Science and Technology (Govt. of India). Thanks are due to all the scientists who have provided the data, from their respective stations, used in the present study. One of the authors, PS thank CSIR (Govt. of India) for awarding the research fellowship.

References

Krishna Murthy B V 1993: *I. J. Radio Space Phys.*, 22, 82–87.
Maruyuma T 1990: *Planet. Space Sci.*, 38, 2, 273–286.

Acta Geod. Geoph. Hung., Vol. 33(1), pp. 25–40 (1998)

TIME SERIES MODELLING OF INTENSITY AND PHASE SCINTILLATION AT GPS FREQUENCIES

M A CERVERA[1] and M F KNIGHT[2]

A model based on phase screen diffraction theory is developed to simulate time series of scintillating trans-ionospheric radio signals. The main purpose of the synthetic scintillation time series, or SSTS, model is to test various GPS receiver systems under scintillation conditions. In order to do this, the modelled scintillation data is designed to be input into a model of a GPS receiver tracking loop. It is noted that although the main interest here is in GPS, the SSTS model may also be used at other radio frequencies and for other transmitter-receiver links (e.g. satellite based communication systems). In this paper the SSTS model is described and preliminary results are presented showing the effects of scintillation on a second order Costas loop. The Costas loop is commonly used in GPS receivers for tracking the phase of the GPS carrier.

Keywords: ionosphere; ionospheric irregularities; ionospheric scintillation; scintillation modelling

1. Introduction

The scintillation of radio signals due to their propagation through ionospheric irregularities is rapidly becoming an important issue for GPS receivers operating in equatorial regions where these irregularities occur. Irregularities in the electron density of the equatorial ionosphere have length scales ranging from a few meters to many kilometres, and can cause diffraction and refraction at GPS frequencies. These effects give rise to temporal fluctuations in the signal intensity and phase at the receiver and are referred to as scintillations. Strong scintillation conditions cause deep fading to occur in the signal intensity as well as rapid changes in the carrier phase. Such effects can severely degrade the performance of GPS receiver tracking loops and may even cause a complete loss of lock. The impact on a receiver's navigational accuracy will, however, depend on the number of receiver channels which have been affected, as well as the geometry of the remaining unaffected constellation.

The synthetic scintillation time series (SSTS) model has been developed in order to understand and quantify the effects described above. The model, which is described in Section 2, generates synthetic time series of amplitude and phase perturbations which are experienced by radio signals as they traverse the ionosphere under disturbed conditions. These data may then be input into models of various GPS receiver architectures and systems to determine how scintillation phenomena

[1]Wide Area Surveillance Division, Defence Science and Technology Organisation, Salisbury, SA 5108, Australia

[2]Tactical Surveillance System Division, Defence Science and Technology Organisation, Salisbury, SA 5108, Australia

1217-8977/98/$ 5.00 ©1998 Akadémiai Kiadó, Budapest

stress the receiver tracking loops and degrade the receiver performance. The detailed testing and modelling of GPS receivers is beyond the scope of this paper. However, preliminary results using a second order Costas loop to simulate a generic GPS receiver carrier tracking loop are presented.

2. The synthetic scintillation time series (SSTS) model

The approach used in the SSTS model is to characterise the signal statistically (i.e. the appropriate probability density functions and power spectra etc.) and then produce realizations of the data which conform to that statistical description. The Wide Band Model (WBMOD) of global scintillation activity (Secan et al. 1995), is used to generate various parameters describing the scintillation and ionospheric irregularities which are required by SSTS for the given conditions. In this manner, a complete environmental model of ionospheric scintillation is specified.

There are several important considerations in developing a model of scintillation time series. These are: 1. The amplitude and phase data must have appropriate PDFs, 2. Amplitude and phase data must be appropriately correlated e.g. large phase variations are observed when deep amplitude fading occurs, 3. The data must have appropriate power spectra, 4. The model should be based on a propagation theory of radio waves through turbulent media, and 5. As previously mentioned, the model should be related to the environment though parameters supplied by WBMOD. Each of these points will be considered in turn.

The probability density functions describing the scintillation of radio signals which have traversed a disturbed ionosphere are Nakagami-m for amplitude and Gaussian for phase (Fremouw et al. 1980, Whitney et al. 1972, Crane 1977). Respectively, these are given by:

$$P_N(r) = \frac{2m^m r^{2m-1}}{\Gamma(m) < r^2 >^m} e^{-mr^2/<r^2>} , \tag{1}$$

$$P_G(\phi) = \frac{1}{\sqrt{2\pi\sigma^2}} e^{-\phi^2/2\sigma_\varphi^2} , \tag{2}$$

where Γ is the gamma function, r and ϕ are the amplitude and phase of the signal, and σ_φ is the standard deviation of the phase fluctuations or the phase scintillation index. The m-parameter in the Nakagami-m distribution is related to the S_4 index by $m = 1/S_4^2$. For large values of m (small S_4) the Nakagami-m distribution approaches the Gaussian distribution. As S_4 increases, the Nakagami-m distribution tends toward the Rayleigh distribution and becomes Rayleigh when S_4 equals 1.0.

In order to fully describe the statistics of scintillating signals, a joint PDF of amplitude and phase is required. The reason for this is that one would expect the amplitude and phase fluctuations to be correlated to some degree. This is because as the amplitude fades, the phase becomes more variable and will eventually become meaningless when the amplitude falls to zero (i.e. the phase may take on any value). Thus, when large amplitude fading is observed, so too are large phase variations. It is important for this behaviour to be included in the generation of synthetic scintillation time series data because it is much harder for a receiver to

maintain lock on a signal when deep fading and large rates of change of phase occur simultaneously.

Various schemes have attempted to model the joint statistics of scintillating signals based on Gaussian and log-normal distributions for the amplitude (Fremouw et al. 1980). However, these schemes are quite complicated and do not describe the amplitude PDF as accurately as the Nakagami-m distribution which was designed specifically to describe intensity fading (Nakagami 1960). Due to the complexity of the joint statistics, a joint PDF incorporating the Nakagami-m distribution for amplitude and the Gaussian for phase has not been developed. The method that has been developed to include the joint statistics will not be described here except to say that it is not based on analytical techniques, but rather on Monte-Carlo methods. The technique will be described in detail in a subsequent paper.

The power spectra of scintillating signals is determined through an analysis of the propagation of the radio waves through a disturbed ionosphere. The parabolic equation method (PEM) (see e.g. Yeh and Liu 1982) is used to describe the propagation of radio waves through both the turbulent media and free-space to the receiver, while the effect of the turbulent media on the radio waves is determined from phase screen diffraction theory (Briggs and Parkin 1962, Buckley 1971a, 1971b, Rino 1979a, 1979b, 1982, Rino and Owen 1984, Yeh and Liu 1982). For a single thin phase screen the following expressions for the spatial power spectrum of the log-amplitude, χ, and phase departure, φ, of the radio waves at the receiver may be derived (Yeh and Liu 1982):

$$\begin{aligned}\Phi_\chi(\kappa_\perp) &= 2\pi L_s\lambda^2 r_e^2 \sin^2(\kappa_\perp^2 z/2k)\Phi_{\Delta N}(\kappa_\perp,0)\,,\\ \Phi_\varphi(\kappa_\perp) &= 2\pi L_s\lambda^2 r_e^2 \cos^2(\kappa_\perp^2 z/2k)\Phi_{\Delta N}(\kappa_\perp,0)\,,\end{aligned}\tag{3}$$

where L_s is the 'slant' thickness of the phase screen (i.e. the irregularity layer), z is the distance from the phase screen to the receiver, r_e is the classical electron radius, λ and k are the wavelength and wave number of the radio waves, and $\Phi_{\Delta N}$ is the 3-dimensional spatial spectrum of the ionospheric irregularities.

In order to proceed it is necessary to relate L_s to the thickness of the irregularity layer, L, and z to the height of the phase screen, h. The curvature of the Earth's surface must also be considered in this analysis. Figure 1 displays the geometry of the situation. From this figure it is possible to show that

$$z = [(h+R_e)^2 - (R_e+a)^2\cos^2\theta']^{1/2} - (R_e+a)\sin\theta'\,,\tag{4}$$

and

$$L_s = [(L+h+R_e)^2 - (R_e+a)^2\cos^2\theta']^{1/2} - [(h+R_e)^2 - (R_e+a)^2\cos^2\theta']^{1/2}\,,\tag{5}$$

where R_e is the radius of the Earth, a is the altitude of the receiver, and θ' is the elevation angle of the satellite as seen from the reciever. From simple trigonometry it may be shown that θ' is related to the elevation of the satellite, θ, by:

$$\tan\theta' = \tan\theta - \frac{a\sec\theta}{[(h_s+R_e)^2 - R\cos^2\theta']^{1/2} - R\sin\theta'}\,,\tag{6}$$

where h_s is the height of the satellite.

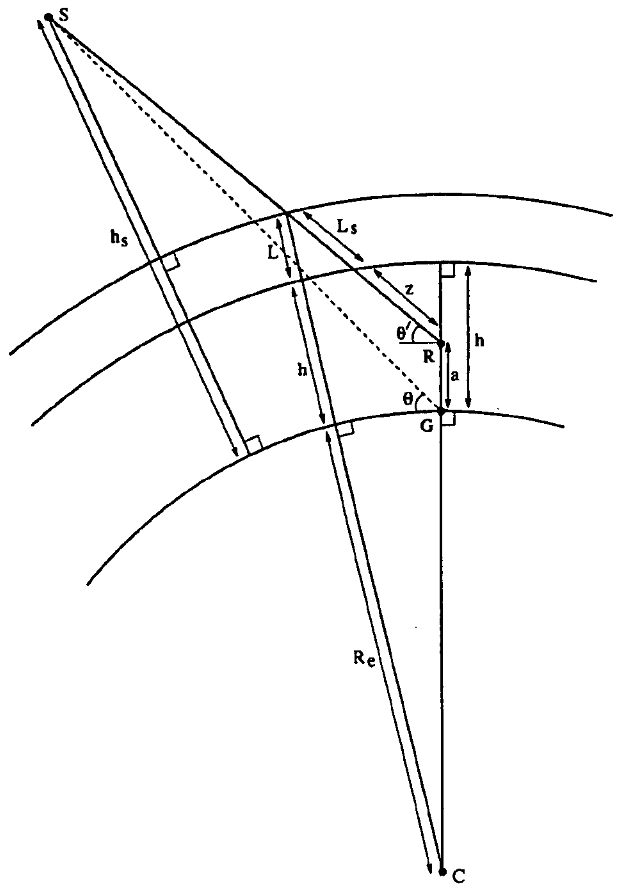

Fig. 1. Geometry of the signal propagation path where 'S' is the satellite, 'C' the centre of the Earth, 'R' the receiver, and 'G' the point on the ground directly below the receiver. See text for further details

An appropriate expression for $\Phi_{\Delta N}$ is now required. A fundamental requirement for the 3D-spatial spectrum is that it must have a breaking (or outer) scale, below which the spectrum drops off as a power law (the inertial range). From Tatarski (1961) we have the following:

$$\Phi_N(\kappa) = \frac{\sigma_N^2 l_0^3 \Gamma(p/2)}{\pi^{3/2}\Gamma((p-3)/2)(1+l_0^2\kappa^2)^{p/2}}, \tag{7}$$

where σ_N is the RMS fluctuation in the electron number density $\Delta N(\mathbf{r})$ about the background N_0, l_0 is the outer scale size of the structures, and p is the spectral index below the outer scale. An appropriate value for σ_N can be obtained from the

following equation (Rino 1979a, 1979b, Rino and Owen 1984):

$$\sigma_N^2 = \frac{C_s l_0^{(2-p)}\Gamma(p/2-1)}{8\pi^{3/2}\Gamma((p+1)/2)}, \tag{8}$$

where C_s is the irregularity strength defined at a wave number of 1 radian/m and is a function of altitude. From WBMOD one may obtain a value of the irregularity strength, C_k, defined at a scale of 1 km and at the altitude of interest (i.e. the height of the phase screen). This can then be converted into a value of C_s. Alternatively, σ_N may be ignored in the calculation of $\Phi_N(\kappa)$ and instead the final frequency power spectrum scaled such that the spectral strength at a frequency of 1 Hz, T is that supplied by WBMOD.

The above expression for $\Phi_N(\kappa)$ does not include an inner (or freezing) scale below which the power spectrum falls off more rapidly (the sub-inertial range). Whitter (1992) introduced a freezing scale by modifying Tatarski's result as follows:

$$\Phi_N(\kappa) = \frac{\sigma_N^2 l_0^3 \Gamma(p/2)}{\pi^{3/2}\Gamma((p-3)/2)(1+l_0^2\kappa^2)^{p/2}(1+l_0'^2\kappa^2)^{(p-p')/2}}, \tag{9}$$

where l_0' is the freezing scale ($l_0' < l_0$), and p' is the power law drop-off in the sub-inertial range ($|p' > p|$).

An alternative power-law irregularity spectrum with a freezing scale and a sub-inertial range is that introduced by Shkarofsky (1968) (see also Yeh and Liu 1982):

$$\Phi_N(\kappa) = \frac{\sigma_N^2(\kappa_0 l_0')^{(p-3)/2} l_0'^3 K_{p/2}(l_0'\sqrt{\kappa^2+\kappa_0^2})}{(2\pi)^{3/2}K_{(p-3)/2}(\kappa_0 l_0')(l_0'\sqrt{\kappa^2+\kappa_0^2})^{p/2}}, \tag{10}$$

where $\kappa_0 = l_0/2\pi$, $k_0 l_0' \ll 1$, and $K_n(x)$ is the n^{th}-order modified Bessel function of the second kind of argument x. Note that in this expression the sub-inertial range does not follow a power law with spectral index p', but rather an exponential drop-off. Thus only one spectral index parameter, being that for the inertial range, is required together with the inner and outer scale sizes to describe the power spectrum.

The current version of WBMOD (13.04) only supplies the power law index in the inertial range and the outer scale. Thus, for current version of the SSTS model, Ee. (7) is used to model the spatial spectrum of the irregularities. However, it is intended that in later versions of SSTS, information about the sub-inertial range will be included when it is made available by a more advanced version of WBMOD (Secan et al. 1995).

The frequency spectrum of the signal at the receiver is obtained from the spatial spectrum through the following equation (Umeki et al. 1977, Yeh and Liu 1982):

$$\Phi_{\chi,\varphi}(f) = \frac{1}{v_t}\int_{-\infty}^{+\infty} \Phi_{\chi,\varphi}(\kappa = 2\pi f/v_t, \kappa_y)d\kappa_y\,, \tag{11}$$

where v_t is the relative velocity of the irregularities transverse to the radio propagation path. The coordinate frame has been chosen such that v_t is in the x direction in the $x-z$ plane (the propagation path being in the z direction). The value of v_t is found from the velocity of the irregularities relative to the radio propagation path which is given by $\mathbf{v} = \mathbf{v}_d + \mathbf{v}_p$ where $\mathbf{v}_d$ is the drift velocity of the irregularities and $\mathbf{v}_p$ is the velocity of the ionospheric pierce point of the radio path due to motion of both the satellite and the receiver. For GPS, the component of $\mathbf{v}_p$ due to satellite motion is negligible and only receiver motion is required to be considered.

In the analysis so far, it has been assumed that the irregularities are isotropic. Generalisation to the anisotropic case is achieved by replacing κ^2 with $\alpha_u^2\kappa_u^2+\alpha_v^2\kappa_v^2+\alpha_w^2\kappa_w^2$, where $\alpha_u, \alpha_v\, \alpha_w$ are dimensionless scaling factors along each axis. The anisotropy of the irregularities in electron density are governed by the geomagnetic field. Consequently, a series of rotations is required to transform the (u, v, w) frame of the irregularities to the (x, y, z) frame used in the calculation of the frequency power spectra. A detailed discussion on this is given by Rino and Fremouw (1977).

As mentioned previously, the SSTS model is based on a single thin phase screen and single scattering of the radio waves. This is suitable for the case of weak scattering. However, we are interested in strong scattering, as it is under these conditions that a receiver will lose lock. Expressions for the amplitude power spectrum have been derived for the strong scattering case using thick multiply scattering phase screens (Gochelashvily and Shishov 1971, Taylor 1972, Rumsey 1975). The multiple scattering phase screen models describe the statistics of strongly scintillating signals much better than the single scattering models. Consequently, the multiple scattering approach is more appropriate for GPS analysis. However, the power spectra in the two regimes do not vary greatly. The effect of strong scintillation activity is to cause some de-correlation of the signal time series which leads to an enhanced contribution from the high frequency components of the power spectrum. The intensity probability density function, on the other hand, does vary considerably from the low to high scattering regimes, but this has already been incorporated into the SSTS model separately; the phase screen analysis is only used to generate the correct power spectra. Thus, considering that the only effect of using a single thin phase screen is to underestimate the contribution of the high frequency components of the scintillation time series, we consider that the use of this theory is justified as a first approach. The next stage of this work, however, will be to introduce a multiple scattering approach for the calculation of the power spectra.

This completes the specifications of the SSTS model. As mentioned earlier, WBMOD is used to supply the values of the various parameters required by SSTS. These are: S_4, σ_φ, r, L, h, p, l_0, C_k and $\mathbf{v}_d$. The altitude, dynamics and operating frequency of the receiver, which are also required by SSTS, are supplied by the user for a specific test. In addition, WBMOD requires various input parameters to be supplied including the receiver and satellite locations (latitude, longitude and altitude), the date and local solar time at the receiver, the frequency of the carrier (in this case the GPS frequencies 1575.42 and 1227.6 MHz), the duration over which the receiver requires phase stability, the percentile at which the scintillation levels are to be generated, the geomagnetic activity index (K_p), and the smoothed

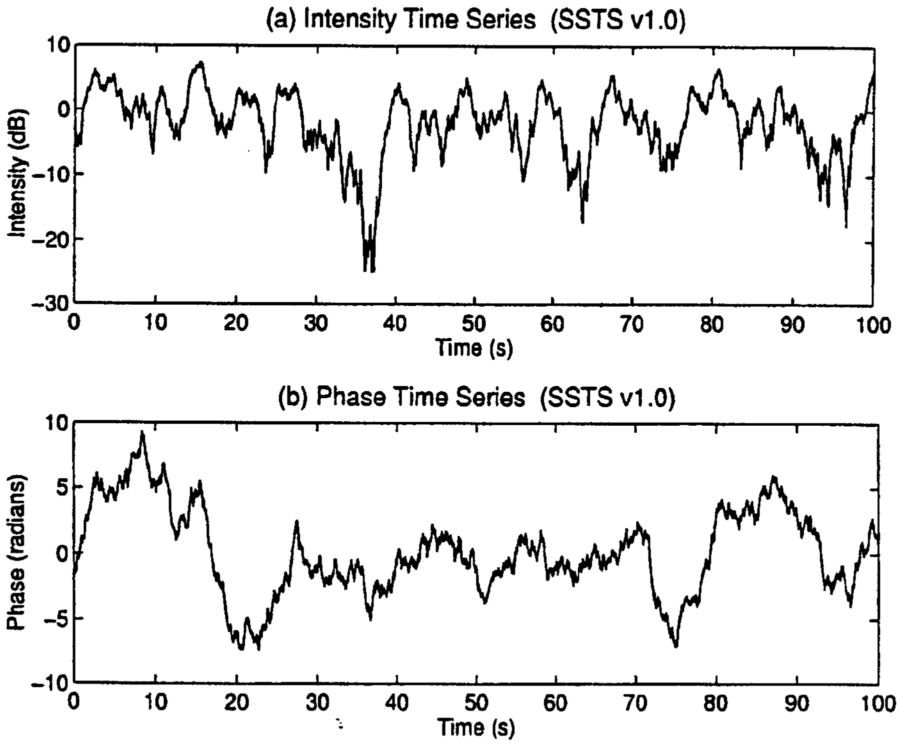

Fig. 2. Example of the SSTS model output showing intensity and phase scintillation (top and bottom respectively). See text for details

Zurich sunspot number (R_{12}). All of these parameters, except for the last two, are determined by the test scenario. The K_p index and R_{12} may be input as real or predicted values, both of which are supplied, for example, by the Ionospheric Predictions Service (IPS) of Australia.

3. Statistical verification of the SSTS model output

Before the SSTS model can be used to test GPS receiver tracking loops, it is important to verify that the model data has the correct statistics. Figure 2 displays an example of the output produced by the SSTS model with intensity scintillation shown in the top panel and phase scintillation in the bottom. The input values of S_4 and σ_ϕ were 0.90 and π radians respectively, the spectral slope (for both intensity and phase) was 2.30, and the time resolution was 0.01 s. Statistical analysis of the resultant model data yields an output S_4 of 0.89 ± 0.03 and a spectral slope of 2.32 ± 0.05. These are in good agreement with the input values. The output σ_ϕ is exactly π as the phase scintillation data is renormalised to the desired level.

Next we examine to probability density functions of the scintillation data. Figure 3 shows the PDFs of the modelled intensity (top) and phase (bottom) scintillation

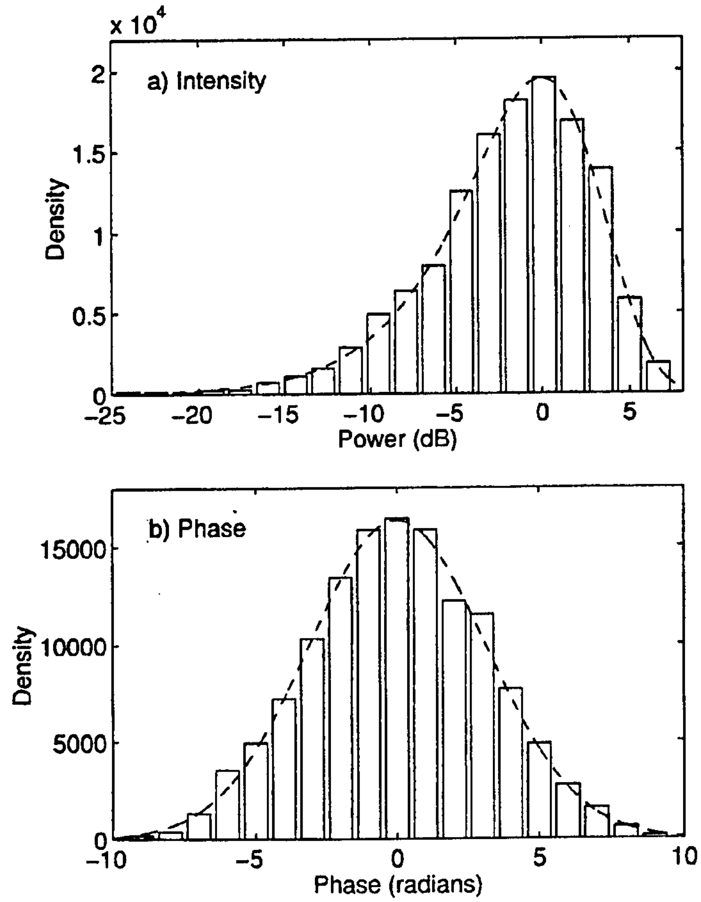

Fig. 3. Probability density functions for the modelled intensity (a) and phase (b) scintillation data of Fig. 2 with the expected PDFs overlaid (dashed lines)

data. In both cases the dashed line is the expected PDF (Nakagami-m with $m = 1.23$ and Gaussian with $\sigma = \pi$ respectively). Inspection by eye suggests that both the intensity and phase PDFs of the data are in good agreement with the expected PDFs. Formally we test the "goodness of fit" of the data to the desired functions using the χ^2 statistics which is given by:

$$\chi^2 = \sum_{i=1}^{N} \frac{(y_i - f_i)^2}{f_i}, \tag{12}$$

where the y_i are the observed values of the PDF, f_i are the expected values of the PDF, and N is the number of bins. The amplitude and phase PDFs have χ^2 values of 0.007 and 2×10^{-4} respectively. The small values yielded for χ^2 imply that we cannot reject the hypothesis that the observed PDFs are consistent with the expected PDFs, and this is the case even at a very low significance level.

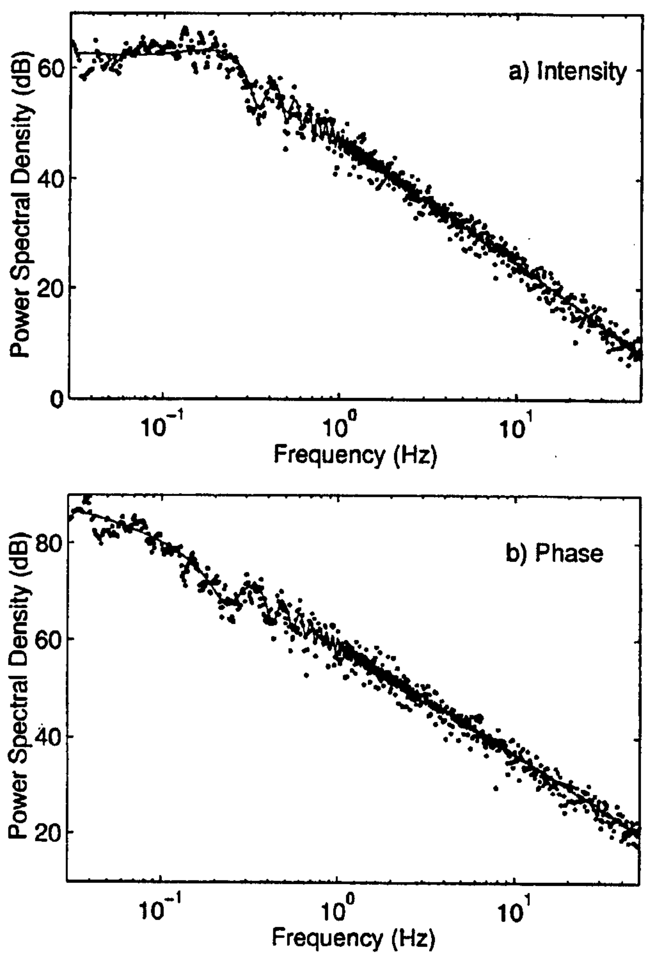

Fig. 4. Power spectra of the modelled intensity (a) and phase (b) scintillation data from Fig. 2 (dotted line) with the desired power spectra overlaid (solid line)

Finally, in Fig. 4 the power spectra of the modelled data are displayed (dotted line) together with the desired power spectra based on theory (solid line). Again it is clear that the model data is in good agreement with the desired result, a conclusion which was confirmed by an analysis of the χ^2 statistics for the power spectra.

4. Results from a second order Costas loop and discussion

The purpose of the SSTS model is to investigate the effects of scintillation on various GPS receiver systems. A thorough analysis of this sort is beyond the scope of this paper. However, in this section we show preliminary results from tests performed on a second order Costas carrier tracking loop with a bandwidth of 5 Hz and a pre-detection integration period of 20 ms. This sort of loop is typically used for carrier tracking in many GPS receivers.

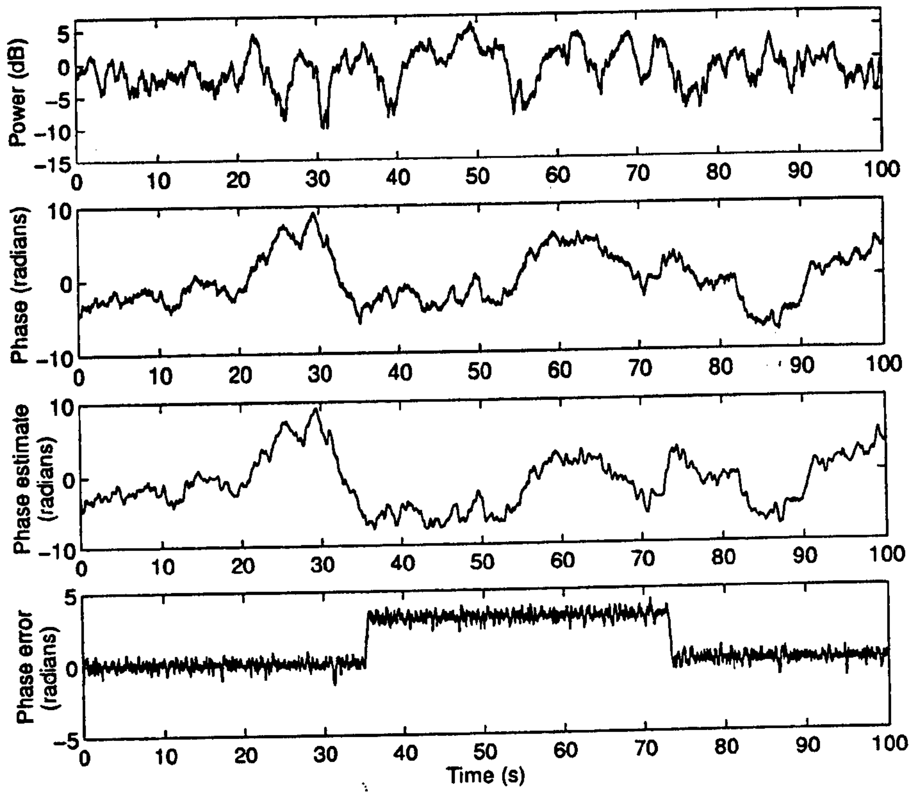

Fig. 5. Results from inputting SSTS model data ($S_4 = 0.6$, $\sigma_\phi = \pi$) into a second order Costas loop with a 5 Hz bandwidth. The top two panels show the input intensity and phase scintillation data respectively, the third panel displays the phase estimate of the Costas loop, and the bottom panel shows the phase error (difference between the input phase and the phase estimate). Note the incidents of cycle slips in the phase error which are indicative of the Costas loop experiencing difficulties in maintaining signal lock

For the results described in this section, the GPS signal power to noise density ratio (C/N_0) under quiescent conditions is set to 44 db Hz. This is based on a nominal GPS signal level of −160 dBW and a thermal noise density of −204 dBW Hz^{-1}. Factors which may reduce the C/N_0 such as antenna gain patterns, multipath, atmospheric absorption, and pre-amplifier noise, etc. have all been ignored. Other sources of loop stress such as Doppler (from satellite and receiver motion) and oscillator phase noise etc. have also been ignored. Suffice to say that in the presence of Doppler, a search algorithm would probably be required in order to recover the carrier phase once phase lock had been lost. It is also noted that in these tests, the levels of amplitude and phase scintillation were varied independently of one another. Although this does not represent a real physical process, it is nevertheless a convenient way of determining whether amplitude or phase scintillations have the greatest effect on loop performance.

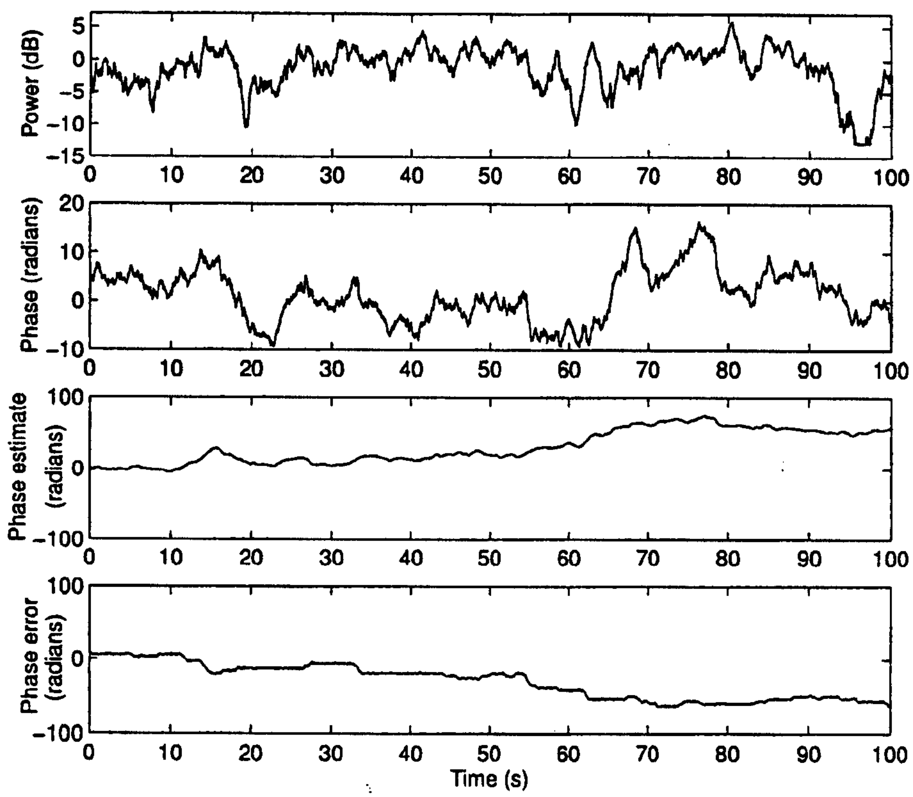

Fig. 6. As for Fig. 5 but with $\sigma_\phi = 2\pi$ radians. Note the increased severity of cycle slips in the phase error

First we examine the effect of phase scintillation on the Costas loop. Figure 5 shows results of feeding SSTS model data into the Costas loop with a moderate levels of S_4 (0.6) and σ_ϕ (π radians). It is apparent from this figure that the Costas loop is stressed and experiences cycle slips at times of 36 and 73 seconds. The phase error (which is the difference between the input phase and the loop phase estimate) jumps by π radians at these times (i.e. half a cycle). It is interesting to note that at these times the signal power does not experience any significant fading, and it is therefore concluded that the cycle slips are produced by phase scintillations.

Increasing the level of phase scintillation activity has a profound effect on the Costas loop. Figure 6 shows the loop response to phase scintillations for which $\sigma_\phi = 2\pi$ (the amplitude scintillation level is the same as in the previous example). We now observe that the occurrence of cycle slips has become so frequent that the phase error is drifting over a range of about 70 radians (11 cycles). With such frequent cycle slips, the loop can be considered to have lost lock on the carrier.

The bandwidth of the tracking loop is a significant factor in determining how well the loop tracks the carrier in the presence of scintillation, noise and Doppler. In the example just given, it was observed that a 5 Hz Costas loop lost lock on

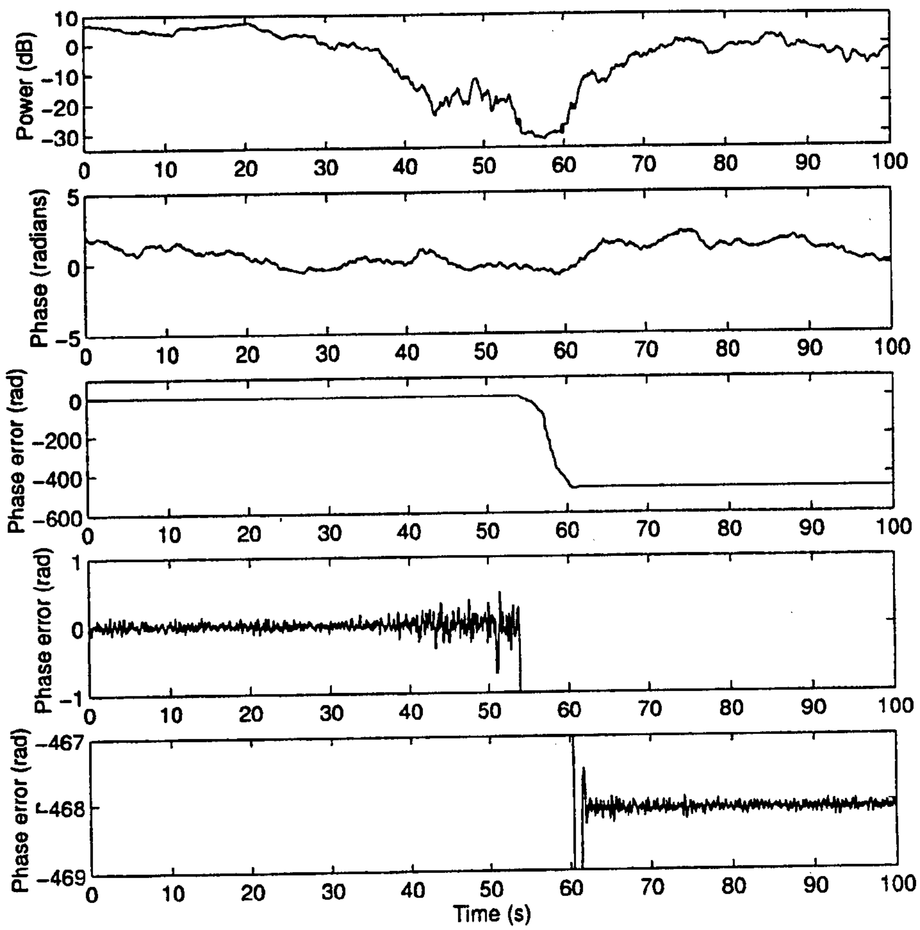

Fig. 7. Results from inputting high intensity scintillation model data ($S_4 = 0.9$, $\sigma_\phi = \pi/2$) into the Costas loop with a C/N_0 ratio of 44 db Hz. The irregularity drift speed has been decreased by a factor of 4 from the previous cases. See text for details

numerous occasions when the RMS phase scintillation strength was increased to 2π radians. However, under the same scintillation conditions, it was found that a loop with a 20 Hz bandwidth suffered no cycle slips (these results are not shown). The reason for this is that the wider bandwidth loop has less of a filtering effect on the phase scintillations and so tracks the high frequency components more accurately. Unfortunately, the wider bandwidth loop also allows more thermal noise through, and so is worse under strong amplitude scintillation conditions. Indeed, for any given combination of Doppler, phase and amplitude scintillation strength, an optimum loop bandwidth (and loop order) will exist which minimises the phase tracking errors. Determining the optimum bandwidth involves Weiner filter analysis and is beyond the scope of this paper.

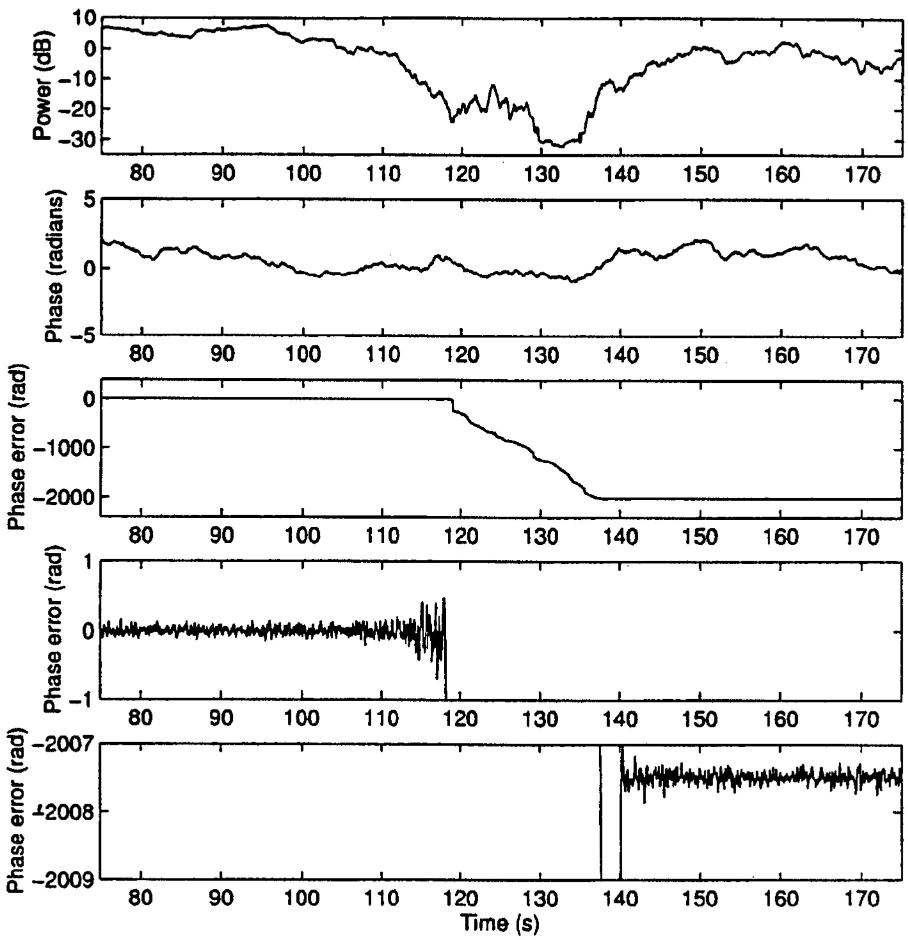

Fig. 8. As for Fig. 7 except in this case the C/N_0 ratio has been decreased to 35 db Hz. Note the increased length of time over which the Costas loop is not locked

We turn now to the effects of amplitude scintillation on the Costas loop. For a Costas loop with a 5 Hz noise bandwidth, the threshold C/N_0 for loss of lock is approximately 19 dB Hz (see e.g. Kaplan 1996). Consequently, for a quiescent C/N_0 of 44 db Hz, a sustained fading level of 25 dB would be required in order to force the loop out of lock (assuming that phase scintillation stresses are not also present).

Amplitude scintillation tests were performed with low, moderate and high levels of amplitude scintillation activity (S_4 of 0.2, 0.6 and 0.9 respectively) and low levels of phase scintillation (σ_ϕ of $\pi/2$ radians). In all cases we found no evidence that the Costas loop was stressed under these conditions (the results have not been displayed). At first glance, this suggests that the Costas loop is robust under even severe amplitude scintillation conditions. However, one must also consider that

the speed of the ionospheric irregularities transverse to the propagation path was relatively large (148 ms^{-1}). Consequently, the duration of the resulting deep fades in the amplitude time series were relatively short and the Costas loop was significantly stressed for only short periods of time.

Although the Costas loop was not adveresly affected by amplitude scintillations in the above example, it was seriously affected by strong phase scintillation as shown by the first two examples. This is because, under conditions where amplitude fading is rapid (i.e. the relative speed of the ionospheric irregularities transverse to the propagation path is large), the phase fluctuations will also be rapid. Thus, large rates of change of phase will be produced which introduce significant phase stress into the Costas loop.

The next logical step is to test the Costas loop under the same severe amplitude scintillation conditions as in the previous example, but now with a lower irregularity drift speed. These results are displayed in Fig. 7 where the irregularity drift speed has been reduced by a factor of 4 to 37 ms^{-1}. From a time of 37 s to 43 s the signal power drops to about –20 dB and remains near this level until nearly 53 s whereupon it drops below 30 dB. At a time of about 60 s, the signal power begins to recover. Over the initial period (i.e. 37–53 s), the Costas loop retains lock, but there is a significant increase in the noise on the phase error indicating that the loop is beginning to be stressed. Once the power falls below –25 dB, the Costas loop looses lock, and does not regain lock until a time of 62 s when the signal power has increased to –15 dB. The C/N_0 for recovery therefore seems to be higher than the threshold for loss of lock.

The above test was performed with a C/N_0 of 44 dB Hz which, is typical for a GPS satellite near zenith. It is expected that if the C/N_0 was reduced, representing, for example, a satellite close to the horizon, the Costas loop would lose lock earlier and require more time to recover. This is shown in Fig. 8 where the C/N_0 is set to 35 dB Hz but all other parameters and model data are identical to those used in the previous example. It is apparent that the Costas loop now loses lock at a time of 118 s when the signal level has fallen below –16 dB, and does not recover until 140 s when the signal power has increased beyond –10 dB.

5. Conclusion

In the first part of this paper we described, in detail, a model for generating synthetic scintillation time series using phase screen diffraction theory. It is intended that the global model of scintillation activity, WBMOD, will be used to supply input parameters for this model. The output of the SSTS model was tested against the desired statistical characteristics of real scintillation including the PDFs and PSDs and was found to produce results which where consistent with real scintillation activity. However, further research is required to determine ways of generating intensity and phase scintillation time series with the correct joint statistics. Also, the application of thick, multiply scattering phase screens to the SSTS model warrants further work.

Tests against a second order Costas loop found that factors such as loop band-

width and the irregularity drift speed influenced the loop's tolerance to scintillations. When the relative speed of the ionospheric irregularities transverse to the propagation path was small, intensity scintillations played a greater role in determining loop stress, while for large transverse speeds, phase scintillations had the greatest effect. These results were expected and are explained as follows. For large irregularity drift speeds transverse to the propagation path, deep fading of the signal power will be short in duration allowing the Costas loop to remain in lock. However, large drift speeds cause changes in carrier phase to become more rapid, thus increasing loop stress if appreciable phase scintillation activity is present. The reverse is true for small irregularity drift speeds, the carrier phase changes will be slower but the fades in the signal power will be longer in duration. Thus, in this case the amplitude scintillations will be more likely to cause the carrier tracking loop to lose lock.

Clearly then, the geometry of a given transmitter-receiver link is very important in evaluating the effects of scintillation on a receiver's tracking loops, along with the other physical parameters which describe scintillation activity. If the satellite is at zenith, the signal propagation path will be perpendicular to the motion of the ionospheric irregularities (assuming that the vertical drift speed of the irregularities is small) and the speed of the irregularities transverse to the propagation path will be at a maximum. As the satellite moves to lower elevations, the component of the drift velocity transverse to the propagation path will decrease monotically until a minimum is reached when the satellite is just above the horizon (again assuming that the vertical drift speed is small).

Finally we examined the effect of reducing the carrier-to-noise ratio of the quiescent GPS signal. This was done to simulate the effect of a satellite at low elevation angles. As expected, the loss of lock occurred at a smaller signal fading levels and recovery times were increased. This effect is of considerable importance when evaluating the response of GPS receivers to scintillation and their recovery performance. A follow on paper will investigate this in detail, together with the effects of satellite and receiver dynamics.

Acknowledgements

The authors would like to thank Drs Dick Thomas, Anthony Finn, and Chris Colemann for their helpful comments and discussions.

References

Briggs B H, Parkin I A 1962: *J. Atm. Terr. Phys.*, 25, 339–366.

Buckley R 1971a: *Aust. J. Phys.*, 24, 351–371.

Buckley R 1971b: *Aust. J. Phys.*, 24, 373–396.

Crane R K 1977: *Proc. IEEE*, 65, 181–199.

Fremouw E J, Livingstone R C, Miller D A 1980: *J. Atm. Terr. Phys.*, 42, 717–731.

Kaplan E D 1996: Understanding GPS principles and applications. Mobile Communications Series, Artech House

Nakagami M 1960: In: Statistical method in radio wave propagation, W C Hoffman ed., Symposium Publications Division, Pergamon Press

Rino C L 1979a: *Radio Sci.*, 14, 1135–1145.
Rino C L 1979b: *Radio Sci.*, 14, 1147–1155.
Rino C L 1982: *Radio Sci.*, 17, 855–867.
Rino C L, Fremouw E J 1977: *J. Atm. Terr. Phys.*, 39, 859–868.
Rino C L, Owen J 1984: *Radio Sci.*, 19, 891–908.
Rumsey V H 1975: *Radio Sci.*, 10, 107–114.
Secan J A, Bussey R M, Fremouw E J, Basu Sa 1995: *Radio Sci.*, 30, 607–617.
Shkarofsky I P 1968: *Can. J. Phys.*, 46, 2135–2153.
Tatarski V I 1961: Wave propagation in a turbulent medium. McGraw-Hill, New York
Taylor L S 1972: *J. Math. Phys.*, 13, 590.
Umeki R, Liu C H, Yeh K C 1977: *J. Geoph. Res.*, 82, 2752–2760.
Whitney J E, Aarons J, Allen R S, Seeman D R 1972: *Radio Sci.*, 7, 1095–1104.
Whitter L A 1992: Radio wave propagation in structured ionization for satellite and radar applications. Technical Report, Mission Research Corporation
Yeh K C, Liu C 1982: *Proc IEEE*, 70.

Acta Geod. Geoph. Hung., Vol. 33(1), pp. 41–51 (1998)

SPATIAL CHARACTERISTICS OF MID-LATITUDE IONOSPHERIC SCINTILLATIONS IN VHF RADIO-SATELLITE TRANSMISSIONS

L A HAJKOWICZ[1]

Simultaneous recordings of VHF radio-satellite transmissions from Transit satellites were obtained at three latitudinally displaced sites in the vicinity of Brisbane (36°S geom.lat): St.Lucia (S), Taringa (T) and Boreen Pt. (B). The meridional displacement were: S-T (2.12 km) and T-B (121.0 km). The location of the site B was such that it was almost directly under a field point MT (i.e. the point at an ionospheric height when the ray-path from a satellite to the site T was tangential to the magnetic field). A number of scintillation patches (so-called the P-type events), showing large enhancement (more than 10 dB) near the local magnetic zenith, were predominantly recorded at the sites S and T whereas the site B showed little or no scintillation activity. The anomalous situation is explained in terms of the geometry between the ray-path and magnetic field, associated with different positions of MT and MB (for the site B). It is suggested that the predominant effect in causing scintillation-producing irregularities becoming invisible from the site B, is associated with an alternative model of scintillation generation based on specular reflection of radio signal.

Keywords: field aligned irregularities; interference; mid-latitude scintillation; specular reflection

1. Introduction

The presence of small scale-size irregularities in the ionosphere (in the E and F regions) leads to rapid fading (scintillations) of VHF radio-satellite transmissions. Relatively little is known about mid-latitude scintillations as this region has been largely neglected in favour of auroral and equatorial scintillations where ionospheric disturbances are frequent. The early studies indicate that scintillation-producing irregularities, at southern mid-latitudes, are field aligned (Jones 1969, Parkin 1968, Singleton 1970).

All the previous study of mid-latitude scintillations did not differentiate between true mid-latitude scintillations and the fringe scintillations from the auroral and equatorial scintillation belts. It has been recently found that true mid-latitude scintillations are formed as patches (or longitudinally extended scintillation belts) which invariably occur equatorwards of a typical mid-latitude station (Hajkowicz 1994, 1997). The morphology of this type of scintillations (so-called P-type scintillations) is now more clear as a long-duration study of scintillations at a southern station Brisbane (36°S geom.lat.) is continuing. Specifically, P-type is almost an exclusive type of mid-latitude scintillations at sunspot minimum when fringe auroral scintillations are no longer visible from a mid-latitude site (Hajkowicz 1997). This type of scintillations is associated with the occurrence maximum of mid-latitude spread-F

[1]Department of Physics, University of Queensland, Qld. 4072, Australia

Table I. The location of three sites used for mid-latitude scintillation study

Station	Symbol	Lat. South deg.	Long. East deg.	Field point (Lat.) deg.
Taringa	T	27.477	152.974	25.9
St.Lucia	S	27.498	153.013	25.9
Boreen Pt.	B	26.288	153.000	24.7

which also reaches maximum at sunspot minimum. Some study on the association of spread-F and scintillations has been conducted by Bowman and Hajkowicz (1991) who linked the occurrence of specific type of spread-F related to field-aligned irregularities with the P-type scintillations.

The previous studies (Hajkowicz 1994, 1997) were concerned with the P-type morphology but did not provide information on the structure of irregularities responsible for these scintillations. Since 1993 three latitudinally displaced stations were used to detect the P-type in the vicinity of Brisbane. The results of these recordings start to emerge pointing out to a less recognised feature of scintillation-producing irregularities.

2. Method and results

Scintillation studies, using amplitude recordings from polar-orbit Transit satellites transmitting at a frequency of 150 MHz were conducted near Brisbane (27.5°S and 152.9°E geographic, 35.6°S invariant latitude) in 1993–1996. Table I gives the locations of the three sites in geographical coordinates. The sub-ionospheric locations (altitude: 300 km, Lat. South) of the points at which the ray-path from a satellite to a specific site is tangential to the magnetic field are shown (Field point).

The geographic locations are also shown in Fig. 1. The meridional distances are as follows: 2.12 km (T-S), 121.0 km (B-T). Note that the site T and S were also displaced in the E-W direction. The location of the field point MT (for the site T) is also shown. It can be seen that MT is about 0.4° north of the site B (at 25.9°S) thus being almost at the local zenith of the latter site. A corresponding point for the site B (MB) is further north at 24.7°S (not shown).

It has been evident over this solar cycle that a specific type of scintillations occurred at Brisbane. The so-called P-type scintillation events invariably had a characteristic structure as shown in Fig. 2a and b (also reported by Hajkowicz 1994 and 1997, and Bowman and Hajkowicz 1991). The distinct structure of the event is best seen from the raw VHF amplitude data which show a slow change in the signal strength as a transmitting satellite moves from the northern (equatorial) horizon to the southern (polar) horizon passing at its nearest point close to the local zenith (when signal is at maximum). It can be seen that the slow varying amplitude is modulated with fast fading (scintillations). A cursory look at the examples (Fig. 2) seem to indicate that a scintillation patch starts at lower latitudes,

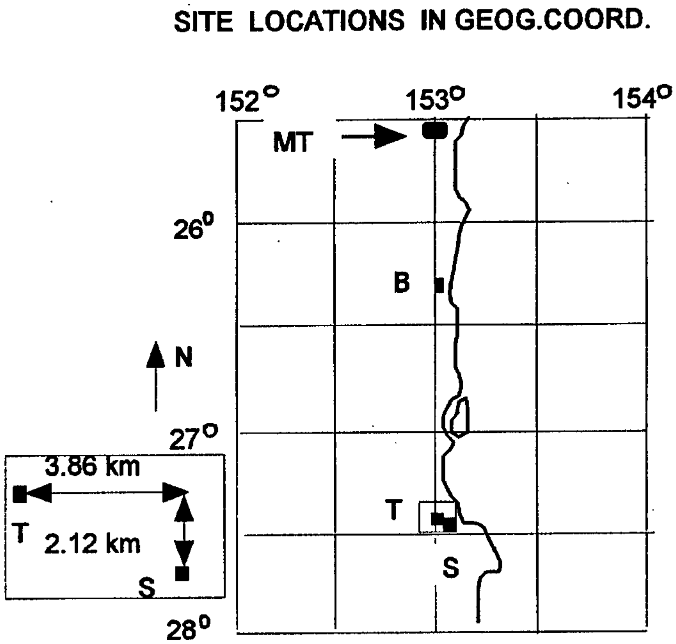

Fig. 1. The geographical position (South lat. and East long.) of three scintillation recording stations in the vicinity of Brisbane: S (St.Lucia), T (Taringa) and B (Boreen Pt.). The insert shows the relative location of the near-by sites T and S

north of the station, and terminates just slightly north of its geographical zenith. The assumption on the spatial extent of the event (whether it is strong as in Fig. 2a or weak as in Fig. 2b) is only apparent but not real. This assumption can be verified from noticing that all the P-type events (even as strong as that reported by Bowman and Hajkowicz 1991) terminate at approximately the same position, slightly short of the local zenith. It stands to reason that a hitherto unrecognised geometrical effect artificially limits the southern extent of the scintillation patch.

The locations of the three sites had a considerable effect on the recorded P-type scintillations as it can be seen from four typical examples in Fig. 3. The events were recorded at nighttime when a Transit satellite was passing close to the sites. In the first example (a-c) a scintillation event (reaching 15 dB peak-to-peak at maximum) showed similar scintillation structures at the sites T and S. Unexpectedly however, no corresponding scintillations were recorded at the northernmost site B; the event was invisible from this site. This situation was characteristic for other three events. Weak scintillations were recorded north the site B for the last event (j-m). A rare event is shown in (d-f) when a relatively small magnitude event (6 dB) at the site T was not registered even at the nearby site S. Note that the approximate maximum enhancement time at the site T (indicated as MT) coincided with the satellite's position when the ray-path was almost tangential to the magnetic field. It can be inferred from this that irregularities responsible for scintillations were field aligned.

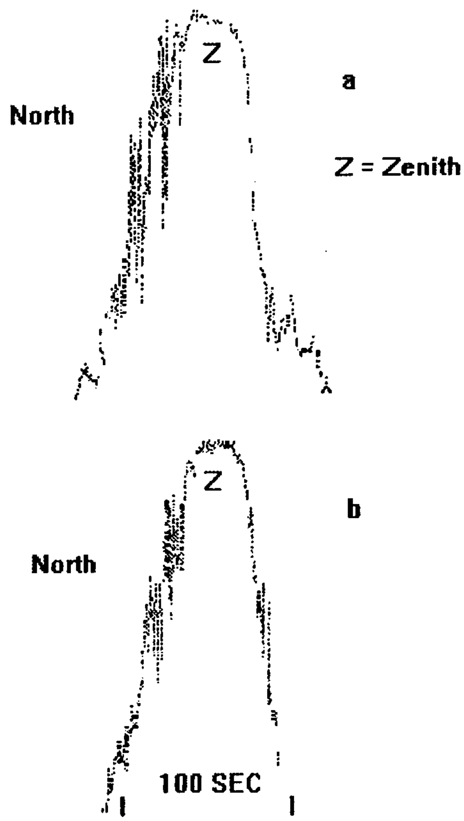

Fig. 2. Typical structures of the strong (a) and weak (b) P-type scintillations

Figure 4 shows yet another example of the same trend in scintillations. Note the scintillation enhancements at the field points MT (15 dB) and at MB (10 dB); the event recorded at the site B was not only smaller but much shorter than those at the sites T and S. It can be seen that there is no trace of scintillations close to the geographical zenith at the site T (indicated as ZT in Fig. 4a). The horizontal structure of this event can be seen from Fig. 5. The positions of the sub-satellite trajectories, as seen from sites T and B, are shown here in geographical coordinates. The satellite moved polewards, slightly East of the three sites. The regions of maximum enhancements, centred at the field points, are shown in relation to the sites B and T (MB and MT). Note that when the ray-path was sweeping over the region where MT is located no trace of scintillations was visible from the site B. Again a strong scintillation event, as observed from the two sites T, and S was not recorded at the site B.

Occurrence of mid-latitude scintillations is less frequent than at high and low latitudes and it was possible to record a relatively small number of the events at all three sites simultaneously (taking also into account instrumental failures and missing data). Altogether 10 simultaneous events were recorded indicating the

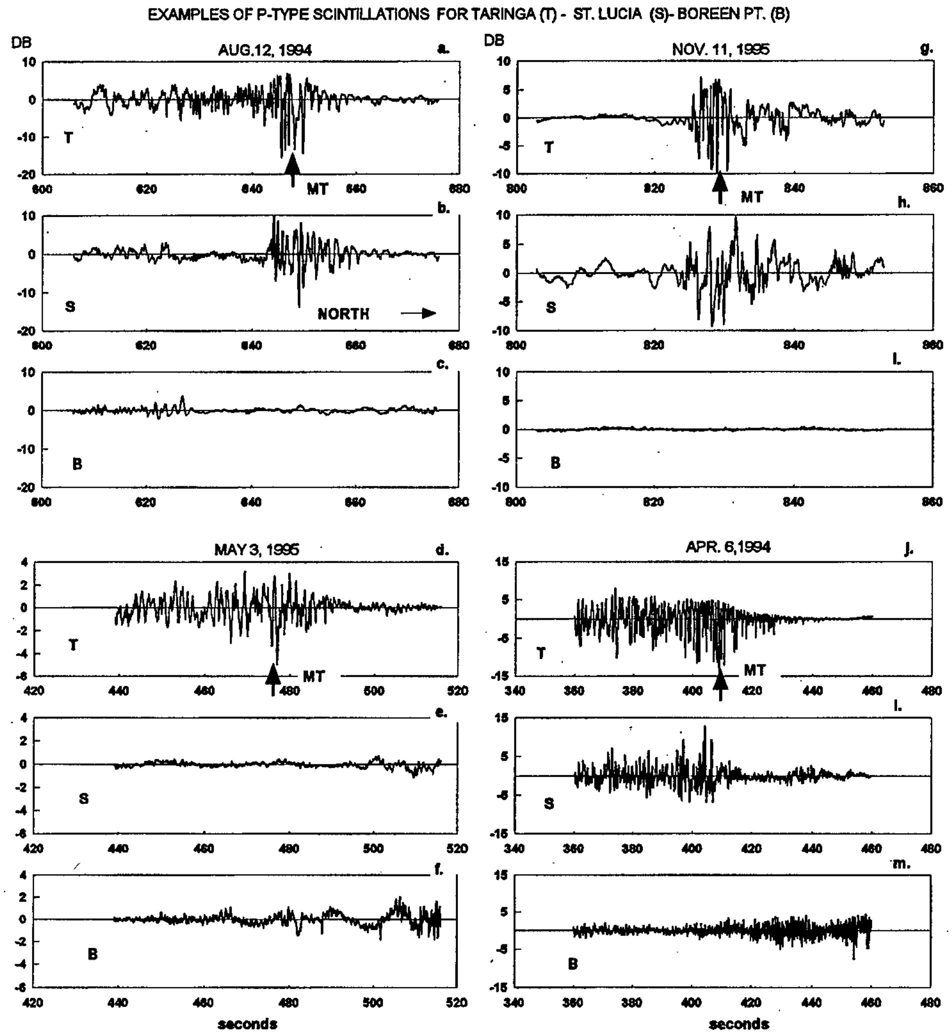

Fig. 3. Typical examples of simultaneous recordings of scintillations (or the absence of thereof) for the three sites:T, S and B. The positions of the field point MT (site T) and the satellite travel direction (North) are indicated

same trend as depicted in Fig. 3. On two occasions extensive scintillations, not resembling the P-type scintillations, were recorded simultaneously at all three sites. It is interesting that no case was recorded where an opposite effect took place, i.e. a case for which strong scintillations were recorded at the site B but without scintillations being recorded at the sites T and S.

Over 30 simultaneous P-type events were recorded at the two adjacent sites T and S. They all showed a patch-like structure being of similar magnitudes. The cross-correlation analysis applied to all the records indicated a relatively small cor-

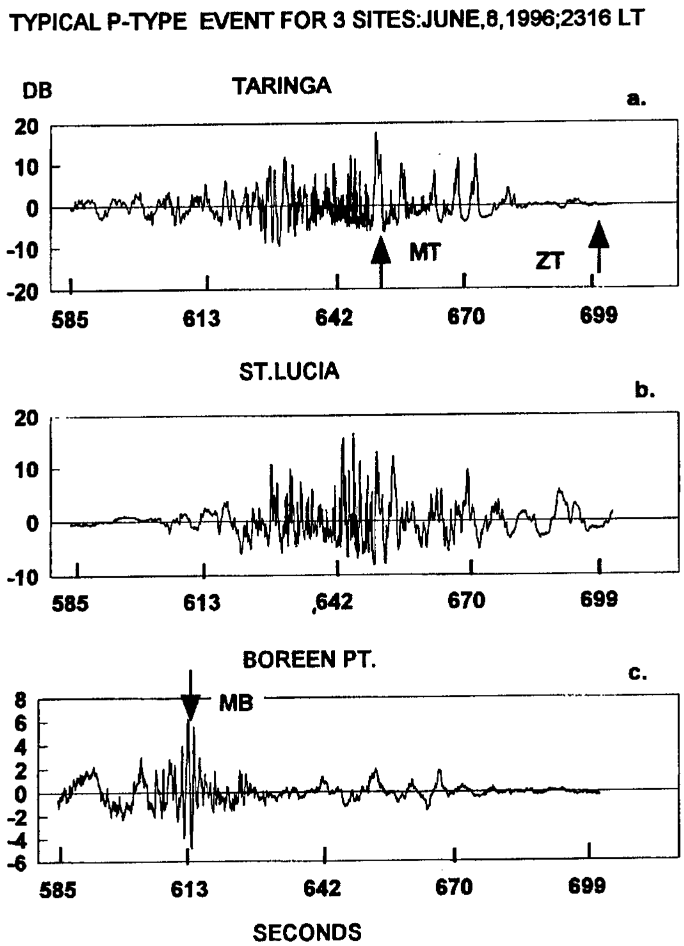

Fig. 4. A detailed structure of an event simultaneously recorded at three sites (symbols as for Fig. 3, ZT indicates the position of the geographical zenith at the site T)

relation coefficient ($r \leq 0.5$) of the fluctuations which is consistent with a relatively large separation of the sites. The similar trace displacement varied from about 3 sec to 0.1 sec, changing rapidly over the duration of each event. This precluded a height computation of the irregularity using the similar fade displacement. The scintillation enhancement at the field point was a characteristic feature of this event. Scintillations terminated rather rapidly polewards of the field point but continued equatorwards of it (cf. Fig. 2).

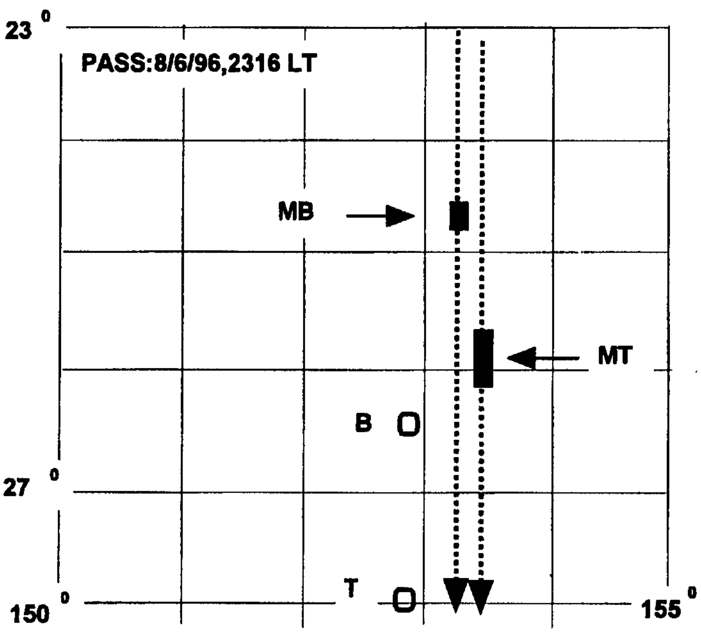

Fig. 5. The sub-ionospheric (altitude: 300 km) horizontal positions of scintillations regions as observed during a single pass from the sites T and B; the corresponding shaded areas refer to the scintillation enhancements close to the field points

3. Discussion and results

Relatively simple results from radio-satellite transmission recordings at the displaced mid-latitude sites point out to an unknown aspect of scintillation-producing irregularities. The effect of "invisible" irregularities was suspected but not demonstrated in the previous study. Parkin (1968) deduced from his mid-latitude scintillation study a hypothesis which is particularly relevant to the present findings. He stated: "It is clear that observations made close to the field-point will preferentially detect irregularities of large axial ratio. Irregularities of very large axial ratio may exist in the ionosphere and their r.m.s. deviation of electron density may be so small that they escape observation except at the field point." A similar postulate was given by Jones (1969) who noted that VHF scintillations occur in patches enhanced close to the magnetic zenith near Brisbane. He advanced a hypothesis: "Even when there is no observable scintillation activity there are weak patches of irregularities. The visibility of these patches are greatly enhanced when one looks in directions near the magnetic field direction."

The hypothesis on the possibility that scintillation-causing irregularities might become invisible under a certain configuration between the ray-path and magnetic field appears to be correct. Field-aligned irregularities which are visible from the sites T and S are not causing any scintillations at the site B since the latter site's field point is well shifted equatorwards from the other two field points. To demonstrate

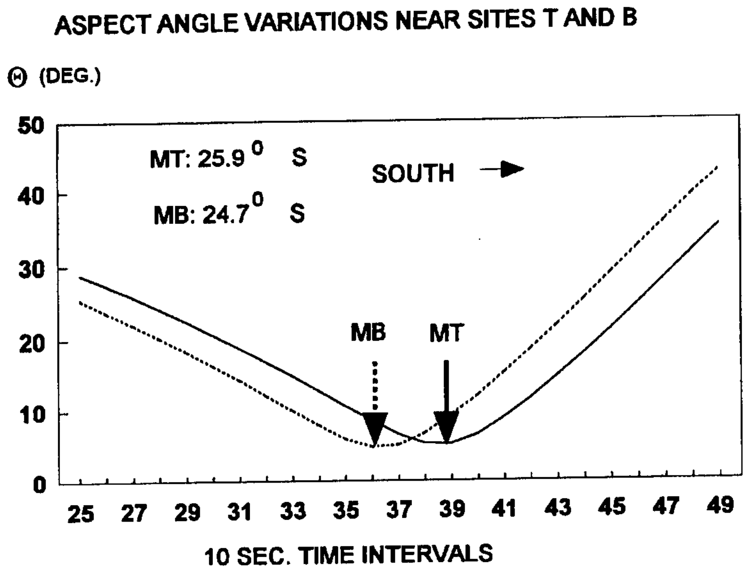

Fig. 6. Typical variation of the aspect angle Θ (i.e. the angle between the ray-path and magnetic field) during the time interval when a satellite in the vicinity of the sites T and B (solid and broken curves, respectively). The solid and broken arrows indicate the corresponding latitudinal locations of the field points MT and MB

this effect one must be first familiar with the variations of the aspect angle Θ (i.e. the angle between the ray-path and magnetic field) vs. satellite travel time (which can be translated to a latitudinal position). This can be seen in Fig. 6 for a typical satellite pass in the vicinity of the stations. The angle Θ increases rather rapidly polewards of the site T (solid line) and the site B (broken line); its increase is relatively slow equatorwards of the sites. Approximately, the field point for site T is located vertically above the site B; the irregularity which is seen almost along its axis from the site T at an angle Θ_T, is simultaneously seen at a certain larger angle Θ_B from the site B. From the aspect angle variations in the vicinity of the sites (Fig. 6b) it is found that $\Theta_T = 5°$ whereas $\Theta_B = 22°$.

The change in the aspect angle can be translated to a change of the ray-path length traversing the field-aligned irregularity (Fig. 7a). It appears from a mid-latitude scintillation study by Parkin (1968) that field aligned irregularities have axial ratios (i.e. the ratio of the length of irregularity to its transverse dimension) typically between 6–10 with the transverse dimensions in the range 0.5 to 1.0 km. In the positions S_1 and S_2 the satellite is overhead the sites T and B so that the ionospheric length $\Delta L \simeq 1$ km for the ray path S_1T (length CD) and S_2B (length EF). Clearly, the ionospheric length ΔL_0 (or the length AB for the ray-path S_3T) is then $\Delta L_0 \gg \Delta L$ which would lead scintillations at the site T being 8–10 dB larger (assuming the reported axial ratios) than for the site B (for the satellite positions S_2 and S_3).

An alternative explanation of the observed phenomenon is illustrated in Fig. 7b.

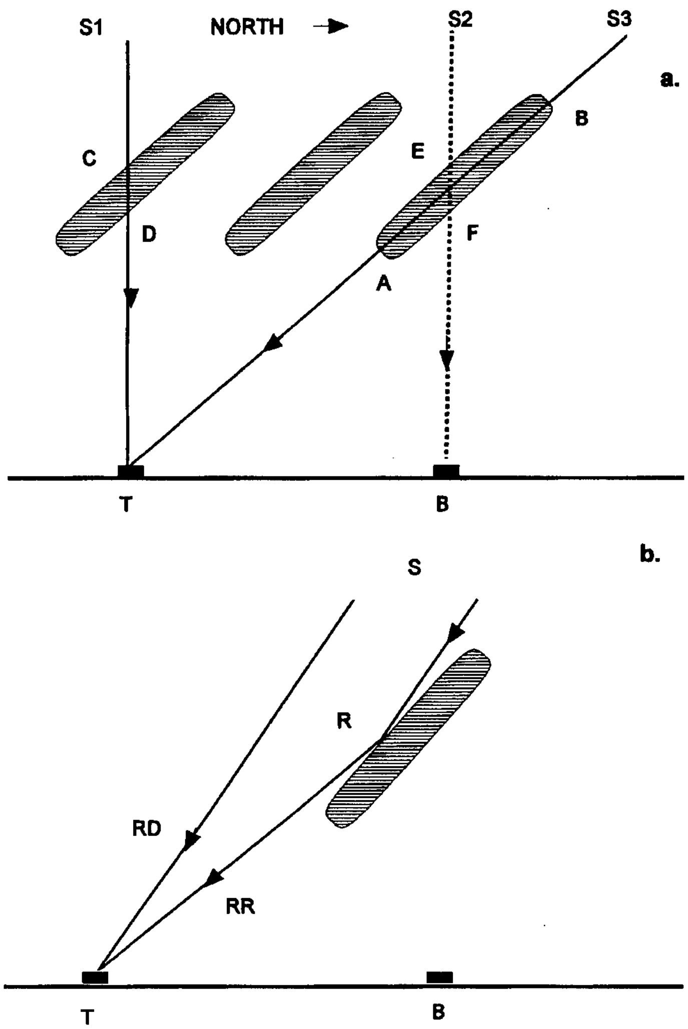

Fig. 7. A sketch of possible geometrical configuration between the ray-path from a satellite and the field-aligned irregularities. a) and b) show the diffraction and reflection interpretations of the observed phenomena

Here, the scintillation enhancement takes place at the site T only due to an interference between the direct (RD) and reflected (RR) rays. The strong interference effect takes place close to the field point since only then the angle of incidence to the surface of the irregularity is large (i.e. for the grazing angle g) which assures almost total reflection (as discussed further in the text). This effect will be absent for the site B at the position of the scintillation maximum for the site T. Absence of scintillations at the site B also indicates that the field-aligned irregularities are relatively weak and do not generate noticeable scintillations due to the diffraction

effect (i.e. for the ray-path intersecting the irregularity as in Fig. 6a). Unless the inhomogeneous ionization cloud, with the embedded field aligned irregularities, continues well past the site B towards the field point MB no scintillation activity will be recorded at this site. The case shown in Fig. 4 indicates that the equatorward limit of irregularities extended to the position MB but irregularities were weaker than those at higher latitudes. It can be thus assumed that the ionization cloud responsible for the P-type events extended to about 25°S (or 33°S geom. lat.). The termination of scintillations close to the geographical zenith at the sites T and S would indicate that the geometry of the ray-path becomes unfavorable to detect irregularities past this point (for the same reason that they were not observed at the site B). Thus, the polewards extent of the cloud cannot be established from the present recordings as one needs a fourth station positioned several degrees further south from the site T.

The presence of scintillations at one site only seems to confirm that the specular reflection model is more appropriate to explain the observed phenomena. This can be seen in Fig. 3 d-f where a weak PN-type event at the site T was not recorded at the nearby site S. The change in the path length trough the irregular region for these sites will be very small as they are adjacent therefore the ionospheric path length should be the same.

An alternative explanation of the selective scintillation occurrences was discussed by Rush and Colin (1958). They postulated that field-aligned ionospheric irregularities can cause strong specular reflections of radio waves in the VHF/UHF range provided that the ray-path is at a grazing angle (g) to the reflecting surface. An interference effect between the direct and reflected rays could lead to a sharp scintillation increase in a narow cone near the field point. They calculated that for small ionization density $N = 10^{11}$ el./m^3 the maximum angle g is about 1° but it increases to about 45° at $N = 10^{14}$ el./m^3. Clearly, for the case of a weak scintillation event shown in Fig. 3 d-f the ionization density was low and therefore even a small change in the angle would determine the presence or absence of the reflection effect. It follows that the ray-path in this case was better aligned with the irregularity axis for the site T than for the site B.

The specular reflection model of generation of the P-type events was originally suggested by Parkin (1968). He found serious discrepancies between his experimental results and the results provided by the classical diffraction theory for generation of scintillations (Briggs and Parkin 1963). Namely to obtain the scintillation enhancement of the magnitude he found it would be necessary to have field aligned irregularities extending almost to the altitude of a transmitting satellite which is clearly unacceptable (even for the fact that the curvature of the field lines must be then taken into account whereas the ray-path is a straight line). It prompted him to suggest that another mechanism, such as specular reflection and interference, should be considered. No theory of this effect has been developed yet. It stands to reason that both mechanisms diffraction and specular reflection (as discussed in association with Fig. 7) may contribute to the observed scintillation observation discrepancy from the sites T and B.

Acknowledgements

I am grateful to Mr M Francis, Mr H Lorek and to the technical staff of the Departmental electronic workshop for the design and completion of the time synchronised satellite recording system used in this project. The financial support was given by Telstra, Australia. The computer software used in the scintillation analysis and in the satellite prediction was written by Mr I Mortimer, Dr K L Jones and Mr M Keir.

References

Bowman G G, Hajkowicz L A 1991: *J. Atmos. Terr. Phys.*, 53, 447–457.
Briggs B H, Parkin I A 1963: *J. Atmos. Terr. Phys.*, 25, 339–365.
Hajkowicz L A 1994: *J. Atmos. Terr. Phys.*, 56, 391–399.
Hajkowicz L A 1997: *J. Atmos. Terr. Phys.* (in press)
Jones K L 1969: *Planet. Space Sci.*, 17, 585–593.
Parkin I A 1968: *J. Atmos. Terr. Phys.*, 30, 1135–1142.
Rush S, Colin L 1958: *Proc. I.R.E.*, 46, 356–357.
Singleton D G 1970: *J. Atmos. Terr. Phys.*, 32, 789–803.

Acta Geod. Geoph. Hung., Vol. 33(1), pp. 53–60 (1998)

LATITUDINAL TEC PROFILES OVER ARGENTINA BASED ON NNSS DIFFERENTIAL DOPPLER MEASUREMENTS DURING THE PERIOD 1994–1996

N JAKOWSKI[1], H-G KUGLAND[1], S SCHLÜTER[1], V H RIOS[2], R INZIRILLO[3], R LEITINGER[4]

Differential Doppler measurements at the NNSS 150/400 MHz radio beacons were used to derive latitudinal profiles of TEC over Argentina. The measurements have been carried out in the frame of the German/Argentinean TECUA project. During this project NNSS receivers were installed in Argentina along a meridional chain at different places such as Tucuman, Mendoza, Trelew, and Ushuaia.

The selected observation sites are suited to monitor the total ionization of the ionosphere over South America in the latitude range 15° – 65° S. Calibrated TEC profiles were obtained by applying the two-station-calibration technique.

To derive the mean diurnal and latitudinal variation of the ionosphere over Argentina, the observations are monthly averaged over the whole observation period. The observations near 60 W longitude indicate the position of the southward crest region at about 20–30° S. The observations are discussed and compared with corresponding TEC data computed from the IRI95 model.

Keywords: differential Doppler measurements; IRI 95; NNSS; total electron content, TEC

1. Introduction

The begin of the installation of a NNSS receiver network in Argentina within the TECUA project and preliminary results have been reported earlier (Jakowski et al. 1994).

The differential Doppler measurements made within the TECUA project at different stations along a meridional chain cover the period March 1994 – December 1996. All the stations which were included in the measuring program for a certain time are listed in Table I and indicated in a geographical map shown in Fig. 1.

It becomes clear that the distribution of receiving stations is well suited to monitor the ionosphere in the latitude range 15 – 65°S over the South American sector, thus including mid-latitudes as well as the crest region of the equatorial anomaly. Up to now only a few long-term TEC observations have been made over South America under low solar activity (LSA) conditions by Grimolizzi (1980). More knowledge about TEC variations is available for high solar activity conditions (Ezquer and Ortiz de Adler 1989).

This study is an attempt to give a first-order-estimation of the latitudinal dependence of TEC over South America under low solar activity conditions. It should

[1]Deutsches Zentrum für Luft-und Raumfahrt e.V., Fernerkundungsstation Neustrelitz, D–17235 Neustrelitz, Germany
[2]Universidad Nacional de Tucuman, Instituto Fisica, 4000 Tucuman, Argentina
[3]Universidad de Mendoza, IEMA, 5500 Mendoza, Argentina
[4]Karl-Franzens-Universität Graz, IMG, A–8010 Graz, Austria

1217-8977/98/$ 5.00 ©1998 Akadémiai Kiadó, Budapest

Table I. TECUA receiving ground stations

Station	Abbr.	φ [°S]	λ [°W]
Salta	SA	24.7	65.4
Tucuman	TU	26.8	65.2
Mendoza	ME	33.0	68.8
Trelew	TR	43.2	65.3
Ushuaia	UA	54.9	68.3

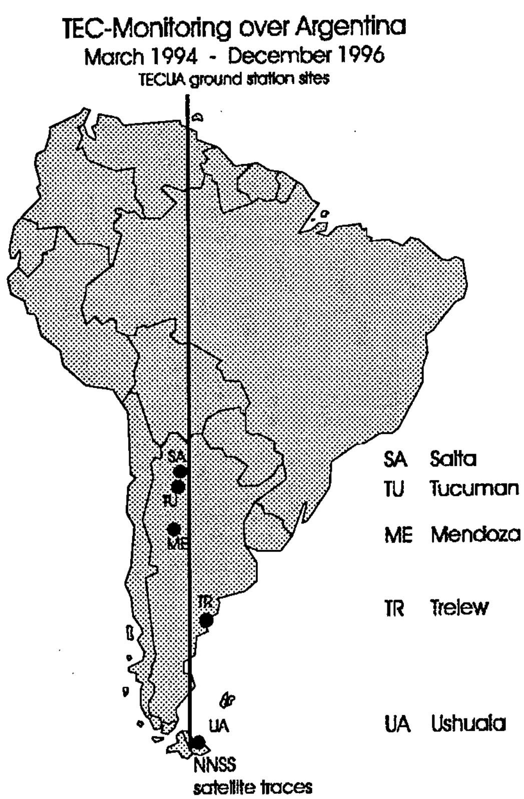

Fig. 1. Distribution of TECUA receiving stations of NNSS satellites over Argentina

be mentioned that these results are provisional since the data analysis has not yet been finished.

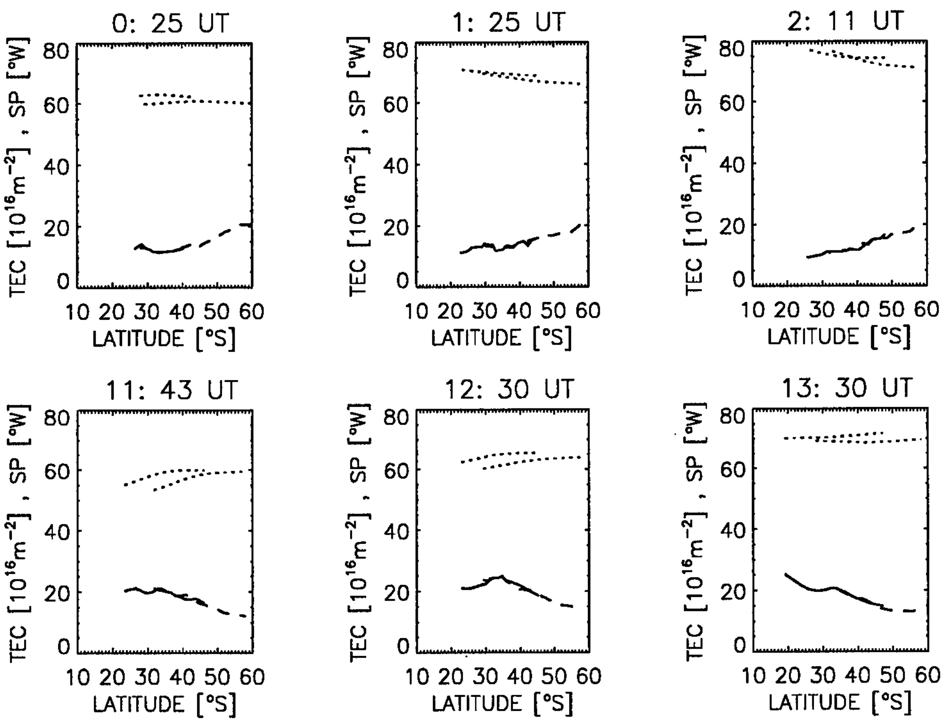

Fig. 2. Subsequent latitudinal profiles of TEC derived from observations at the Mendoza and Trelew stations on December 2, 1994. The traces of the subionospheric points are shown on the top by dotted lines

2. Data analysis

The differential phase measurements on the coherent 150/400 MHz frequency signals transmitted by the NNSS satellites provide the original data base for the estimation of the total electron content (TEC) of the ionosphere. Unfortunately the number of available satellites was decreasing during the observation period from 7 at the beginning to 3 transmitting satellites in December 1996 due to the declining phase of the TRANSIT satellite navigation system which is now completely replaced by the Global Positioning System (GPS). Applying the two-station-calibration-method (Leitinger et al. 1975), absolute TEC data can be derived from the measurements obtained at well-spaced stations.

Due to a number of data gaps at singular stations, an absolute calibration of TEC was not possible for all satellite passes. In this report we have used only reliable results of two-station-calibrations. Additional results will be saved after a more careful screening and correcting of the original observational data. To have more representative data for the regular behaviour of the ionosphere, the derived TEC data are averaged over certain observational periods. In order to discuss the observations in relation to commonly used models of the ionosphere, we have compared the data with corresponding IRI95-derived TEC data.

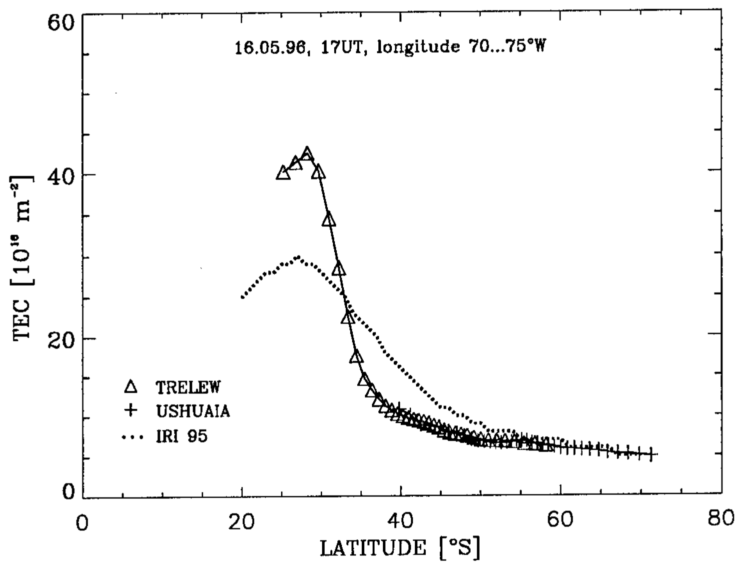

Fig. 3. Latitudinal TEC profiles derived from measurements at the TECUA stations Trelew and Ushuaia on May 16, 1996, 17 UT compared with corresponding IRI95 model data

3. Results and discussion

The NNSS measurements provide a lot of individual snapshots of the latitudinal TEC profile over South America, illustrated in Figs 2 and 3. The TEC profiles in Fig. 2 which are derived from observations at the TECUA stations Mendoza and Trelew give an impression of the latitudinal TEC-structure during late-evening and morning hours on an arbitrarily selected day in summer. The longitude range of the trace of the subionospheric points (SP) is shown in the upper part of the plots by dashed lines. It is interesting to note that the trend of the TEC profile reverses during night-time, probably related to enhanced geomagnetic activity ($A_p = 24$).

Figure 2 shows a well pronounced crest at about 27°S which corresponds with the latitude of the Tucuman station. As it should be expected, the data of the Trelew and the Ushuaia station match quite well indicating a reliable TEC calibration. The comparison with the corresponding values of the IRI95 model indicates a much more smooth behaviour of the model around the crest which is typical for an average profile.

Compared with modern GPS-techniques applied for TEC estimation (e.g. Jakowski et al. 1996), the disadvantage of NNSS observations is their discontinuity in time since the discussion of dynamical processes developing in space and time requires a fast sequence of measurements. Unfortunately, due to the reduced number of satellites the sequence was rather poor at the end of the project phase. But nevertheless, due to the high latitudinal resolution of TEC illustrated in Figs 2 and 3 it is valuable to discuss the actual measurements in comparison with the 'normal' behaviour provided by averaged data. So we confine our attention in this

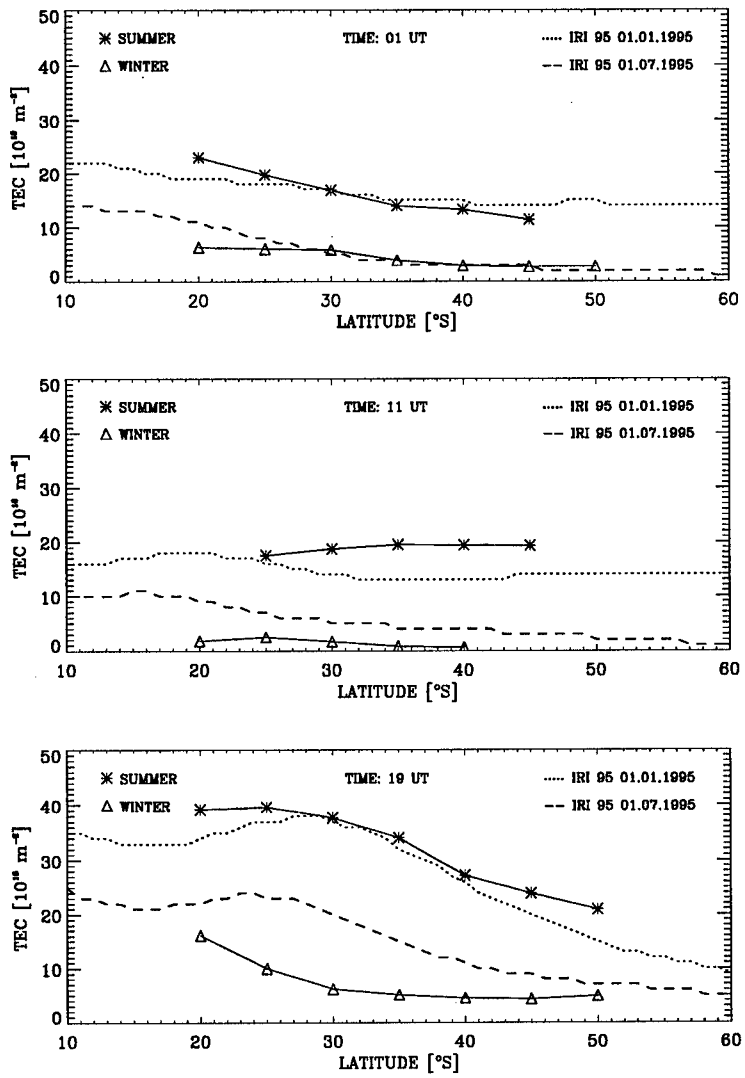

Fig. 4. Latitudinal profiles of TEC averaged over winter and summer month's including all satellite passes with SP traces inside $55° < \lambda_{sp} < 78°$W longitude range within the observation period March 1994 – December 1996

paper to the estimation of the average behaviour which will be the reference for future studies of more dynamical processes such as ionospheric storms.

Averaged longitudinal profiles are shown in Fig. 4 under different time conditions. It has to be mentioned that the data basis for the averaging includes all NNSS passes whose subionospheric traces are in the longitude range $55 < \lambda_{sp} < 78°$W. So the mean Local Time corresponds with LT = UT – 4.4 (hours). Due to considerable differences in the seasonal behaviour, we consider TEC under winter (6,7) and summer (12,1) conditions separately.

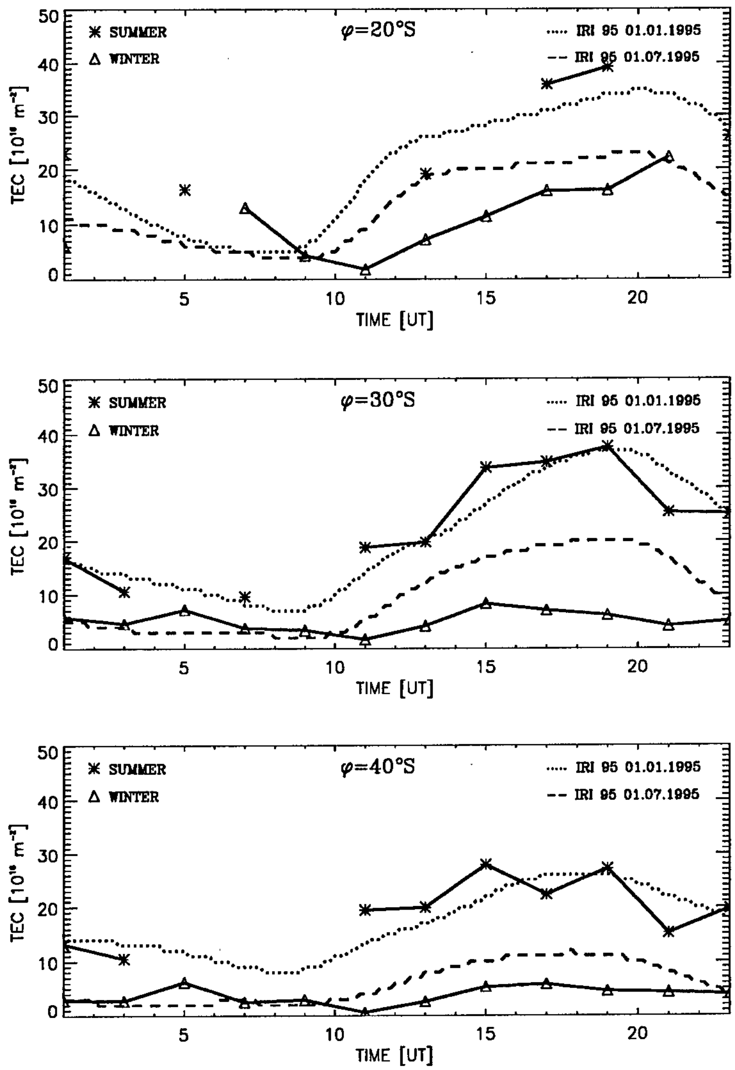

Fig. 5. Diurnal variation of TEC two hourly averaged over winter and summer month's including all satellite passes with subionospheric point (SP) traces inside $55^\circ < \lambda_{\mathrm{SP}} < 78^\circ$W longitude range within the observation period March 1994 – December 1996

In the late evening hours (01 UT) the observations fit IRI95 values very well at latitudes southward from 25°S both for summer as well as for winter conditions. The situation is quite different at 11 UT just before sunrise. All this time the IRI95 values overestimate TEC during winter and underestimate TEC in summer by about $3 - 6 \cdot 10^{16}$ m^{-2}. For a more detailed discussion of these differences near sunrise the longitude range of selected satellite passes covering about 1 1/2 hours, has to be reduced. Whereas at 19 UT the summer values match quite well, the

winter TEC data of IRI95 and TECUA observations differ considerably by more than $10 \cdot 10^{16}$ m^{-2} especially around $25-30$°S. The observations indicate no crest at this time. The rather low TEC level in winter is quite different from observations made near the Northern crest region at the Asian sector under LSA-conditions, whereas the summer level again agrees quite well (Huang et al. 1989).

No systematical comparison with the individual TEC profiles discussed by Grimolizzi (1980) is possible. However, the corresponding TEC data obtained under winter conditions over the Tucuman region by Grimolizzi indicate also a rather low TEC level.

As Fig. 5 shows, the overestimation of TEC by the IRI95 model in winter is a systematical effect practically for all latitudes considered here at daytime hours. The summer values fit sufficiently well, indicating that IRI95 provides a good description of the ionosphere over this area under summer conditions.

4. Summary and conclusions

NNSS differential Doppler measurements carried out within the TECUA project provide TEC data over South America in the latitude range 15 – 65°S within the time period March 1994 – December 1996. The derived latitude profiles of TEC indicate the appearance of a well developed crest in the latitude range 20–30°S during the afternoon/evening hours. Observations obtained during the whole measuring campaign are averaged and compared with corresponding IRI95 data. The results are typical for low solar activity conditions.

Generally speaking, both the derived latitudinal profiles as well as the diurnal variations of TEC in summer agree quite well with IRI95. In winter IRI95 overestimates TEC (up to a factor of 3) at all latitudes considered here during day-time under low solar activity conditions which are typical for the whole TECUA measuring campaign.

Acknowledgements

The project was sponsored by the Bundesministerium für Bildung und Forschung of Germany through the International Bureau headed by H Bianchi of the GKSS Research Center Geesthacht.

Besides the participating institutes we thank the Base Aeronaval Almirante Zar, Trelew and Tte G Caramanan from VAG station Ushuaia for providing infrastructur and support to operate the TECUA receiver during the measuring period. NNSS receiver were kindly provided by the TU Berlin, the University of Bonn and by the AWI Bremerhaven.

References

Ezquer R G, Ortiz de Adler N 1989: *J. Geophys. Res.*, 94, 9029–9032.

Huang Y-N, Cheng K, Chen S-W 1989: *J. Geophys. Res.*, 94, 13515–13525.

Jakowski N, Kugland H-G, Puliafito J L, Inzirillo R, Leitinger R, Maderbacher R, Rothleitner W, Hartmann G K, Degenhardt W, Rios V H, Manzano J R, Smilauer J 1994: In: Proc. Intern. Beacon Sat. Symp., L Kersley ed., Aberystwyth, UK, 242–245.

Jakowski N, Sardon E, Engler E, Jungstand A, Klähn D 1996: *Ann. Geophys.*, 14, 1429–1436.

Leitinger R, Schmidt G, Tauriainen A 1975: *Zeitschr. Geophysik*, 41, 201–213.

Pakula W A, Anderson D N, Beaudet M, Bendito J, Doherty P H, Eicher J, Fougere P F, Hughes L F, Inzirillo R, Jakowski N, Kapel M, Klobuchar J A, Kuenzler H, Kugland H G, Lottig C, Leitinger R, Maderbacher R, Manzano J R, Raymund T D, Rios V H, Sheehan R, Trepanier B, Valladares C, Whitfield J 1994: In: Proc. Intern. Beacon Sat. Symp., L Kersley ed., Aberystwyth, UK, 266–269.

Acta Geod. Geoph. Hung., Vol. 33(1), pp. 61–73 (1998)

LATITUDE DEPENDENT MEAN IONOSPHERIC HEIGHT — A NEW APPROACH TO THE TEC EVALUATION FROM NNSS DATA

R LEITINGER[1], P SPALLA[2], L CIRAOLO[2]

The evaluation procedures for NNSS Differential Doppler data normally use a fixed ionospheric height (usually of 400 km; considerably larger heights have to be used in the equatorial anomaly region).

An iterative procedure allows the use of latitude dependent mean ionospheric height, h_i. If a reasonable model can be used from which to derive the latitude dependence of the F layer peak height, h_m, the formula $h_i = h_m + 50$ km leads to a reasonable model for $h_i = h_i(\phi)$.

We demonstrate that such an approach leads to improvements in the latitude dependence of vertical electron content in cases of comparatively large station to station differences of TEC. The most important region in which the iterative procedure should be applied is the low latitude region, especially in the vicinity of a peak of the equatorial anomaly.

Keywords: ionospheric height; latitude dependence; NNSS; TEC

1. Introduction

Vertical electron content (TEC) is an important indicator for the overall ionization status of the ionosphere. At least over Europe we have only navigation satellites as data sources: the modern "Global Navigation Satellite Systems" (GNSS, presently the US system GPS and its Russian equivalent GLONASS) and the remaining active satellites of the former US Navy Navigation Satellite System (NNSS). GPS and GLONASS have satellites in orbit heights around 20000 km and orbit inclinations of 55°(GPS) and 65°(GLONASS). NNSS has satellites in nearly polar and nearly circular orbits in heights around 1100 km.

We discuss the concept of "mean ionospheric height" and a latitude dependence for this quantity using the NNSS geometry but remark that GPS/GLONASS data reduction too needs this concept.

2. Slant and vertical electron content

The NNSS satellites transmit two carrier signals phase coherently (transmitted frequencies $f_1 = p\,f_r$, $f_2 = q\,f_r$, f_r: "reference frequency", $p = 3$ and $q = 8$ are integer numbers; nominally $f_r = 50$ MHz).

The observed quantity is the carrier phase difference $\Phi = \phi_1/p - \phi_2/q$ (in a sloppy terminology it is usually called "Differential Doppler"). In a (sufficiently

[1]Institut für Meteorologie und Geophysik, Universität Graz, Halbärthgasse 1, A–8010 Graz, Austria, e-mail: leitinger@bkfug.kfunigraz.ac.at

[2]IROE Firenze

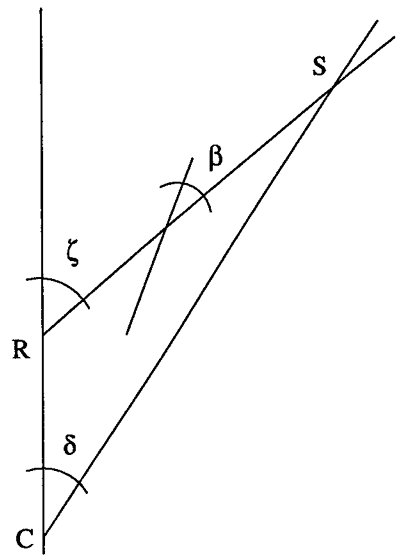

Fig. 1. Ray geometry. R: receiver at ground, S: satellite transmitter, C: center of Earth, ζ: zenith angle of ray at ground, β: zenith angle along ray, δ: angular distance SR at C

accurate) first order approximation it relates to "slant electron content" $I_/$ (the number of free electrons in a tube along the ray path with a cross section of 1 m^2) in the following way:

$$\Phi + \Phi_o = \frac{2\pi f}{c} \int\limits_{\mathrm{S}}^{\mathrm{R}} N_e \, \mathrm{d}\, s = \frac{2\pi f}{c} I_/$$

(N_e: electron density; d s: straight line element; integration from the satellite transmitting antenna at S to the receiving antenna at R. The "initial phase value" Φ_o is an additive constant which has to be found by means of "evaluation procedures" (see, e.g., Leitinger et al. 1975, Leitinger and Putz 1978, Leitinger et al. 1984).

The projection from slant to vertical gives "vertical electron content" (TEC) and therefore is a crucial process which enhances strongly the usefulness of the observations. The geometry for the projection is shown in Fig. 1: S, R and the center of the Earth, C, are in one plane. In this plane we adopt for coordinates the height h and the angle at C, δ. Be β the zenith angle along the ray path, ζ the zenith angle of the ray at R. From the triangle RCS we gain $\beta = \zeta - \delta$. Furthermore we have $\mathrm{d}\, s = -\mathrm{d}\, h / \cos\beta$.

Then we have the relation between slant and vertical electron content, $I_\perp$ as follows:

$$I_/ = \int\limits_S^R N_e \, \mathrm{d}\, s = \int\limits_0^{h_s} \frac{N_e}{\cos\beta} \mathrm{d}\, h = \overline{\frac{1}{\cos\beta}} \int\limits_0^{h_s} N_e \, \mathrm{d}\, h = \overline{\frac{1}{\cos\beta}}\, I_\perp = \frac{1}{\cos\chi}\, I_\perp$$

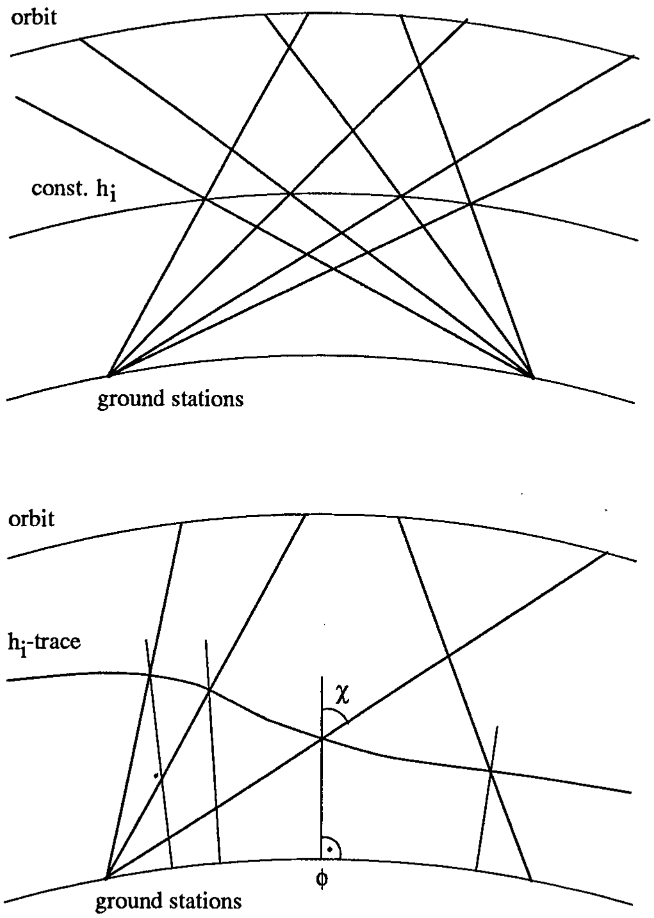

Fig. 2. Sample rays from two ground stations. Top: constant mean ionospheric height h_i. Bottom: mean ionospheric height varies with the horizontal coordinate ϕ (latitude). χ: zenith angle of ray in h_i. In both cases co-planarity is an approximation (projection onto meridian plane in case of NNSS)

($\overline{}$ means averaging in such a way that the equation is exactly fulfilled; χ is the zenith angle in the "mean ionospheric height" h_i (Fig. 2)). From the exact value of the projection factor

$$\frac{1}{\cos\chi} = \frac{\int\limits_S^R N_e \,\mathrm{d}\,s}{\int\limits_0^{h_s} N_e \,\mathrm{d}\,h} = \frac{\int\limits_0^{h_s} N_e \,\mathrm{d}\,h / \cos\beta}{\int\limits_0^{h_s} N_e \,\mathrm{d}\,h}$$

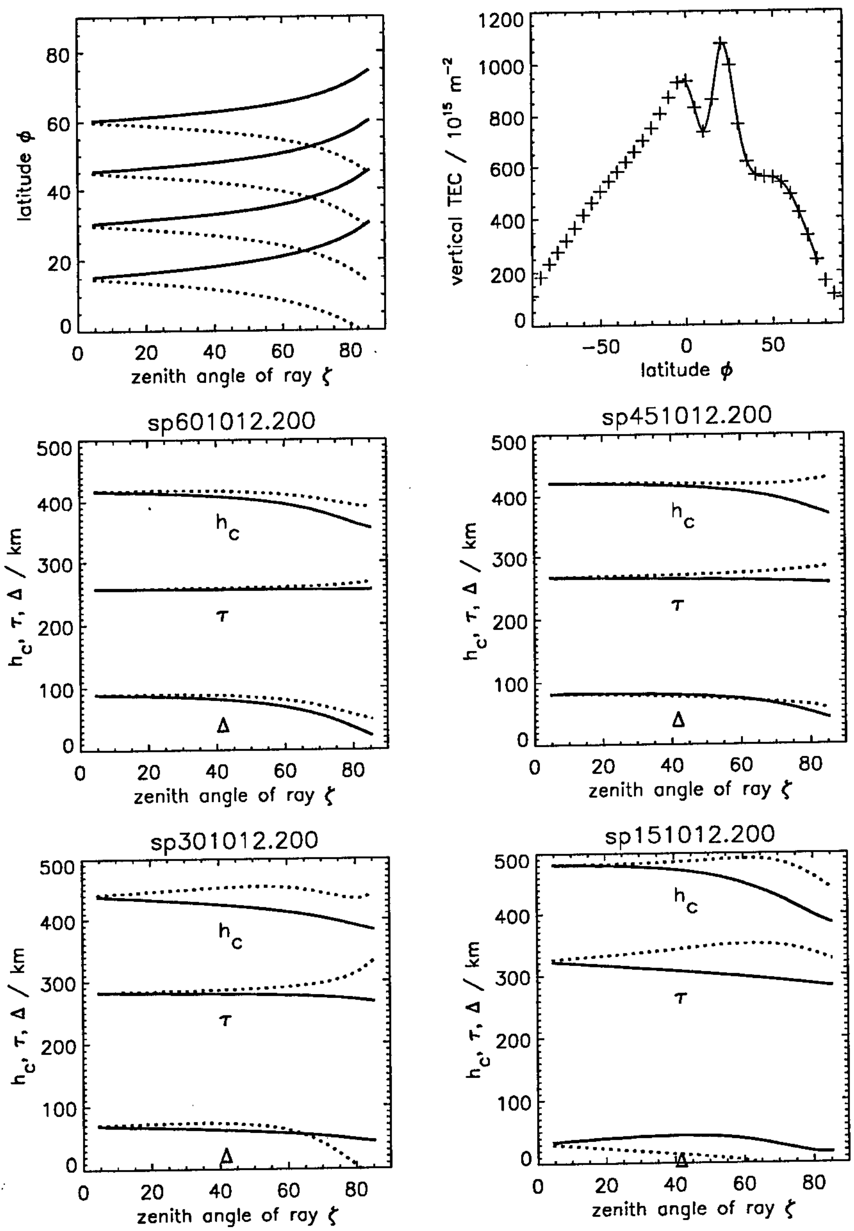

Fig. 3. Model NeUoG, center of mass h_c for the electron distribution along the rays, equivalent slab thickness τ, and $\Delta = h_c - h_m$ for 15° E, October, 12 UT, high solar activity ($S_F = 200$). Ground points R at 60°N, 45°N, 30°N, 15°N. Panel 1 (top left): geogr. latitude vs. zenith angle ζ. Solid lines: North pointing rays, dotted: South pointing rays. Panel 2 (top right): vertical TEC from NeUoG vs. geogr. latitude (crosses). Solid line: third order interpolation in region covered by the model rays. Panels 3 to 6: h_c, τ, Δ vs. ζ for rays originating at 60°N, 45°N, 30°N, 15°N. Solid lines for North looking rays, dotted lines for South looking rays

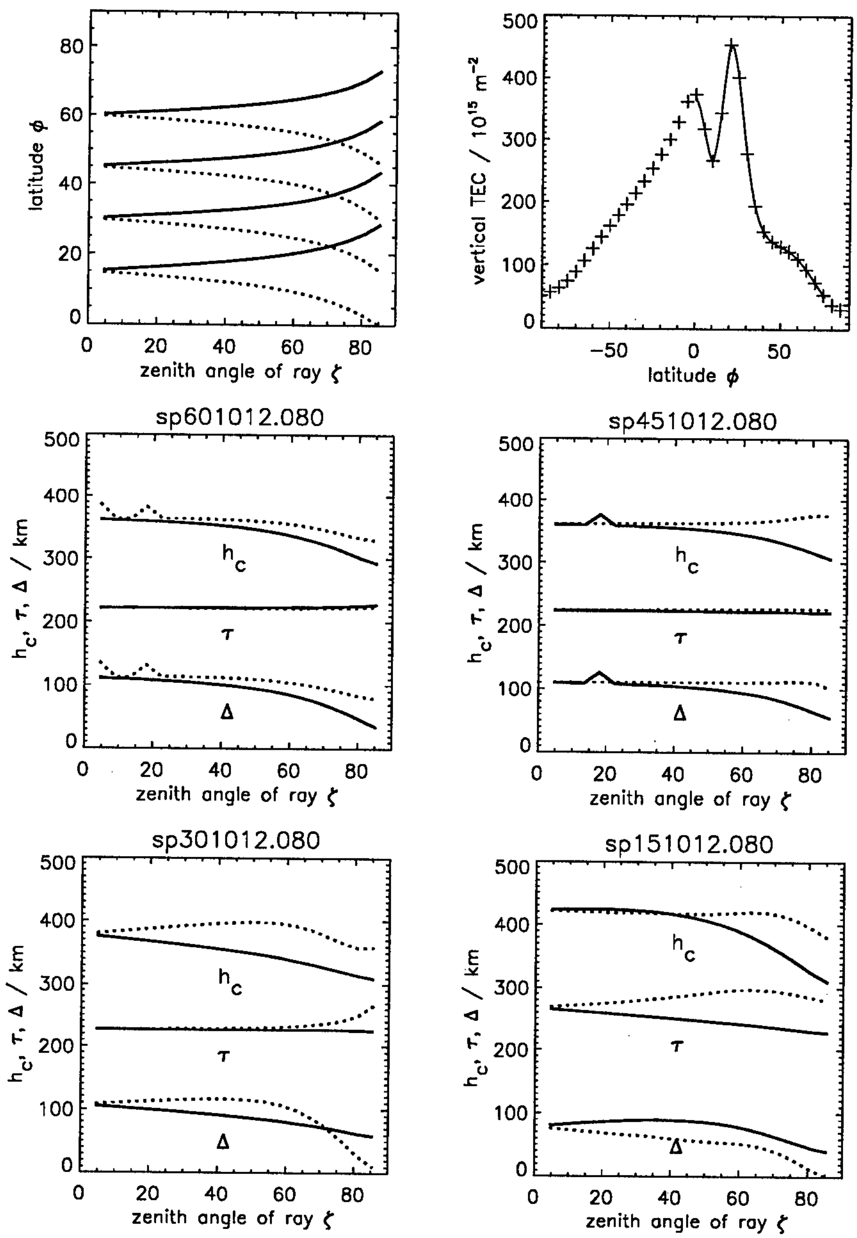

Fig. 4. Model NeUoG, center of mass h_c for the electron distribution, equivalent slab thickness τ, and $\Delta = h_c - h_m$ for 15° E, October, 12 UT, low solar activity ($S_F = 80$). Ground points R at 60°N, 45°N, 30°N, 15°N. Panel 1 (top left): geogr. latitude vs. zenith angle ζ. Solid lines: North pointing rays, dotted: South pointing rays. Panel 2 (top right): vertical TEC from NeUoG vs. geogr. latitude (crosses). Solid line: Third order interpolation in region covered by the model rays. Panels 3 to 6: h_c, τ, Δ vs. ζ for rays originating at 60°N, 45°N, 30°N, 15°N. Solid lines for North looking rays, dotted lines for South looking rays

follows the exact value of the mean ionospheric height

$$h_i = R_e \left[\frac{\sin \zeta}{\sqrt{1 - \cos^2 \chi} - 1} \right] .$$

Since both the height profile of electron density $\int_0^{h_s} N_e \, \mathrm{d}\, h$ and electron density along the ray SR $\int_S^R N_e \, \mathrm{d}\, s$ are not known we have to use an estimate h_i^* for h_i instead of the true value. By means of model calculations it has been shown that h_i is near the center of mass h_c for the electron distribution along a slant ray path. Let $h_c = h_m + \Delta$. If we exclude strong gradients of peak electron density N_m along the ray (vicinity of the equatorial anomaly, severely disturbed conditions, the high latitude case of very strong E layer ionization), Δ is always > 0.

For mid latitudes $\Delta = 50$ km was considered to be a good value. Recent calculations based on both Chapman layers and more realistic models have shown that Δ depends on the zenith angle of the ray, on the height profile, on horizontal gradients, but also on solar activity, season, local time, on the latitude of the ground station, and (to a much lesser degree) on the longitude of the ground station. For mid latitudes, under undisturbed conditions, and excluding sunrise effects, it is safe to neglect the influence of horizontal gradients. However, even for a purely spherical electron density distribution Δ depends on the zenith angle ζ: it decreases with increasing ζ. For a Chapman layer $N_e = N_m \exp[1 - z - \exp(-z)]$ with $z = (h - h_m)/H_1$ for $h \leq h_m$ and $z = (h - h_m)/H_2$ for $h > h_m$, $H_2/H_1 = 2$, we gained the following "rule of thumb" formulae: $\Delta = 0.4\tau$ for $\zeta = 0°$, $\Delta = 0.36\tau$ for $\zeta = 63°$ and $\Delta = 0.3\tau$ for $\zeta = 90°$ (τ: equivalent slab thickness; $\tau = H_1 + (e-1)H_2$).

Simulations based on the model ionosphere NeUoG (Leitinger et al. 1996, 1998) have shown that stronger gradients can lead to an increase of Δ with ζ or to a decrease or even to negative Δ values for high zenith angles ζ in the vicinity of the equatorial anomaly (Tables I and II, Figs 3 and 4).

However, under strong gradient conditions (e.g., in the vicinity of the equatorial anomaly) and for high zenith angles $h_i = h_c$ might not be the best possible choice. If peak electron density increases strongly along the ray $h_i < h_c$ is a better choice and $\Delta = 50$ km is a good compromise (see the next section).

3. Variable mean ionospheric height

For routine evaluation of large quantities of data a variable h_i^* is not practical and not necessary. Such data are used for long term investigations (e.g., for TEC mapping) and experience has shown that the "calibration methods" which have to be applied to find the phase constant Φ_o introduce larger errors than a wrong choice for h_i^*. Furthermore, the natural variability of electron content is very large and for long term investigations both relative "calibration" and "slant to vertical conversion" errors in the order of 10% are easily tolerable.

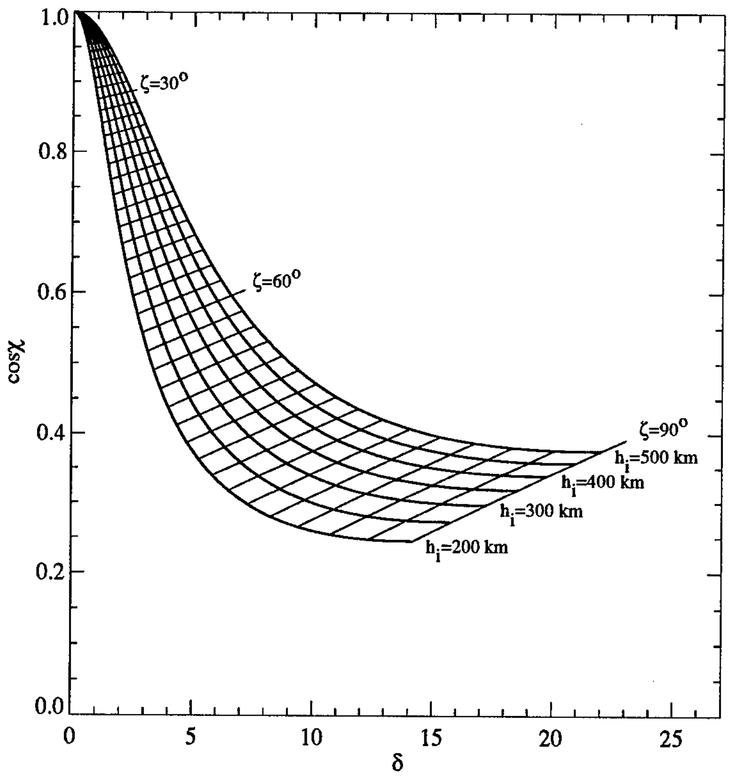

Fig. 5. Heavy lines: projection factor $\cos\chi$ vs. angular distance from ground station δ for different mean ionospheric heights h_i. Thin lines: points with given zenith angle of the rays at the ground station ζ (spacing: 2 degrees)

For individual studies the situation is different. For such it makes sense to adjust the mean ionospheric height to the actual situation. When the latitudinal profiles of vertical TEC gained from Diff. Doppler observations from a chain of stations span a large latitude range, a constant mean ionospheric height is not always good enough. Therefore, we have introduced the possibility to use a latitude dependent h_i^*.

In general this approach needs a model for the latitude dependence of h_m except when the latitude dependence of h_m can be gained from measurements. (Data sources: Incoherent Scatter, Ionosonde parameters, true height analysis of bottom or topside ionograms; in the near future inversion of GNSS occultation data.)

A change of h_i changes the latitude profile of TEC in two ways: a) by changing the projection factors, b) by shifting the "ionospheric points" P which are the intersection points of the straight lines SR with the h_i shell. For a given ray path an increase of h_i decreases χ (and therefore increases vertical content) and shifts P away from R (compare Fig. 5).

The ionospheric points P are found by means of an iterative algorithm. Mean

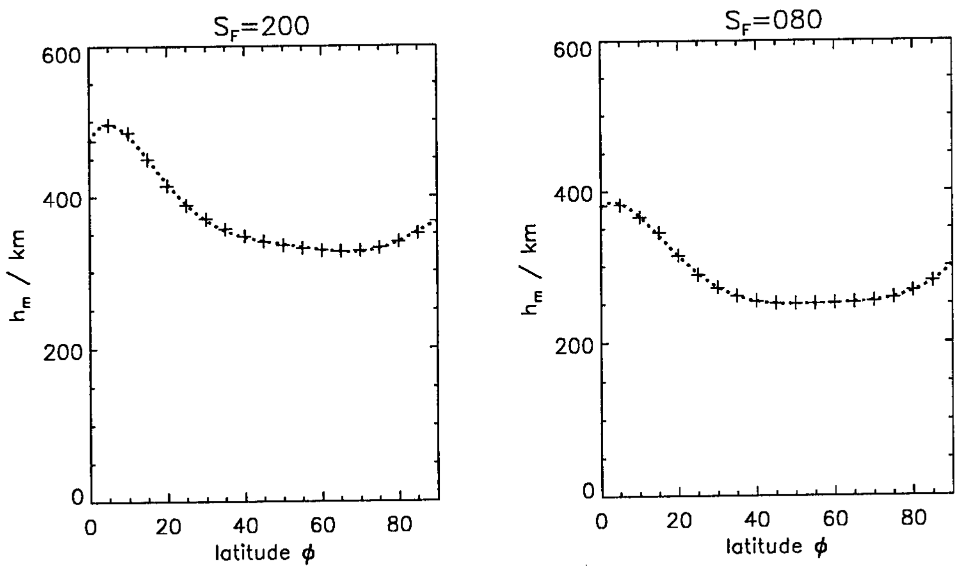

Fig. 6. Model NeUoG, F layer peak height h_m vs. latitude for 15° E, October, 12 UT. Left hand side: high solar activity ($S_F = 200$), right hand side: low solar activity ($S_F = 80$). Crosses: model values; dotted: polynomial fit (6th order)

ionospheric height h_i is formulated as a function of δ (Fig. 1). For a given ray (with zenith angle ζ at R) we start at a height h and step forward by increasing h until $h > h_i$. This process is repeated with a smaller step size until $|h - h_i| < \varepsilon$, ε being a preselected accuracy limit.

For NNSS it is of advantage to refer to a geographic meridian which can be found by a suitable fit to the 400 km ionospheric points. Then h_i is taken as a function of geographic latitude, e.g., as a short polynomial.

We have used the model ionosphere NeUoG for simulations. Sample results are shown in Figs 6 and 7. First, peak height h_m was calculated from NeUoG for fixed time and longitude and for a grid of latitudes with a spacing of 5°(19 values for latitudes 0° to 90°).

We have used NeUoG to check for other Δ values and found that $\Delta = 100$ km was definitely too large even under conditions of $h_c - h_m > 100$ km. On the other hand, $\Delta = 0$ was found not to be a good constant value even for equatorial receiving stations.

A polynomial of degree 6 was fitted to the grid point values in one hemisphere by means of a least squares procedure (samples for low and high solar activity are shown in Fig. 6). $h_i = h_m + \Delta$ was used for the mean ionospheric height. For the scenarios investigated so far a constant $\Delta = 50$ km was found to be a good compromise. For high solar activity, day time (noon, afternoon) and high zenith angles ζ it is too large in the vicinity of the crest of the equatorial anomaly (Fig. 7, top left). A decrease of Δ with ζ from about $\Delta = 50$ km to $\Delta = 10$ km would give optimal results.

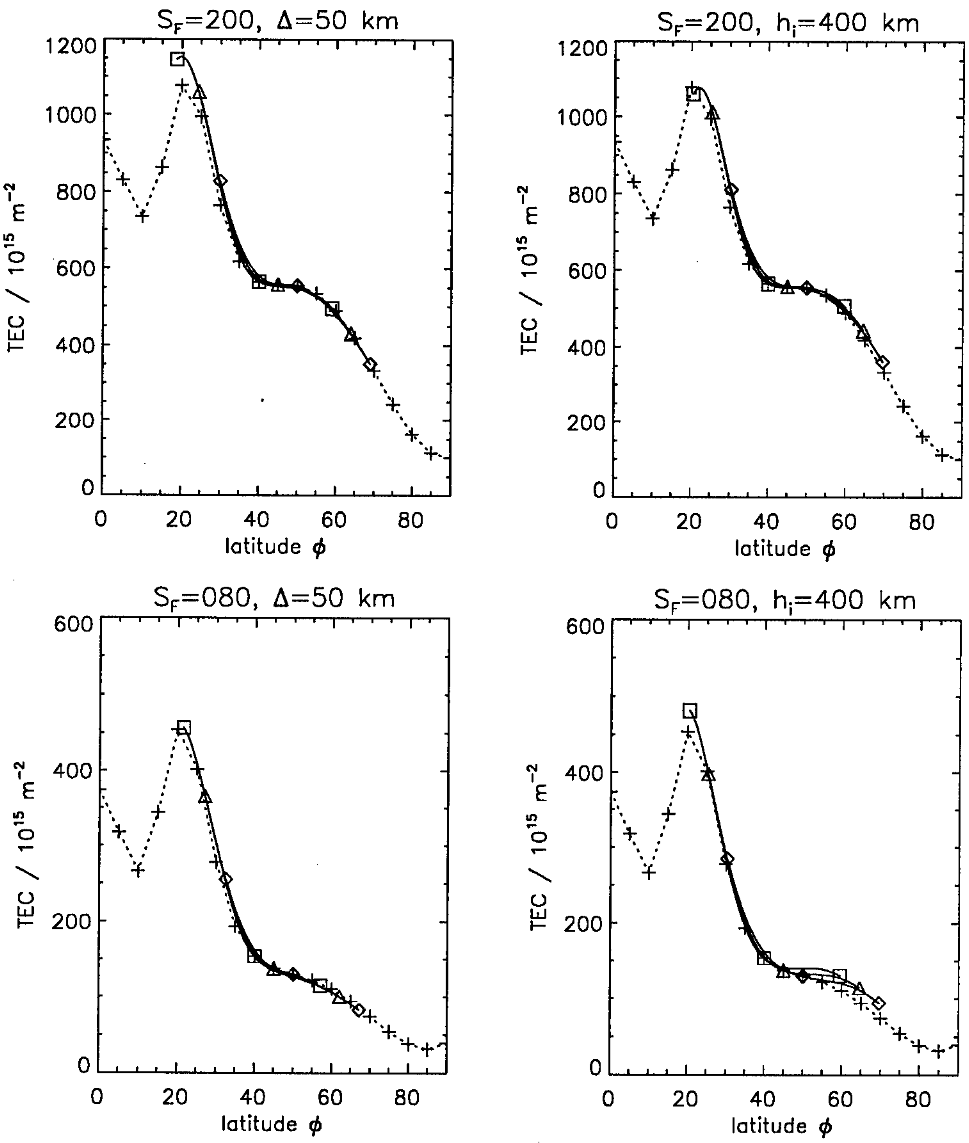

Fig. 7. Model NeUoG, vertical electron content (TEC) in units of 10^{15} m^{-2}. vs. latitude for 15° E, October, 12 UT. At the top: high solar activity ($S_F = 200$), at the bottom: low solar activity ($S_F = 80$). Crosses: given values (dots: linear interpolation); projection results: the symbols mark the end points (zenith angle $\zeta = \pm 90°$) and the mid points ($\zeta = 0°$). Squares for "receiving station" R at $\phi = 40°$N, triangles for R at $\phi = 45°$N, diamonds for R at $\phi = 50°$N. Left hand side: $h_i = h_m + \Delta$ with $\Delta = 50$ km, right hand side: $h_i = 400$ km. Heavy lines: projection factor $\cos\chi$ vs. angular distance from ground station δ for different mean ionospheric heights h_i. Thin lines: points with given zenith angle of the rays at the ground station ζ (spacing: 2 degrees)

Table Ia. Model ionosphere NeUoG, rays from 45°N, 15°E, October, 12 UT, $S_F = 200$

	North looking rays						South looking rays					
ζ	Δ	Δ/τ	N_m	τ	h_m	h_c	Δ	Δ/τ	N_m	τ	h_m	h_c
°	km		km	km	km	km	km		km	km	km	km
9	81.8	0.306	2.090	266.7	339.5	421.3	81.0	0.302	2.081	267.9	340.8	421.8
18	81.7	0.307	2.094	266.2	338.8	420.6	80.3	0.299	2.077	268.5	341.6	421.9
27	81.5	0.307	2.098	265.6	338.1	419.6	79.3	0.294	2.072	269.2	342.4	421.7
36	80.7	0.305	2.102	264.9	337.3	418.0	77.8	0.288	2.069	270.0	343.4	421.2
45	79.2	0.300	2.107	264.1	336.4	415.5	75.9	0.280	2.067	271.0	344.7	420.5
54	75.9	0.288	2.110	263.2	335.3	411.2	73.3	0.269	2.071	272.3	346.4	419.7
63	71.4	0.272	2.107	262.1	333.8	405.2	69.9	0.255	2.090	274.0	349.2	419.1
72	62.7	0.241	2.087	260.5	331.9	394.5	66.3	0.239	2.166	276.7	354.1	420.4
81	49.1	0.190	2.004	258.5	329.2	378.3	61.3	0.218	2.504	280.6	365.0	426.2

Table Ib. Model ionosphere NeUoG, rays from 30°N, 15°E, October, 12 UT, $S_F = 200$

	North looking rays						South looking rays					
ζ	Δ	Δ/τ	N_m	τ	h_m	h_c	Δ	Δ/τ	N_m	τ	h_m	h_c
°	km		km	km	km	km	km		km	km	km	km
9	68.1	0.242	2.639	281.7	368.5	436.7	70.5	0.249	2.801	282.9	372.3	442.8
18	66.8	0.238	2.570	281.1	366.7	433.5	71.4	0.252	2.899	283.6	374.4	445.8
27	65.2	0.233	2.499	280.5	364.8	430.1	72.0	0.253	3.009	284.3	376.8	448.7
36	63.5	0.227	2.424	279.9	362.7	426.3	71.8	0.252	3.135	285.2	379.7	451.5
45	61.6	0.221	2.342	279.2	360.4	422.0	70.2	0.245	3.280	286.5	383.5	453.8
54	59.2	0.213	2.252	278.2	357.6	416.8	65.6	0.227	3.445	288.4	388.8	454.4
63	56.2	0.203	2.166	276.6	354.1	410.2	54.5	0.187	3.584	292.0	396.8	451.3
72	51.7	0.189	2.094	274.2	349.5	401.2	32.1	0.108	3.619	298.3	410.1	442.1
81	45.6	0.169	2.069	270.0	343.4	389.0	-3.9	-0.012	2.993	314.7	437.9	433.9

Table Ic. Model ionosphere NeUoG, rays from 15°N, 15°E, October, 12 UT, $S_F = 200$

	North looking rays						South looking rays					
ζ	Δ	Δ/τ	N_m	τ	h_m	h_c	Δ	Δ/τ	N_m	τ	h_m	h_c
°	km		km	km	km	km	km		km	km	km	km
9	36.3	0.113	2.794	319.9	445.0	481.3	27.3	0.084	2.567	327.1	454.6	482.0
18	40.2	0.127	2.928	316.3	440.2	480.4	22.6	0.068	2.469	330.6	459.8	482.4
27	43.7	0.140	3.074	312.6	435.0	478.7	17.9	0.053	2.371	334.6	465.3	483.2
36	46.2	0.150	3.233	308.9	429.2	475.4	13.3	0.039	2.272	339.1	471.5	484.8
45	47.3	0.155	3.407	304.8	422.5	469.8	8.7	0.025	2.176	344.1	478.5	487.1
54	45.7	0.152	3.583	300.5	414.6	460.3	4.0	0.012	2.113	348.9	486.1	490.2
63	39.5	0.133	3.632	296.1	405.5	445.0	-1.5	-0.004	2.174	350.8	493.0	491.5
72	28.5	0.098	3.547	290.7	394.0	422.6	-12.0	-0.035	2.385	347.1	495.8	483.8
81	16.7	0.059	3.092	284.9	378.7	395.4	-21.3	-0.064	2.741	334.6	480.1	458.7

Table IIa. Model ionosphere NeUoG, rays from 45°N, 15°E, October, 12 UT, $S_F = 80$

	North looking rays						South looking rays					
ζ	Δ	Δ/τ	N_m	τ	h_m	h_c	Δ	Δ/τ	N_m	τ	h_m	h_c
°	km		km	km	km	km	km		km	km	km	km
9	109.1	0.488	0.609	223.7	250.7	359.8	110.1	0.491	0.616	224.4	251.0	361.0
18	125.5	0.561	0.605	223.5	250.6	376.1	110.3	0.491	0.621	224.4	251.1	361.4
27	107.0	0.479	0.601	223.6	250.5	357.5	110.4	0.491	0.626	224.9	251.4	361.8
36	105.3	0.471	0.597	223.4	250.4	355.7	110.4	0.490	0.633	225.3	251.7	362.1
45	102.6	0.460	0.593	223.1	250.3	353.0	110.4	0.490	0.644	225.5	252.1	362.5
54	98.5	0.442	0.588	222.8	250.3	348.8	110.4	0.489	0.661	225.9	252.9	363.3
63	91.7	0.412	0.581	222.5	250.3	342.0	110.9	0.490	0.692	226.4	254.2	365.1
72	80.7	0.363	0.569	222.1	250.4	331.1	112.3	0.496	0.764	226.5	257.2	369.5
81	64.1	0.289	0.543	221.8	250.7	314.8	111.7	0.494	0.992	226.3	264.7	376.4

Table IIb. Model ionosphere NeUoG, rays from 30°N, 15°E, October, 12 UT, $S_F = 80$

	North looking rays						South looking rays					
ζ	Δ	Δ/τ	N_m	τ	h_m	h_c	Δ	Δ/τ	N_m	τ	h_m	h_c
°	km		km	km	km	km	km		km	km	km	km
9	103.5	0.456	1.179	226.8	270.3	373.8	109.4	0.482	1.280	227.0	273.1	382.5
18	100.2	0.442	1.135	226.6	269.0	369.1	112.1	0.493	1.340	227.3	274.6	386.7
27	96.6	0.426	1.089	226.6	267.6	364.2	114.4	0.503	1.408	227.6	276.5	390.9
36	92.7	0.409	1.040	226.5	266.2	358.8	116.0	0.508	1.487	228.1	278.7	394.7
45	88.2	0.389	0.985	226.4	264.5	352.7	115.8	0.506	1.580	228.8	281.7	397.5
54	82.9	0.366	0.921	226.3	262.6	345.5	111.7	0.486	1.691	229.9	285.9	397.6
63	76.2	0.336	0.844	226.3	260.1	336.3	99.2	0.427	1.806	232.4	292.5	391.7
72	69.1	0.305	0.757	226.6	256.9	326.0	72.4	0.305	1.890	237.3	303.4	375.8
81	60.7	0.269	0.665	226.0	253.0	313.7	32.8	0.132	1.703	249.1	324.9	357.7

Table IIc. Model ionosphere NeUoG, rays from 15°N, 15°E, October, 12 UT, $S_F = 80$

	North looking rays						South looking rays					
ζ	Δ	Δ/τ	N_m	τ	h_m	h_c	Δ	Δ/τ	N_m	τ	h_m	h_c
9	82.2	0.312	1.360	263.4	341.5	423.7	73.3	0.271	1.226	270.5	347.5	420.8
18	86.0	0.331	1.438	259.7	337.9	423.9	69.0	0.252	1.166	274.1	350.2	419.2
27	88.7	0.347	1.523	256.0	334.0	422.7	65.2	0.235	1.105	278.1	353.1	418.3
36	89.8	0.356	1.616	252.3	329.5	419.3	61.6	0.218	1.042	282.6	356.2	417.7
45	88.4	0.356	1.718	248.4	324.1	412.5	56.5	0.196	0.976	288.2	359.8	416.3
54	83.3	0.341	1.826	244.3	317.5	400.8	53.2	0.181	0.913	294.4	364.2	417.4
63	72.9	0.303	1.892	240.1	309.4	382.3	48.9	0.164	0.914	297.5	370.8	419.6
72	56.9	0.242	1.869	235.3	299.0	355.9	36.0	0.123	1.019	293.9	379.0	415.0
81	39.3	0.171	1.656	229.6	284.5	323.9	10.9	0.038	1.229	284.8	383.3	394.2

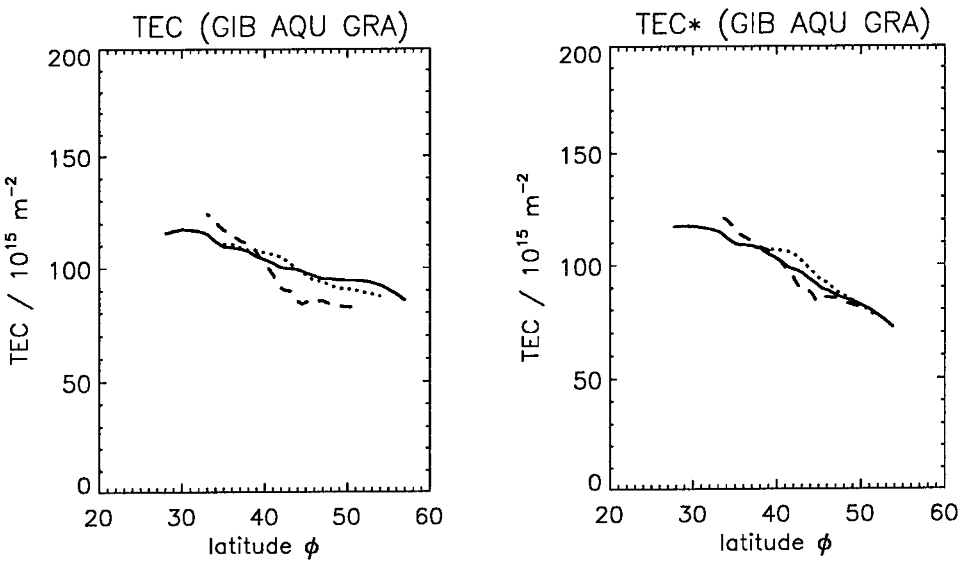

Fig. 8. Example for the evaluation of Differential Doppler observations using a fixed mean ionospheric height of 400 km (left hand side) and a variable h_i (right hand side). Observing stations GIBilmanna (dashed line), L'AQUila (heavy line) and GRAz (dotted line). 25 October, 1995, around 10:18 UT

With NeUoG we have also checked the choice of $h_i = 400$ km and found that this value leads to vertical TEC results which are comparable in quality with the $\Delta = 50$ km results under most conditions of high solar activity for lower mid latitudes and even in the vicinity of the equatorial anomaly (Fig. 7, top right). Under conditions of low solar activity $h_i = h_m + 50$ km clearly gives better results than $h_i = 400$ km, especially in higher mid latitudes (Fig. 7, bottom right). However, for mass evaluation of large amounts of data the complication to introduce a model for h_m is not justified. If needed for individual studies re-projection of TEC data is easy to carry out if the geographic coordinates of the ionospheric points are known.

An example from observed values is shown in Fig. 8. The Diff. Doppler data from the three stations Gibilmanna (38.0°N, 14.0°E), L'Aquila (42.3°N, 13.4°E) and Graz (47.1°N, 15.5°E) were first evaluated with $h_i = 400$ km (two stations method for the combination of Gibilmanna and L'Aquila data — see Leitinger et al. 1975, least squares fit of the data from Graz to the TEC data from L'Aquila). The latitude dependence of vertical electron content shows a considerable divergence (left panel of Fig. 8). A new evaluation was made with $h_m = 250-4.167(\phi-\phi_o)+0.0833(\phi-\phi_o)^2$, $\phi_o = 48°$N, h_m in km. The coefficients were estimated on the basis of model data for h_m and on the basis of GPS-MET occultation results (Leitinger et al. 1997) which gave a rather thin F layer in rather low heights. The vertical TEC data gained with $h_i = 400$ km were re-projected using $h_i(\phi) = h_m(\phi) + 50$ km. The results are shown in the right panel of Fig. 8. The divergence of the three TEC curves is appreciably smaller. The remaining divergence is partly caused by smaller

scale structures in the latitudinal dependence of true vertical TEC, partly by the oversimplification of the $h_i(\phi)$ model.

4. Conclusions

Simulations based on a Chapman model and on the model ionosphere NeUoG as well as an application to observations have shown that a latitude dependent mean ionospheric height is of value for case studies provided that information on the latitude dependence of F layer peak height h_m is available. One possibility to gain $h_m(\phi)$ data is the "educated use" of a model. The ITU-R maps (formerly CCIR maps, CCIR 1967) for the ionogram parameters f_0F2, M3000(F2), f_0E can be used to provide the input values for one of the established "formulae" for h_m. The maps could be updated with observed ionogram parameters using "nowcasting" procedures. Updating of h_m maps constructed from the ITU-R maps with h_m values from the true height analysis of ionograms is an alternative. (Remark: h_m and N_m of NeUoG is based on the ITU-R maps.) For regional applications the use of regional maps is recommended (e.g., the PRIME/COST 238 maps for Western Europe, Bradley, 1995). For most purposes $h_i(\phi) = h_m(\phi) + \Delta$ is an adequate approach. A constant Δ of 50 km gave good results.

On the basis of recent simulations the "old" recommendation $h_i = h_m + 50$ km is maintained but our results show that for high zenith angles ζ this value for the mean ionospheric height can differ by up to ± 70 km from the height of the center of gravity h_i of the electron density distribution along the rays.

A fixed h_i of 400 km is appropriate for routine evaluation of NNSS observations.

References

Bradley P A ed. 1995: PRIME (Prediction and Retrospective Ionospheric Modelling over Europe). Final Report COST 238, Comm. European Communities, Brussels

CCIR 1967: Atlas of ionospheric characteristics. Comité Consultatif International des Radiotelecommunications, Report 340–4, International Telecommunications Union (ITU), Geneva

Leitinger R, Kirchengast G 1998: Easy to use global and regional ionospheric models – A report on approaches used in Graz. *Acta Geod. Geoph. Hung.*, 32, 329–342.

Leitinger R, Putz E 1978: Die Auswertung von Differenz-Doppler-Messungen an den Signalen von Navigationssatelliten. Techn. Report, IMG, University of Graz

Leitinger R, Schmidt G, Tauriainen A 1975: *J. Geophysics (Zs. Geophysik)*, 41, 201–213.

Leitinger R, Hartmann G K, Lohmar F-J, Putz E 1984: *Radio Sci.*, 19, 789–897.

Leitinger R, Titheridge J E, Kirchengast G, Rothleitner W 1996: *Kleinheubacher Ber.*, 39, 697–704.

Leitinger R, Ladreiter H-P, Kirchengast G 1997: *Radio Sci.*, 32, 1657–1669.

Acta Geod. Geoph. Hung., Vol. 33(1), pp. 75–81 (1998)

SOME RESULTS ON GPS-NNSS TEC COMPARISON

L CIRAOLO[1] and P SPALLA[1]

Availability of three years of TEC versus latitude, obtained from NNSS differential doppler measurements, enables to give a contribution to the study of TEC of the upper part of the ionosphere.

Keywords: GPS; GPS-NNS TEC differences; NNSS; plasmaspheric content

1. Basic considerations on GPS and NNSS data analysis

— *For both GPS and NNSS:* Equation of observation: $d = k \cdot \mathrm{TEC} + \beta$.

Observed Differential Phase and/or Group Delays, d; total electron content, TEC; bias or offset, β.

Extra problems for phase: inherent ambiguity, cycle slips.

— *Model:* Vertical total electron content (VEC): $\mathrm{TEC}(P{-}S) = \mathrm{VEC}(P_{\mathrm{iono}}) \sec\chi$.

Ionosphere: slab of infinitesimal width at 400 km height.

Solution of $d = \mathrm{VEC} \cdot \sec\chi + \beta$ enables estimation of VEC.

— *NNSS analysis:* One station: assuming VEC quasi-linear function of P_{iono}, Φ.

$\mathrm{VEC}(\Phi) = (d - \beta)\cos\chi$, $\Delta\mathrm{VEC} = \Delta(d\cos\chi) - \beta\Delta(\cos\chi)$.

LSQ solution for intercept ΔVEC and slope β.

Two stations: assuming that observations relative to the same ionospheric point have the same VEC (neglecting the longitude displacement)

$$(d(t_1) - \beta_1)\cos\chi_1 = (d(t_2) - \beta_2)\cos\chi_2$$

LSQ solution for β_1 and β_2.

Final product: VEC at every degree of latitude along the track of P_{iono}.

— *GPS analysis:* Assumptions for VEC over the station: a) dependence on time and longitude only through the Local Time; b) linear dependence on latitude.

Given a time t_s at the station, observations from satellite i and j at the same LT are paired in order to give the same VEC, giving the equations of condition:

$$[d(t_i) - \beta_i]\cos\chi_i - m(t_s) \cdot (\Phi_i - \Phi_s) = [d(t_j) - \beta_j]\cos\chi_j - m(t_s) \cdot (\Phi_j - \Phi_s)\,.$$

LSQ solution for biases β's and latitude slopes $m(t_s)$ smoothed over 20 minutes.

Final product: VEC and latitude slope daily curves at each 10th minute, satellite plus receiver biases (group) or phase offsets (phase).

[1]Istituto di Ricerca sulle Onde Elettromagnetiche "Nello Carrara", Firenze, Italy

1217-8977/98/$ 5.00 ©1998 Akadémiai Kiadó, Budapest

2. The comparison method

NNSS provides TEC evaluations and their accurate latitudinal dependence sparse in time; GPS provides continuous TEC evaluations.

The comparison proceeds as follows, as described in Fig. 1:

— the NNSS TEC value at the latitude of the GPS station (Matera) is interpolated from the latitudinal curve,

— this NNSS TEC value is tagged with the epoch of the closest approach, instead of with the actual time of crossing the parallel of the GPS station,

— these NNSS TEC values are plotted on the GPS TEC daily curves displaced in time according to the difference in longitude between the ionospheric point of the NNSS measurement and that of the GPS station. This accounts for the local time dependence of the ionosphere, in accordance with the above assumptions.

A typical example for a given day is shown in Fig. 2, in which the continuous line is the GPS TEC daily curve and the single points are NNSS TEC's. The results of about 3 years of daily curves of GPS TEC and about 42000 NNSS TEC passes (from only one station during 1994 and mainly from two stations during 1995 and 1996) are available and can be compared. This analysis follows a similar one carried out on two years (1994–95) observations and constitutes its improvement (Ciraolo and Spalla 1997).

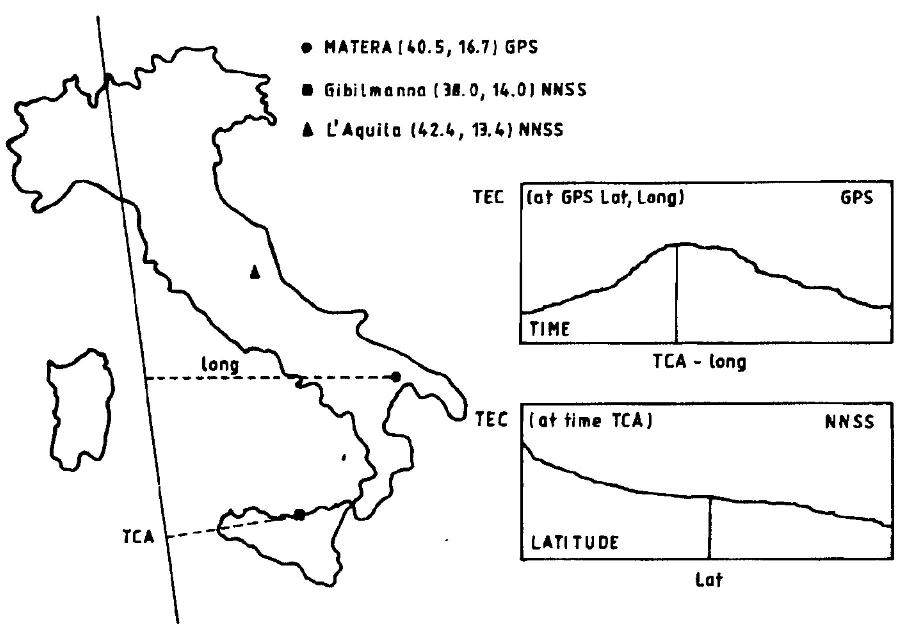

Fig. 1. The geometry of GPS and NNSS observations

If actual slant TEC's in the same direction were compared, the GPS TEC will always be larger than NNSS TEC, and the difference accounts for the electron content between the two satellites. It can be expected that for vertical TEC's evaluated as described in the previous sections, the following equation holds: $\mathrm{VEC_{GPS}} = \mathrm{VEC_{NNSS}} + P$, where all the quantities involved are positive: no particular physical meaning is given in this moment to the differences P.

3. Results of the comparison for GPS-NNSS differences

As can observed in Fig. 2, there are some NNSS points showing a TEC larger than the one provided by GPS, which is non physical. These events must be considered only as being derived from bad solutions whether in GPS or NNSS TEC or in both.

The statistics of the differences, P between TEC evaluated from GPS and that evaluated from NNSS, computed individually over the data of each year, have confirmed the absence of daily or seasonal trends as the previous analysis. The results of present analysis are summarized in Table I.

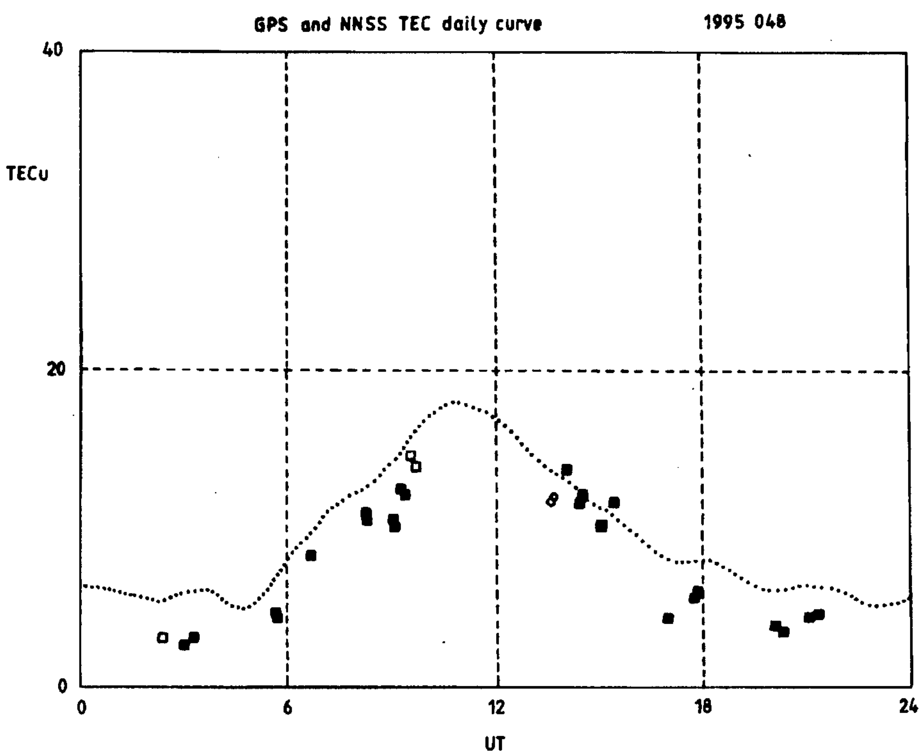

Fig. 2. Daily curve of measured TECs: the dotted line is the GPS TEC, the filled points are the NNSS measurements derived from the two stations solutions, the empty ones are TEC from one station solution

Table I. The results of the statistical study

1994	All data		Set 3		Set 2		Set 1	
Processed data	13620		11458		10158		6811	
Negat. values	2095	15%	902	8%	291	3%	0	
Average	2.31		2.62		2.60		2.58	
Stand. deviat.	4.33		1.76		1.37		0.77	
Correlat. coef.	0.74		0.94		0.96		0.99	
Slope	0.95		0.96		0.97		0.99	
Error of slope	0.0074		0.0034		0.0028		0.0020	
Intercept	−1.80		−2.25		−2.32		−2.43	
Error of interc.	4.32		1.75		1.36		0.76	
Median 2.59			lower quartile 1.11				upper quartile 4.02	
1995	**All data**		**Set 3**		**Set 2**		**Set 1**	
Processed data	17473		15124		13230		8738	
Negat. values	2753	16%	1305	9%	446	3%	0	
Average	1.91		2.37		2.36		2.35	
Stand. deviat.	3.84		1.62		1.24		0.72	
Correlat. coef.	0.75		0.93		0.96		0.99	
Slope	1.01		1.00		0.99		0.99	
Error of slope	0.0068		0.0031		0.0025		0.0018	
Intercept	−2.05		−2.35		−2.25		−2.30	
Error of interc.	3.84		1.62		1.24		0.72	
Median 2.38			lower quartile 0.97				upper quartile 3.58	
1996	**All data**		**Set 3**		**Set 2**		**Set 1**	
Processed data	12000		9456		8360		6001	
Negat. values	4004	33%	2319	24%	1816	22%	1005	17%
Average	−2.68		1.21		1.35		1.32	
Stand. deviat.	18.22		2.77		2.01		1.22	
Correlat. coef.	0.12		0.74		0.84		0.94	
Slope	0.63		0.97		1.02		1.04	
Error of slope	0.0465		0.0091		0.0071		0.0051	
Intercept	5.55		−0.99		−1.49		−1.62	
Error of interc.	18.17		2.77		2.01		1.19	
Median 1.49			lower quartile 1.63				upper quartile 3.11	

The first step of the analysis was the evaluation of medians and quartiles. We define four sets of data: one contains all data, one (named 1 in all the tables) the data falling in the interquartile range, the others (2 and 3) contain the data falling respectively in the double and the triple of the interquartile.

The following quantities have been evaluated for all these sets: the total number of cases, the negative values and their relative frequencies, the averages, the standard deviations. Medians and quartiles are also reported.

The negative values of P contained in all the sets are almost the same in 1994

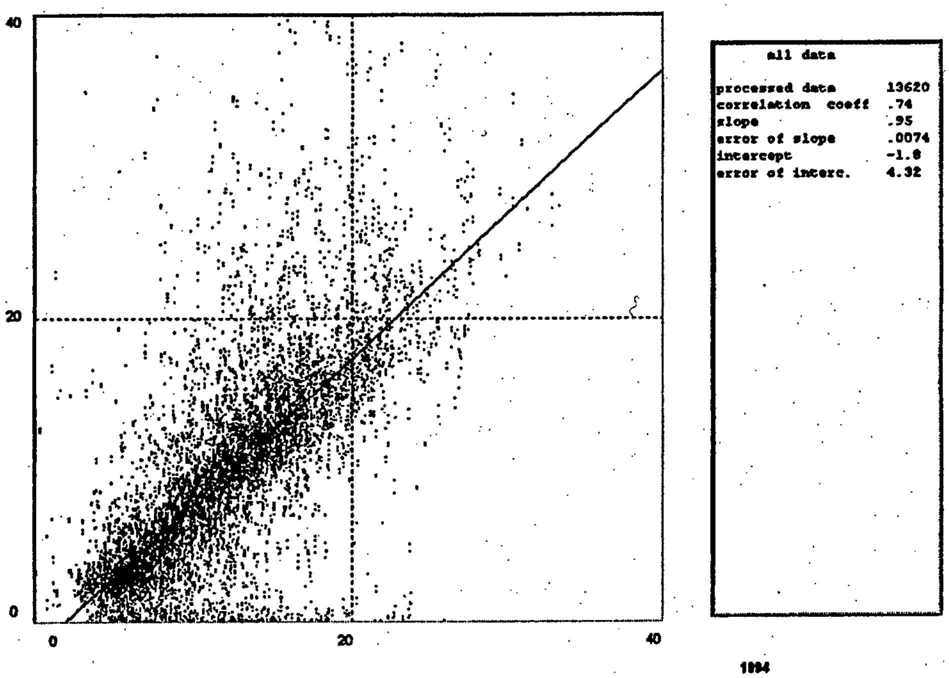

Fig. 3. A correlation curve of one year of data (1994)

and 1995, while in 1996 increase significatively. This seems to be correlated with the decrease of the medians during the three analysed years (accounting for the minimum of the solar cycle?). This is a disagreement with the current models; further observations during the increasing solar cycle are any way needed to reach conclusive results. The last analysis carried out was a direct comparison between the two sets of TEC. The above assumption — expressed by $\mathrm{VEC}_{GPS} = \mathrm{VEC}_{NNSS} + P$ —, seems to be confirmed by the analysis, so that it can be expected that, by plotting the NNSS TEC versus the corresponding GPS TEC, the resulting distribution can be described by a straight line of unitary slope and negative intercept. Several linear regressions were applied to the above-defined sets of data (Fig. 3).

The results are reported in Table I too. Given that, by taking the values between the quartiles, the number of points is half of the total, case 2 and 3 contain about 90% of the points in 1994 and 1995, 80% in 1996: i.e. it was sufficient to reduce the range of the data only slightly in order to exclude most of the outliers. All the resulting slopes amount practically to 1. The correlation coefficient, which is rather poor for all data, converges rapidly towards 1 in the other cases. The intercept behaves in a similar way, converging to a value decreasing versus the year as for the median.

4. Results of the comparison for GPS-NNSS latitudinal dependence (slope)

As reported above, NNSS data analysis provides actually VEC as function of latitude. GPS analysis provides the coefficient of the (assumed) linear dependence of VEC on latitude, $m(t)$: this slope has to be considered as an average slope over the horizon of the observing GPS station. In order to make a comparison between the two techniques, an average NNSS slope has been evaluated still over the horizon of the NNSS station, and this slope was compared with the GPS one at the same epoch.

Using the huge amount of available data, statistically significative season subsets have been obtained. As for VEC, two different types of analysis have been carried out for each seasonal subset. The linear regression of NNSS vs. GPS slopes didn't give evidence of correlation: this is probably due to the errors intrinsic in the GPS analysis which assumes a linear latitude dependence overall the station horizon. We plan to improve the analysis using more sophisticated models of lati-

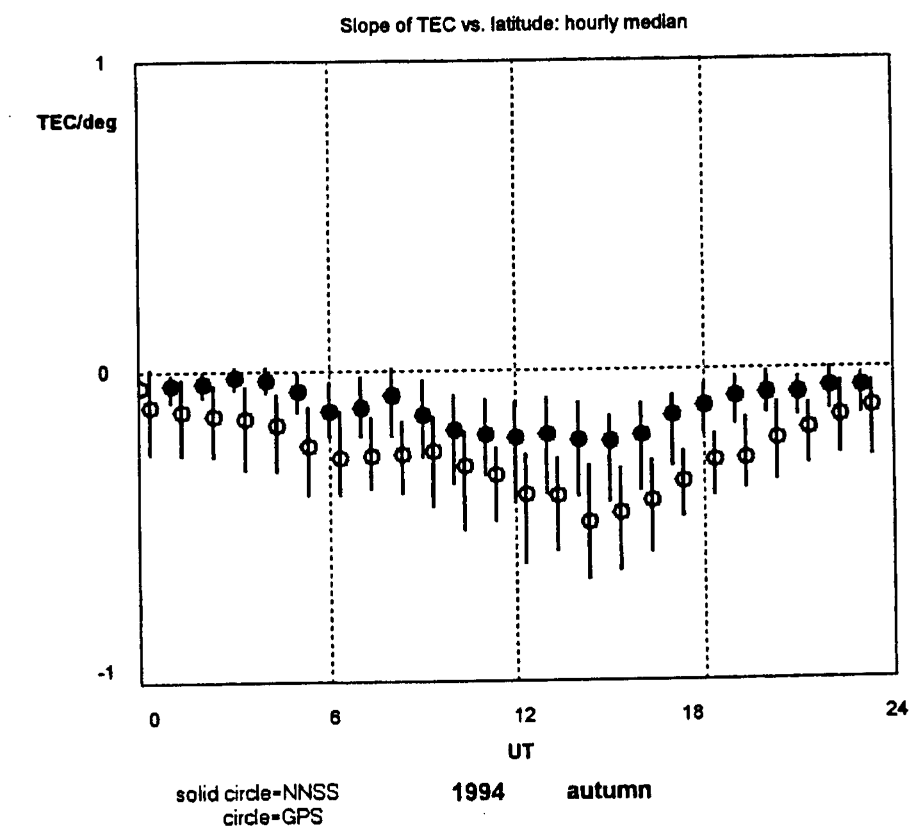

Fig. 4. An example of a daily curve of median slopes (autumn)

tudinal dependence, as for example the regional model of COST 238, and/or global models as IRI.

On the other hand, the direct examination of GPS and NNSS median slopes (see Fig. 4 as an example, where circles are the medians and bars represents the interquartile ranges) plotted versus time of the day shows rather clearly for both sets a similar diurnal behaviour dependent on season. These results, contrary to regression ones, push to refine the investigation, whose first approach will be a spectral analysis.

5. Conclusions

The results presented above shed light on two important points: the comparison between two different techniques of TEC evaluation, and a contribution to the knowledge of the TEC between 1100 and 20000 km, which is currently a relatively unknown field. It must be kept in mind that the present analysis refers to a middle-latitude situation.

We cannot state that this analysis, at least at this stage, can provide an effective tool to sound the plasmaspheric content, mainly as comparisons are made among measurements taken over very different ray paths, and the accuracy of GPS TEC evaluations is of the same order of the plasmaspheric content itself. These considerations make it unlikely that these results derive from systematic errors; it rather suggests that some physical quantity is being measured, and that refining the methods of analysis (i.e. limiting only to close GPS and NNSS ray paths), some contribution to the knowledge of electron content between 1100 and 20000 km could be given.

References

Ciraolo L, Spalla P 1997: *Radio Sci.*, 32, 1071–1080.

Acta Geod. Geoph. Hung., Vol. 33(1), pp. 83–90 (1998)

AN INVESTIGATION OF THE IONOSPHERE IN THE SOUTHERN HIGH LATITUDES DURING LOW SUNSPOT NUMBERS

B S TATE[1], N M SHILO[1], E A ESSEX[1]

During the period of 1993–1996, the transmissions from the US Navy Navigational Satellite System (NNSS) polar orbiting satellites, received at Casey (66.28 degrees S, 110.5 degrees E), Antarctica, were used to investigate the amplitude scintillations on 150 MHz and the Ionospheric Total Electron Content obtained using the Differential phase technique. The differential phase technique, measuring the phase difference between the two coherent transmissions on 150 MHz and 400 MHz from the NNSS satellites, permits only relative TEC changes to be calculated. Absolute TEC is estimated from the relative TEC using the f_oF2 obtained from the digisonde records from Casey station or from GPS measurements. A JMR-1 satellite receiver system is used to obtain the phase and amplitude data, with all measurements logged on a PC. A special antenna with high gain at high elevation enabled the reception of high quality signals from the NNSS satellites. Scintillation measurements were obtained from a purpose built receiver, attached to the 24 MHz IF output of the JMR. Investigations of the ionospheric enhancements known as polar patches, and the depletions, known as polar holes were carried out. In order to locate the patches and polar holes, the TEC data are mapped in MLT magnetic co-ordinates. Comparisons to results similarly obtained from GPS satellites are also made. The results obtained are in agreement with the earlier findings. However, comparisons with models indicate large discrepancies when patches and holes are present.

Keywords: GPS; NNSS; polar holes; polar patches; TEC

Introduction

The polar cap station Casey is the ideal location to investigate the occurrence of holes, patches and associated scintillation in the Southern high latitude ionosphere. TEC was monitored using the constellation of NNSS polar orbiting satellites. The NNSS satellite constellation consists of four active satellites, with several others on standby at any given time. Completing approximately thirteen orbits per day, the satellites are visible two or three times a day above an elevation of 45° at any given fixed site.

Total electron content (TEC) theory

Total electron content is defined as the number of electrons in a volume of one square meter in cross-section, extending along a ray path from a satellite to a ground receiver.

$$TEC = \int_P N(s)ds\,. \tag{1}$$

[1]School of Physics, Faculty of Science and Technology, La Trobe University, Bundoora, Vic 3083, Australia, e-mail: e.essex@latrobe.edu.au

Using the differential phase method this becomes:

$$\int_0^{h_s} N dh = A \cos \chi_m \left(\int \frac{\dot{\Psi}}{\lambda_0} dt + D \right) , \tag{2}$$

where $A = 1.2969 \cdot 10^{15}$ m^2.

Ordinary critical frequencies (f_oF2) are used to generate a baseline which can then be used to calculate absolute TEC (Fox and Mendillo 1991).

$$TEC = 124 \cdot 10^{13} (f_o F2)^2 \cdot \tau , \tag{3}$$

where τ = ionospheric slab thickness.

The TEC values are plotted using magnetic co-ordinates (MLT).

Scintillation theory

Variations in amplitude, phase or angle of arrival of radio signals are known as scintillations. These effects result when a radio wave propagating through the ionosphere is diffracted by irregularities which are moving relative to the raypath. Scintillations are characterised by the scintillation index S_4, which provides a "level of scintillation activity". S_4 is defined as;

$$S_4 = \frac{\left(\overline{P^2} - \overline{P}^2 \right)^{1/2}}{\overline{P}} , \tag{4}$$

where $\overline{P}$ is the average power received.

Location of experiment

Casey Station (formerly Wilkes) was the third permanent ANARE station to be established on the Antarctic mainland. Casey is situated at the geographic location of 66.3°S, 110.5°E, with the magnetic co-ordinates -80.4Λ, $L = 35.9$. Its position, inside both the cusp and auroral region, make it an ideal place to monitor the polar hole. An example of all NNSS passes over a 24 hour period, in relation to Casey is shown in Fig. 1a. All GPS passes visible in the same time span are also shown in Fig. 1b.

Equipment

Phase and amplitude data were recorded using equipment located at Casey, Australian Antarctic Territory. The equipment consisted of a JMR satellite receiver, and an IBM-compatible PC. The PC is used to control the JMR receiver, and is also used to record the differential phase and signal strengths to hard disk. This data are also backed up onto cartridge for permanent storage. High quality signals are obtained from the NNSS satellites due to the use of an antenna which consists of

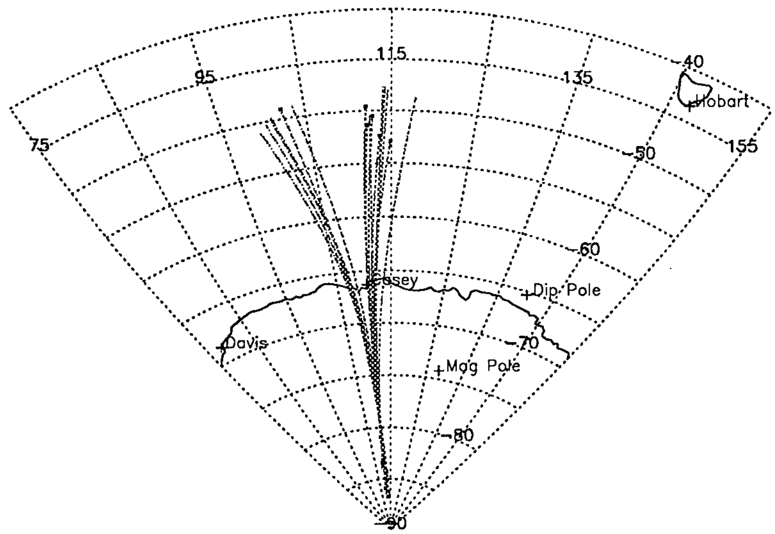

Fig. 1a. Satellite coverage as seen from Casey during a 24 hour period for NNSS

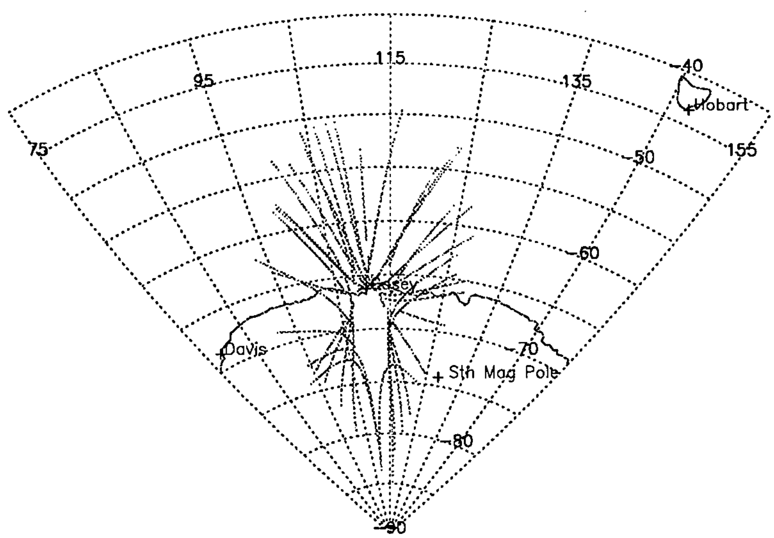

Fig. 1b. Satellite coverage as seen from Casey during a 24 hour period for GPS

two, short helical coils tuned to 150 MHz and 400 MHz respectively. These coils have polar patterns which enable high gain at high elevations to be received. Scintillation measurements are taken using a receiver, attached to the 24 MHz IF output of the JMR. The receiver allows amplitude variations to be recorded, together with differential phase. f_oF2 is collected using the DPS-4 ionospheric sounder located

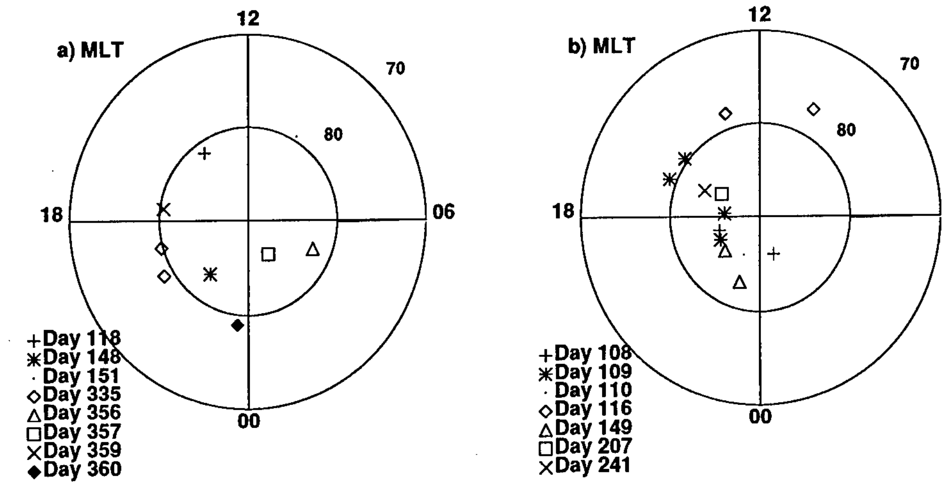

Fig. 2. Locations of Patches as seen by NNSS for a) 1994 and b) 1995, plotted in magnetic co-ordinates

at Casey, provided courtesy of Auroral and Space Physics, Australian Antarctic Division. Data are collected for approximately 15 days per month, separated into 5 days of scintillations and TEC and 10 days of TEC only being recorded. Samples of both differential Doppler and scintillations are ftp'd to La Trobe once a month. The bulk of the data is archived and returned to Australia at the end of the year.

Patches

Solar produced F-region plasma is carried through the dayside cleft and into the polar cap by anti-sunward convection from the post-noon ionosphere. This plasma enters the polar cap as a tongue of ionisation which provides the source for enhanced polar cap F-region plasmas, or 'patches' which are observed at high polar latitudes away from noon. Up to 5 times to 10 times above background level, these patches are localised regions of increased F-region density, which can be up to 1000 km across. Patches are thought to occur most often in April and August, and less likely to occur in January and July (Rodger and Graham 1996). Patches are most likely to occur when the B_z component of the IMF is southward, or when $K_p > 4$. It is possible to track these patches using the method of differential phase determination of columnar TEC, and hence determine some of the dynamics of the polar cap ionosphere (Beggs et al. 1994). Using the above conditions as a guide, patches were located on several occasions during the period of April 1994 through to August 1995. These patches are plotted in magnetic co-ordinates (see Fig. 2), and selected samples are plotted in geographic co-ordinates (see Fig. 3). GPS data was also analysed for the month of April, 1995. The location of suspected patches found from these measurements is shown in Fig. 4, with a sample plotted in both UT and MLT shown in Fig. 5.

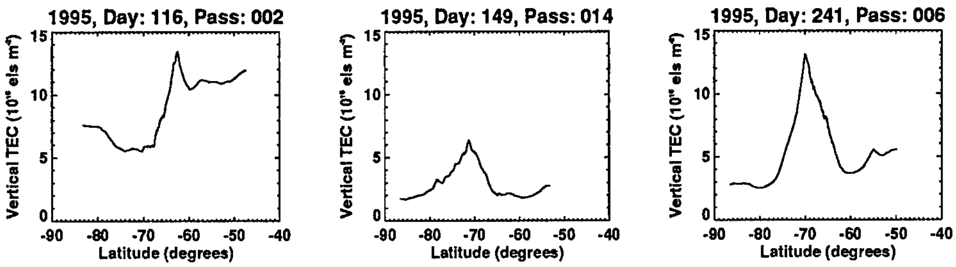

Fig. 3. Selected patches as seen by NNSS from 1995, plotted in geographic co-ordinates

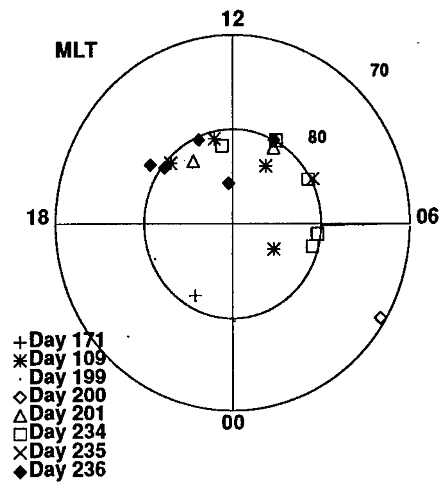

Fig. 4. Locations of Patches as seen by GPS for 1995, plotted in magnetic co-ordinates

Holes

The ionisation 'hole' poleward of the nightside auroral zone first became evident during the late 1970's (Brinton et al. 1978 and Crowley et al. 1993). It arises due to the long transport time of ionisation from the dayside across the dark polar cap. The polar hole is expected to be located in the post-midnight sector (0–3h MLT) when the IMF B_z is southward with a positive B_y, whilst it is expected to be found in the pre-midnight sector of the polar cap (21–24h MLT) when the IMF B_z is southward with a negative B_y. It is also expected that the polar hole ionisation density is lowest during winter with a minimum density in the southern hemisphere at 20.3h UT for all seasons. This hole can also be located using differential phase TEC measurements. The hole was located at various times, during the period of April to August 1995, for both IMF B_z, $B_y < 0$, and for IMF $B_z < 0$, $B_y > 0$. These locations are plotted in magnetic co-ordinates, as shown in Fig. 6, and for selected passes in geographic co-ordinates as shown in Fig. 7.

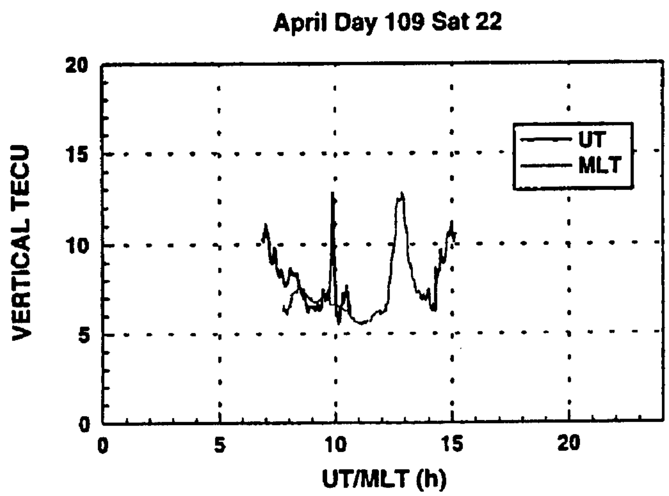

Fig. 5. A patch in April 1995, as seen by GPS, plotted in UT (solid line) and MLT (dotted line)

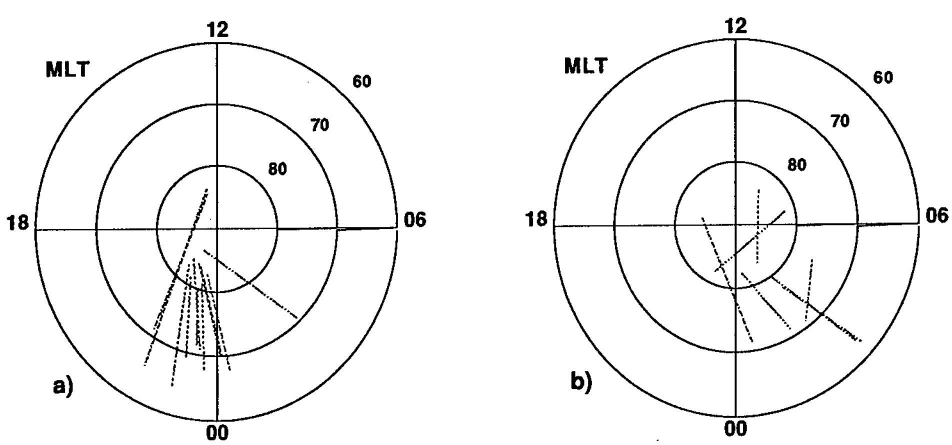

Fig. 6. Locations of Holes during 1995, plotted in magnetic co-ordinates with a) IMF $B_y < 0$, and b) IMF $B_y > 0$

Comparisons with models

Selected TEC passes were compared to results from the Parametrized Ionospheric Model (PIM). Clearly, the results obtained experimentally do not correspond particularly well with the expected results obtained from PIM. PIM does not give the correct background levels of TEC for most of the passes analysed. The experimental background levels were between 5–10 TEC units different to that predicted by PIM. PIM also does not predict the position of the polar hole with any level of certainty. Some samples of these measurements are shown in Fig. 8.

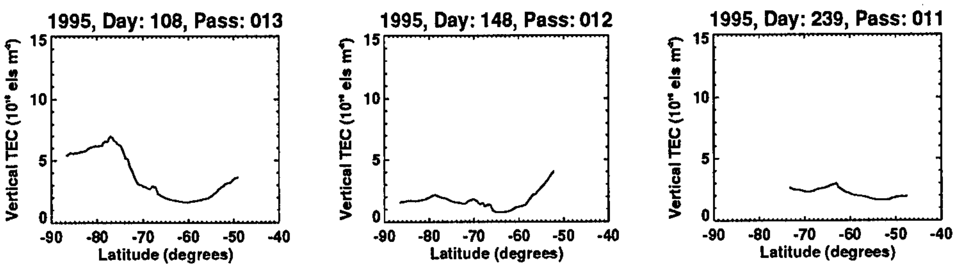

Fig. 7. Selected NNSS satellite passes from 1995 showing holes, plotted in geographic co-ordinates

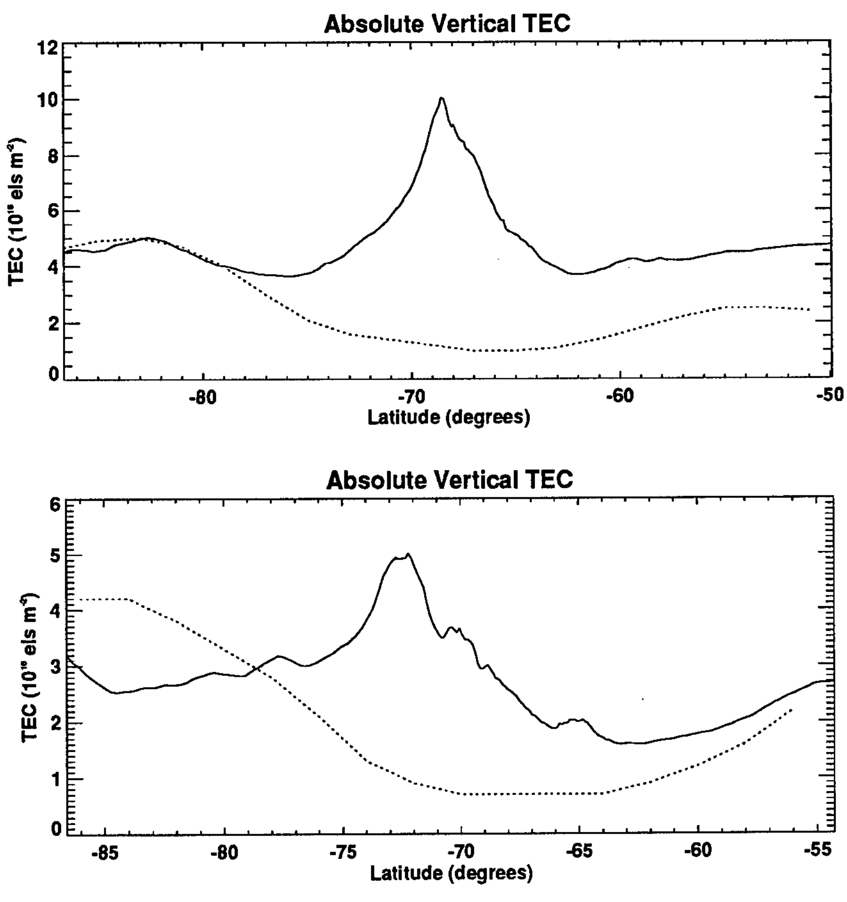

Fig. 8. Selected NNSS absolute TEC measurements (solid line), showing related PIM results (dotted line) as a comparison

Discussion

The ionisation 'hole' was observed on several days during the months of April to August 1995. The hole was predominantly situated between –70 to –80 invariant latitude, between 21–24h MLT ($B_y < 0$), and 0–3h MLT ($B_y > 0$). Patches were observed in the –80 to –90 invariant latitude region, predominantly between 12–24h MLT, on several days throughout the periods of April to November 1994, and April to August 1995. November 1994 and April 1995 were the times when patches were most often observed. TEC levels rose by a factor of 2 times to 4 times that of background levels during the event of a patch. Strong scintillation was observed on several occasions when TEC levels rose significantly compared to background levels. Two patches were identified at the same location using both GPS and NNSS measurements (see Figs 2b and 4). Optical measurements will be needed to ascertain if these are in fact the same patches.

Conclusions

This study shows that the method of differential phase determination of total electron content can be used to locate patches and holes in the polar cap ionosphere. Patches were observed using NNSS satellite passes on a total of seven days during 1995, and eight days during 1994. Several of the patches located using NNSS were verified by comparing similar results obtained using GPS satellite measurements. Patches were only located for times of IMF $B_z < 0$, and in regions of –80 to –90 invariant latitude. Holes were found over a five month period from April to August 1995, in two regions, dependent on whether IMF B_y was positive or negative.

Acknowledgements

Special thanks go to Messrs. Lloyd Symons and Dale Siver, Casey wintering engineers 1993 and 1994 respectively, and Dr. Didier Monselesan, Casey wintering physicist 1995, for assistance with data collection. Thanks also to Dr. Anthony Breed, from the Australian Antarctic Division, for assistance with data analysis software. Also thanks to Mr. Robert Polglase of La Trobe University for help with technical matters, and to Mr. Paul Smith for providing f_oF2 and IMF data. This research is supported by an Antarctic Science Advisory Council (ASAC) grant, and by logistic support from the Australian Antarctic Division. Natalie Shilo is supported by an Australian Postgraduate Award (APA) scholarship.

References

Beggs H M, Essex E A, Rasch D 1994: *J. Atmos. Terr. Phys.*, 26, 659.

Brinton H C, Grebowsky J M, Brace L H 1978: *J. Geophys. Research*, 83, 4767.

Crowley G, Carlson H C, Basu S, Denig W F, Buchau J, Reinisch B W 1993: *Radio Science*, 28, 401.

Fox M W, Mendillo M 1991: *Radio Science*, 26, 429.

Kersley L, Pryse S E, Wheadon N S 1988: *Radio Science*, 23, 320.

Rodger A S, Graham A C 1996: *Ann. Geophys.*, 14, 533.

Acta Geod. Geoph. Hung., Vol. 33(1), pp. 91–95 (1998)

NEW NNSS CONFIGURATION: PROBLEMS AND ADOPTED SOLUTIONS

L CIRAOLO[1] and P SPALLA[1]

The new operational configuration of NNSS involves problems concerning some aspects of TEC evaluation from Doppler measurements. One of these is the different frequency offset needed for satellites operating on the "maintenance frequency". The second one, common to all NNSS satellites, is due to the message no more updated. This implies unavailability of satellite identification, orbital information, capability to set stationtime. The solutions adopted for IROE doppler stations are described.

Keywords: differential Doppler; NNSS; orbital elements; timing

At the beginning of 1997, the Navy Navigation Satellite System (NNSS) has been disabled from being standard service for navigation. The performance of the system has been changed as synthetically sketched in Table I. Given that the two carriers have been kept on, it is possible to continue acquiring Differential Doppler. Many other characteristics that make us able to design a stand-alone system changed. Some satellites have been switched to the so-called Maintenance Frequency (MF), changing the offset from –80 ppm to –150 ppm. The message, which carried information about orbital elements, satellite identification and the way to synchronize to the NNSS time scale, are no more updated. The only usable information is the satellite identification wired in the on-board hardware. In this new situation, the stand-alone system could provide only Doppler Differential measurement, but lacking completely any information concerning the actual positions of the satellite, needed to extract TEC.

In order to provide this information, the old system (left drawing in Table II) has been developed as described in the right side of Table II, according to the following directions:

1. Provision of an external switchable oscillator to enable the reception of the MF satellites, too.

2. Use of a commercial GPS receiver board, to provide synchronization of PC time to GPS time. This solution has been adopted in order to be able to locate the receivers in any site.

3. Downloading of the NORAD orbital elements from the Web page of Grove Enterprise inc., in charge of Dr. Tohmas S Kelso. These elements will be used both in the data analysis after the observations, and in preparing alerts to be sent to the receiving stations.

The former setup, developed at IROE, was presented at BSS94 (Ciraolo et al. 1994) and it is here reported in Fig. 1. The system operated fully on a stand-alone

[1]Istituto di Ricerca sulle Onde Elettromagnaetiche "Nello Carrara", Firenze, Italy

Table I. Status of NNSS before and after January 1997

NNSS Status
Beginning 1997

HI channel: 400 Mhz - 80 ppm	HI channel: 400 Mhz - 80 ppm or -150 ppm
LO channel: 150 MHz - 80 ppm	LO channel: 150 MHz - 80 ppm or -150 ppm
HI & LO channel phase modulated by same message (MSG)	LO channel modulation: telemetry HI channel phase modulation as before
containing:	containing:
Satellite Identification	Wired Satellite Number
Orbital Elements	Remaining information meaningless
NNSS Time Scale	

way. In fact it provided acquisition of Differential Doppler and message decoding, from which ephemeral information and timing were obtained. It has been operating for three years, till the end of standard service of NNSS, in the locations of Gibilmanna and L'Aquila. This system was designed using commercial Geodetic Receivers (GeoRx) according to the same conceptual scheme used by most investigators, i.e. interfacing the GeoRx to a Personal Computer (PC) (both pieces of commercial equipment) via a suitable, expressly designed circuitry. Great effort was made to make the solution as more versatile as possible, and to reduce the needed electronics at minimum. This was possible using for most of signal processing the software approach.

A very simple single board interface accesses three signals inside the GeoRx, namely the HI and LO Doppler, and the HI channel phase detector output, performing:

1. Hard limiting of the phase detector output and generation of a Doublet rate, both signals at TTL level.
2. Evaluation and digitalization of the phase difference between the properly scaled HI and LO Doppler signals.

Once fed into the PC, the signals were processed by a suitable software, which controlled the system initialization and system monitoring and maintenance, too.

The only operator attendance requested was a periodic check of system performance and the change of data diskette every second week.

The new operational configuration of NNSS excludes the capability to realize a fully stand-alone system. In fact, timing and ephemeral information must

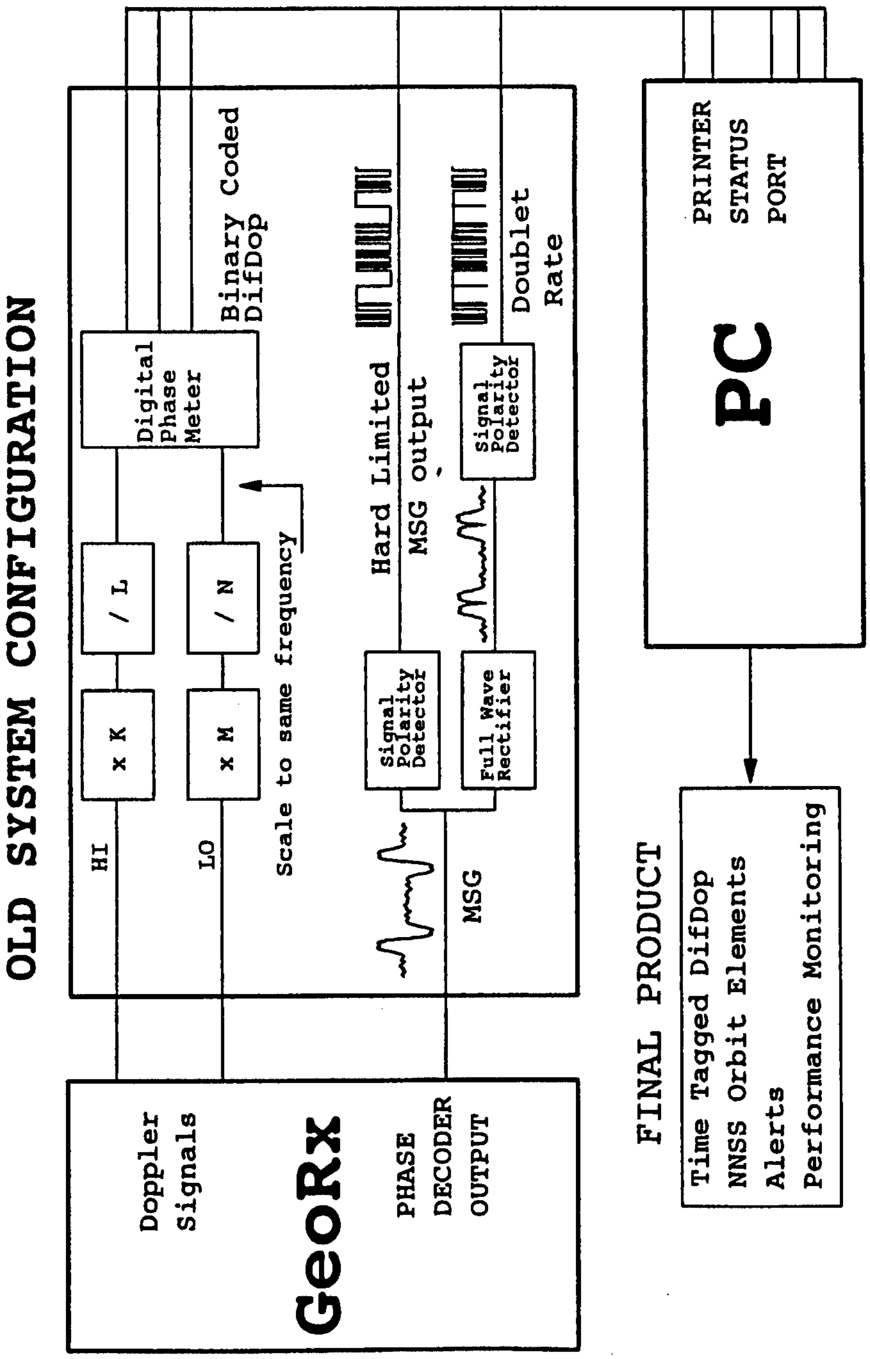

Fig. 1. Configuration of the receiving system for NNSS before January of 1997

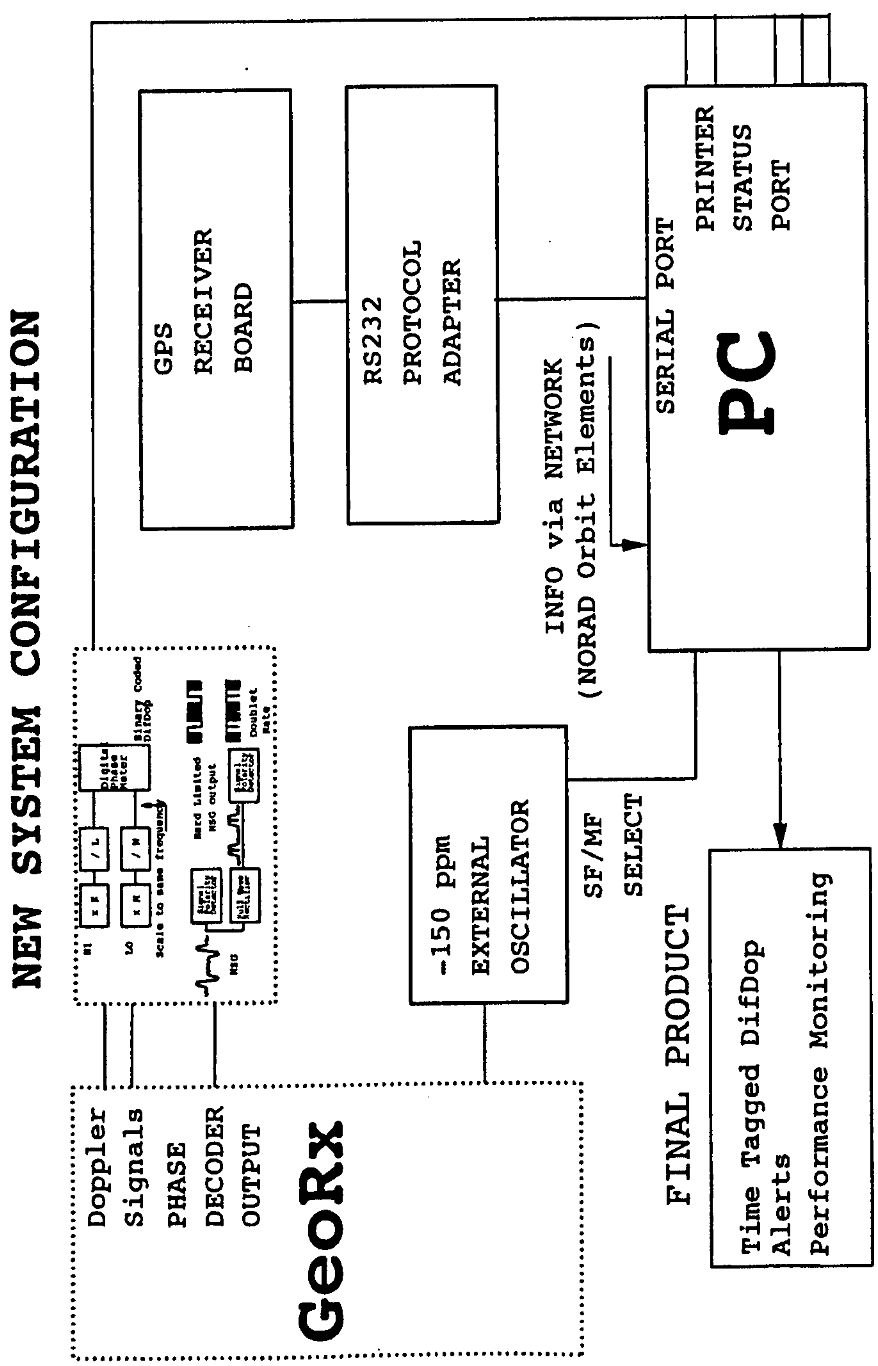

Fig. 2. Configuration of the receiving system for NNSS after January of 1997

Table II. Sketch of the receiving system before and after January 1997

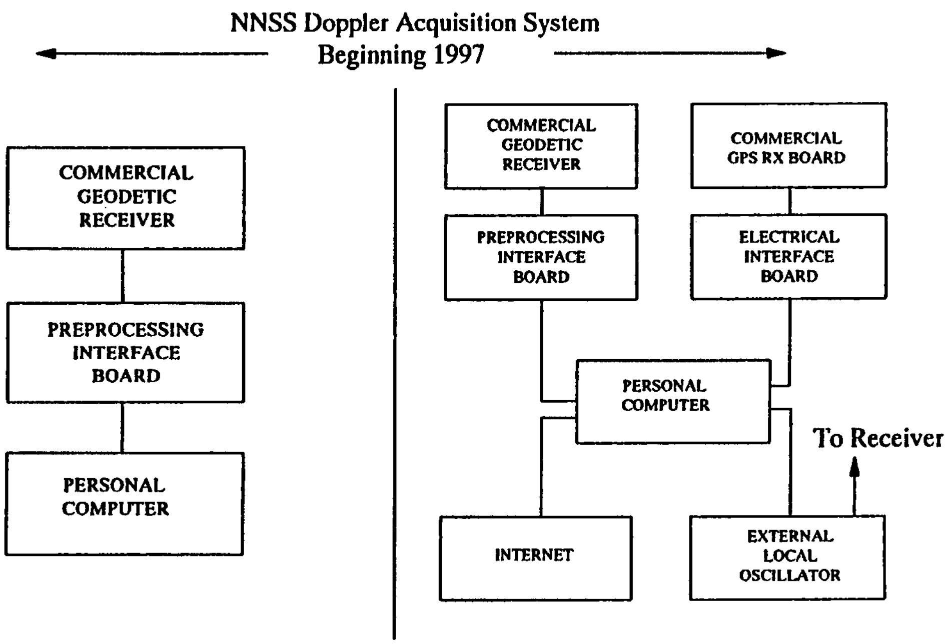

be provided by means external to NNSS. A very convenient way to perform time synchronization is using a commercial GPS board receiver, which, for the global peculiarities of GPS itself, is able to operate practically everywhere any time. This implied additional software to keep PC time synchronised to GPS time. Concerning timing, the receiver can be considered still stand-alone.

Once a precise timing is provided, the real time knowledge of the orbital elements during the measurements is not essential. Nevertheless, their use is recommended to give the operator alerts, a useful tool to check the performance of the station. This is one of the reasons by which we provide orbital elements to the stations. Another good reason is that we are setting up an automatic procedure to switch the receiver to MF or SF according to the scheduled pass. Orbital elements files are obtained via Internet, and distributed to the stations on a montly basis. The evaluation of the alerts occurs automatically at the beginning of each day.

In conclusion, all the components of the old system are still used, providing Differential Doppler and message decoding: this operation gives only a hardwired satellite identification, which is very effective in the following data analysis. An overall sketch of the modifications and new developments are shown in Fig. 2.

References

Ciraolo L, Spalla P, Capannini E 1994: In: Proceedings of the International Beacon Satellite Symposium, Aberystwyth, UK

Acta Geod. Geoph. Hung., Vol. 33(1), pp. 97–109 (1998)

DETECTION OF THE SOUTHERN HEMISPHERE MAIN TROUGH, EFFECTS OF AURORAL ACTIVITY AND NIGHTTIME TEC ENHANCEMENTS WITH GPS

I HORVATH[1] and E A ESSEX[1]

Total electron content (TEC) values are obtained from measurements of the Gobal Positioning System (GPS) satellite signals at the Australian and sub-Antarctic receiver stations situated at mid and high latitudes in the southern hemisphere. A technique was developed to derive GPS TECs from raw data files. The reduced data of 1995 and 1996 were used to investigate the diurnal and seasonal variations of the TEC in the region. Various features were also studied such as the mid-latitude trough, the effects of auroral activity on GPS recording and nighttime TEC enhancements. The latitudinal motion of the mid-latitude through was observed as well as the magnetic activity dependence of the geographic location of the auroral oval. The seasonal variation in the time of occurrence of nighttime TEC enhancements was also investigated. The GPS findings were compared with TEC from TOPEX/POSEIDON satellite and f_0F2 data. Theoretical TECs were obtained by employing an ionospheric model called PIM (Parameterized Ionospheric Model), and results were compared with experimental values.

Keywords: auroral oval; mid-latitude through; nighttime TEC enhancement; TEC

Introduction

The aim of this study was to develop a procedure to derive GPS TECs from raw data files and to monitor the ionization of the upper atmosphere in the Australian and sub-Antarctic regions in order to investigate various ionospheric formations. The results from GPS were compared with TOPEX/POSEIDON TEC and ionosonde data.

The area of study comprises the mid latitude Australian and the high latitude sub-Antarctic regions. Here, the following Australian and New Zealand dual frequency GPS recording stations are situated: Ceduna, Tidbinbilla, Hobart, Wellington and Macquarie Island (see Table I and Fig. 1). Three stations are particularly significant both latitude-wise and longitude-wise and these are Tidbinbilla, Hobart and Macquarie Island. The geographic longitudes of these stations are very similar meaning that the universal time of GPS recording is almost the same. Latitude-wise these stations are relatively closely spaced, therefore provide a continuous North-South latitudinal TEC coverage. The significance of the sub-Antarctic station of Macquarie Island is also related to its unique position in the auroral zone characterized by a relatively low geographic latitude (54.4°S) and at the same time a high geomagnetic latitude (65.°S) (Lambert and Cohen 1986).

[1]School of Physics, La Trobe University, Bundoora, Vic., 3083, Australia, e-mail: e.essex@latrobe.edu.au

1217-8977/98/$ 5.00

Table I. List of receiver sites used for GPS sallite data collection

Station	Country	GPS Receiver	Geog.lon. (°E)	Geog.lat. (°S)	Agency
Ceduna	Australia	R SNR-8100	133.81	31.87	AUSLIG
Hobart	Australia	R SNR-8100	147.43	42.80	AUSLIG
Macquarie Island	Australia	R SNR-8100	158.94	54.50	AUSLIG
Tidbinbilla	Australia	R SNR-8	148.97	35.38	NASA/JPL
Wellington	New Zealand	R SNR-8100	174.78	41.27	AUSLIG

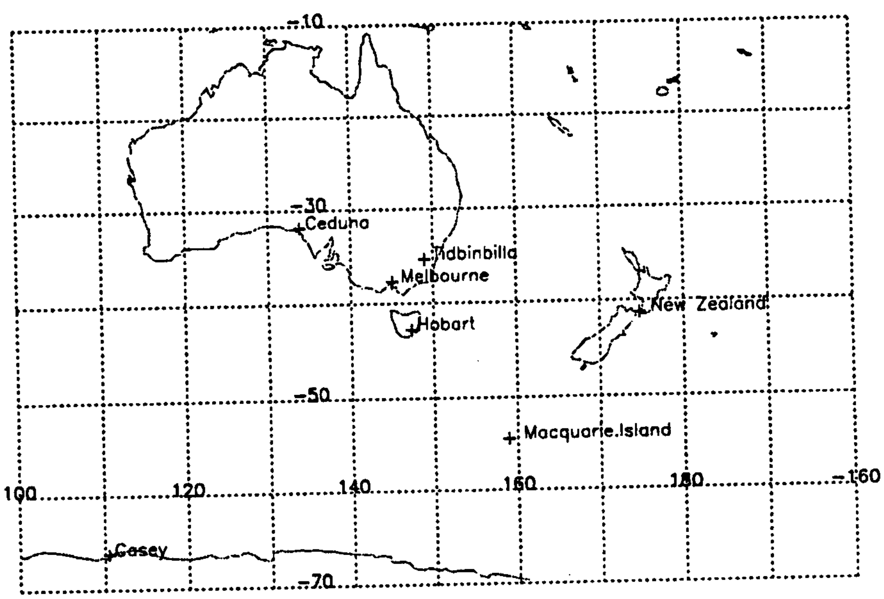

Fig. 1. Map of the area of interest illustrating the location of GPS receiver sites in the grid of geographic co-ordinates

This project makes use of dual frequency GPS measurements to map the ionization of the upper atmosphere in the area of interest. In GPS satellite experiments, GPS users correct for ionospheric errors on two L — Band radio signals ($L1$ = 1.57542 GHz; $L2$ = 1.22760 GHz) that propagate earth-space. Two of these errors are known as carrier phase advance ($\Delta\phi$) and group path delay (ΔT). They offer the opportunity to evaluate the quantities of differential carrier phase ($\delta\Delta\phi$) and differential time delay ($\delta\Delta T$) at the two frequencies, and their combination allows one to derive the total electron content along the line of sight unambiguously (Klobuchar 1994). Since the orbital height of GPS satellites (20183 km) is in the range of the plasmasphere, therefore GPS TECs are the sum of ionospheric and plasmaspheric contents.

The ground based GPS measurements were combined with satellite data of the

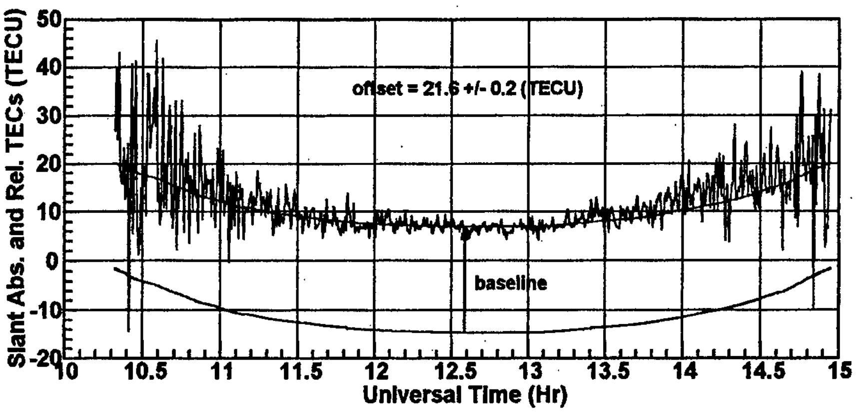

Fig. 2. Plots showing absolute and relative TECs representing a less accurate absolute scale (top curve) and a more accurate relative scale (bottom curve) and the concept of baseline

TOPEX/POSEIDON mission in order to investigate ionospheric processes separately. The TOPEX/POSEIDON mission started in 1992 and one of its main objective is to accurately measure the height of the sea surface. Since the satellite carries a dual frequency ($f_1 = 5.3$ GHz; $f_2 = 13.6$ GHz) altimeter system on board and the orbital height of the satellite (1330 km) is in the range of the ionosphere, unambiguous ionospheric TEC measurements over the Pacific, Indian and Atlantic Oceans are available for the scientific community.

Theory and satellite techniques

Due to the presence of a large number of electrons, propagating transionospheric radio signals experience a complex carrier phase change (ϕ), where the ionospheric component is known as ionospheric carrier phase advance ($\Delta\phi$). At the same time, there is a certain amount of retardation or delay on the modulation of radio waves and the time delay is called group path defect (ΔT). If the number of frequencies is two, the terms differential carrier phase ($\delta\Delta\phi$) relative to the lower frequency (see Eq. (1)), and differential time delay ($\delta\Delta T$) between the two frequencies can be determined (see Eq. (2)).

$$\delta\Delta\phi = +\frac{K}{2cL_2}\left(\frac{m^2-1}{m^2}\right)\int_0^s N ds\,, \tag{1}$$

$$\delta\Delta T \approx \frac{K}{2c}\left(\frac{1}{L_2^2}-\frac{1}{L_1^2}\right)\int_0^s N ds\,, \tag{2}$$

where $K = 80.62$ (m^3/s^2), $m = L_1/L_2 = 1.2833$, N = electron density (e^-/m^3).

Dual frequency GPS users make use of these erors, which can be obtained from the direct outputs of ground based receivers and they give the opportunity to obtain

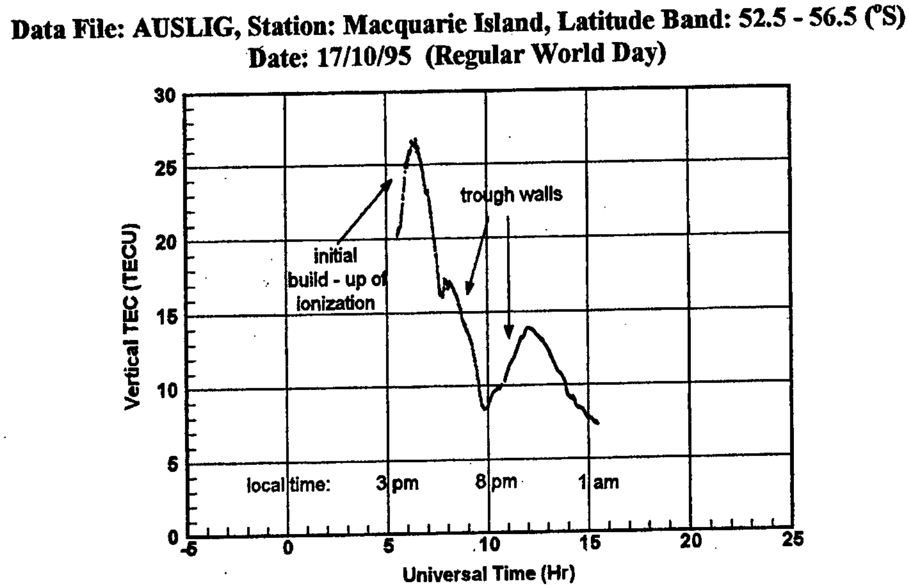

Fig. 3. A daily TEC plot depicting a day-time vernal equinox trough

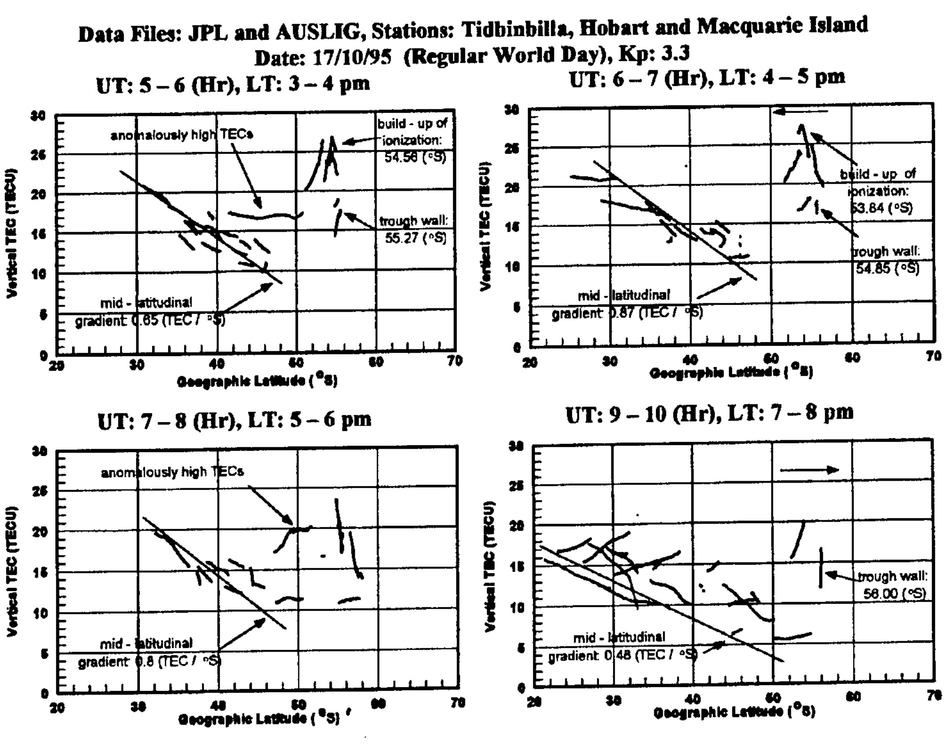

Fig. 4. Hourly latitudinal maps depicting a day-time vernal equinox trough

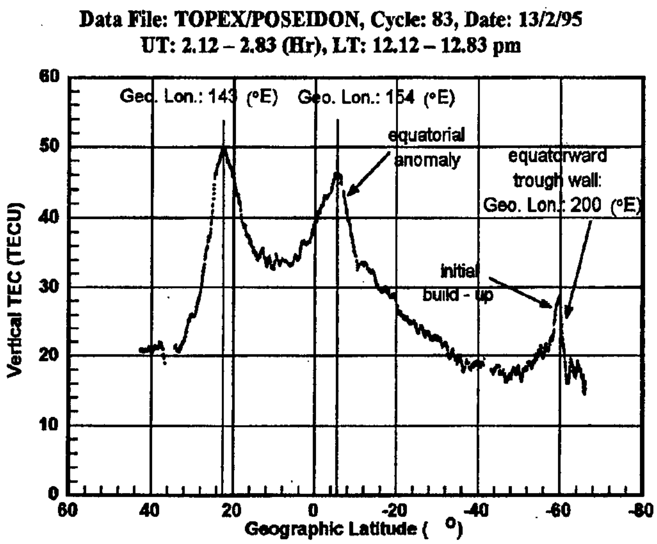

Fig. 5. A latitudinal map depicting the equatorial anomaly and a day-time autumnal equinox trough

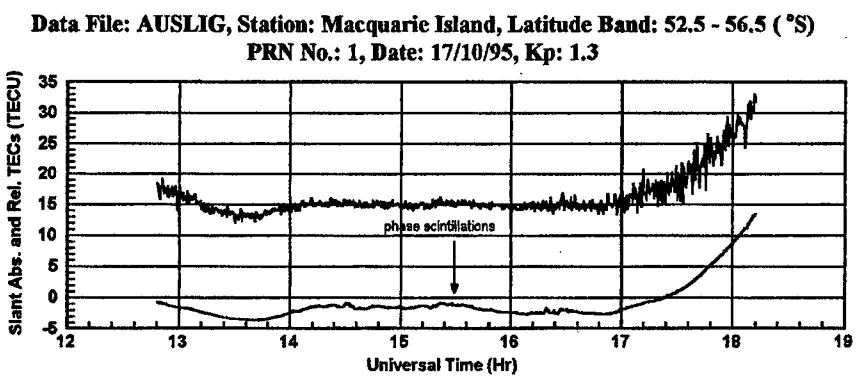

Fig. 6. A digital plot depicting the scintillation of carrier phase signal as a response to auroral disturbance

the values of slant relative and slant absolute TEC, respectively. By plotting the raw GPS data against the time of recording (see Fig. 2), it is clearly seen that the curve of slant absolute TEC is a noisy absolute scale, while the graph of slant relative TEC shows a smooth relative scale.

In order to obtain the values of true slant TEC, a baseline for the relative scale is determined by fitting it to the absolute scale (see Fig. 2 and Eq. (3)). With the knowledge of the orbital elements of the satellite, a vertical content can be obtained (see Eq. (4)).

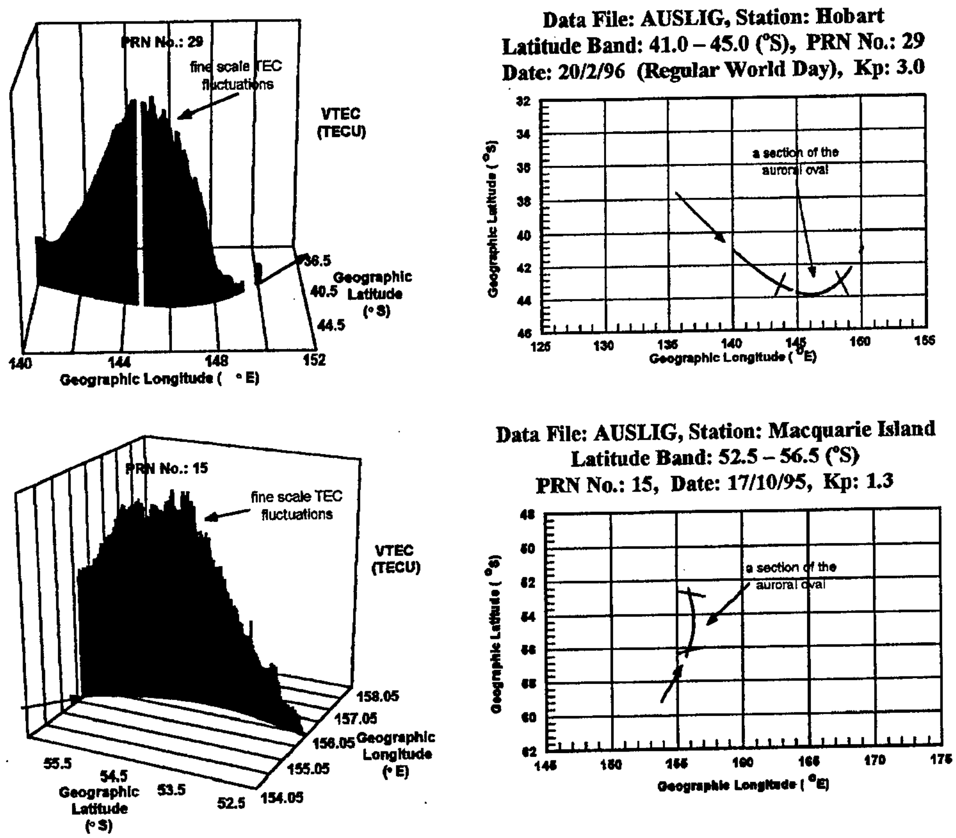

Fig. 7. Plots depicting auroral disturbance related small scale TEC fluctuations (left panel) and the location of the activity itself in the grid of geographic co-ordinates (right panel)

$$\text{slant TEC} = \int_0^s N ds = \frac{2cL_2}{K}\left(\frac{m^2}{m^2-1}\right)\delta\Delta\phi + \text{baseline} \tag{3}$$

$$\text{vertical TEC} = \text{slant TEC} * \overline{\cos\chi}\,. \tag{4}$$

The TOPEX/POSEIDON ocean altimetry satellite measures an apparent height (P) instead of true height (R), due to the dispersive effect of the ionosphere. Dual frequency TOPEX/POSEIDON users make use of the height correction (ΔR in milimetres) carried out relative to the higher frequency (see Eq. (5)). Since this term is proportional to the number of free electrons encountered, a vertical iono-

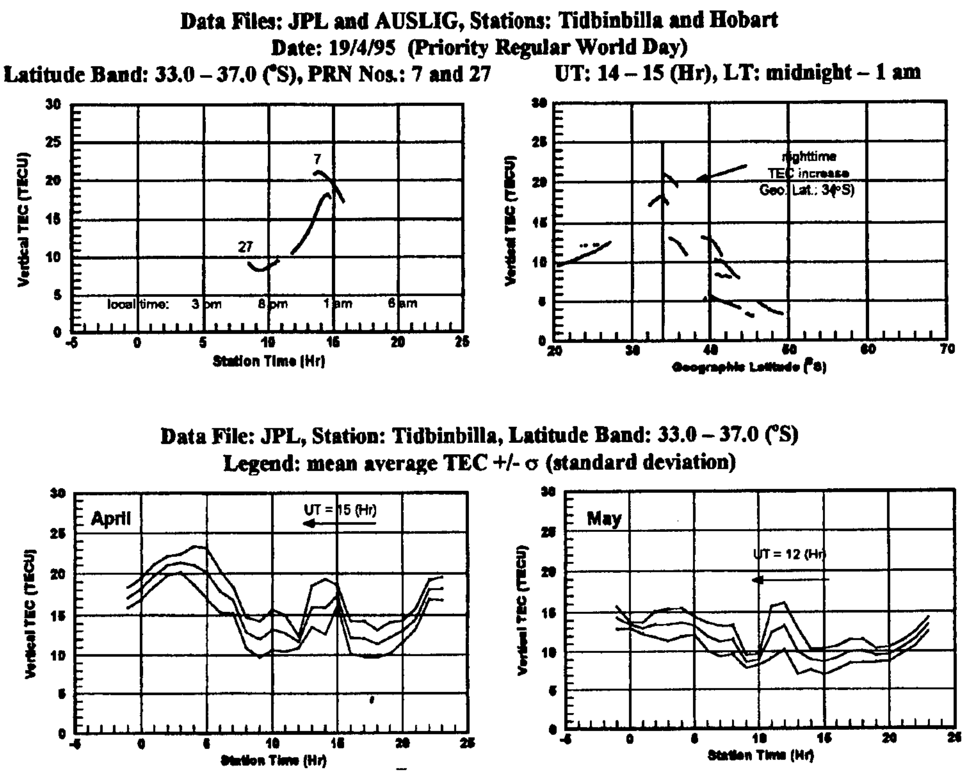

Fig. 8. Daily (top left panel) and hourly (top right panel) plots of GPS TECs depicting a nighttime TEC enhancement occurring in the month of April 1995 and plots of monthly mean average TECs depicting an ionization build-up occurring in different time sectors and its forward movement in time (bottom panel)

spheric TEC can be obtained (see Eq. (6)) (Imel 1994).

$$\Delta R = P - R = -\frac{K}{2f^2}\int_0^s N ds \tag{5}$$

$$\text{vertical TEC} = \frac{\Delta R * f^2}{-403}\,. \tag{6}$$

Data processing procedure

A large GPS database was established by regular downloading through Internet during the calendar years of 1995 and 1996. According to availability, JPL and AUSLIG data files had been collected, which are published in a common Receiver Independent Exchange Format (RINEX). The raw data files were reduced to GPS TECs by using computer programs designed to automate not only the procedure

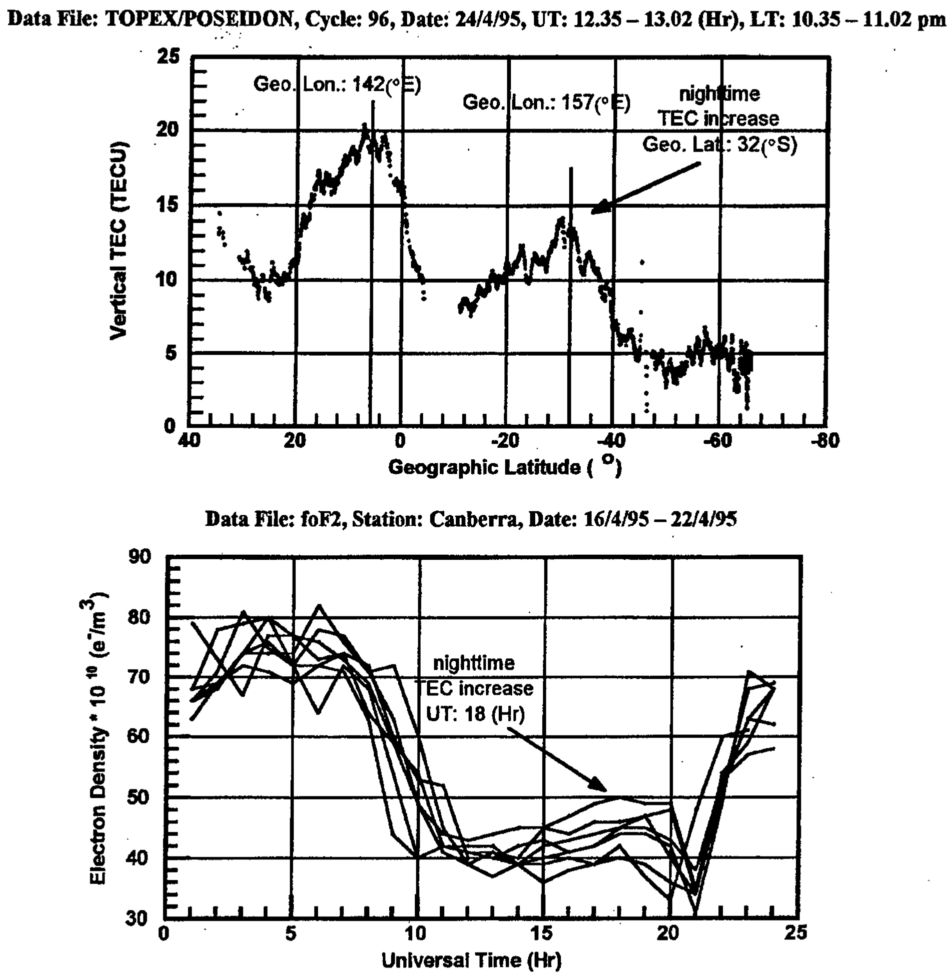

Fig. 9. TOPEX/POSEIDON (top panel) and f_0F2 plots of seven days (bottom panel) imaging a nighttime TEC enhancement occurring in the month of April 1995

of curve fitting, but also the task of cycle slip correction prior to any offset calculation. The calibration values of the biases of the two GPS transmitted signals for each satellite were incorporated into the computation of true slant TEC values. The biases for the Tidbinbilla GPS receiver were also incorporated and used as a calibration for the other GPS receivers.

The TOPEX/POSEIDON data are stored on CD-ROMs, where each CD contains the recordings of two complete cycles and each cycle is made up of 254 passes. In order to deal with the huge database efficiently, an algorithm was written to select passes that might contain the features of interest. The raw satellite data were reduced to vertical TECs by employing a computer program constructed to carry

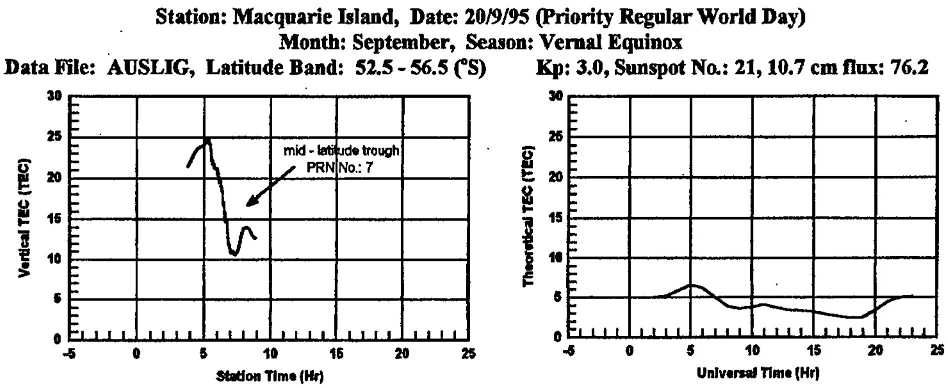

Fig. 10. A daily GPS plot depicting a vernal equinox daytime trough (left panel) and a PIM derived TEC curve constructed for the same day

out all the necessary calculations. The values of vertical TEC were averaged over 20 seconds along the satellite track in order to minimize the noise effect due to wave height variations without degrading the accuracy.

Results and discussion

The southern hemisphere mid-latitude trough

The mid-latitude or main trough is a well known ionospheric formation of both hemispheres. The terminology of "main trough" was introduced by Muldrew in 1965 to designate an electron depletion zone, extending in the magnetic East-West direction, in the F2 region. Soon after Muldrew first recognized this persistent nighttime feature from critical frequency data, the same phenomenon was identified and studied from ion trap measurements by Sharp (1966), who named it the "mid-latitude trough". The trough itself is the manifestation of a sudden electron density depletion in the mid latitude ionosphere created by normal F region processes such as plasma convection, ion production and ion loss. In both hemispheres, the trough is situated equatorwards of the auroral oval ($L \approx 4$; $\Lambda \approx 60° - 56°$, according to magnetic activity). As Mallis and Essex (1993) pointed out, the southern hemisphere main trough is not exlusively a nocturnal phenomenon, as is its northern hemisphere counterpart, possibly due to the larger offset between the southern hemisphere geographic and magnetic poles.

In this study, GPS data recorded from Macquarie Island were used to identify the mid-latitude trough in the southern hemisphere. Unfortunately, the data collected did not cover the complete calendar year selected, but still supported the study of the trough in most of the seasons. Adopting the classification of Mallis and Essex (1993), the southern hemisphere main trough was classified as autumnal equinox, winter, vernal equinox or summer trough according to its seasonal occurrence. The seasons are defined as 3 month periods centred on the months of equinoxes or solstices. The best trough findings were in the season of vernal equinox. Daily TEC

profiles were constructed by plotting the values of vertical GPS TEC, originating from a 4 degree latitude band centered on the recording station, against local or station time to show the trough and one plot is presented here (see Fig. 3). As is seen, the characteristics of the trough such as the steep trough walls and the building up of ionization are well defined. While the steep equatorward wall is the manifestation of the sudden electron density depletion, the building up of ionization is an indication of incoming plasma entering into the polar circulation (Foster 1993).

Latitudinal maps are particularly useful to picture the structure of the ionization at mid and high latitudes. These maps were constructed by plotting GPS TEC values, obtained from the recording stations of Tidbinbilla, Hobart and Macquarie Island, against geographic latitudes for a certain one hour time period (see Fig. 4). As is seen, at mid latitudes the vertical TEC increases gradually towards the equator, as is expected according to theoretical predictions, while at high latitudes the trough appears. As these maps are constructed for certain hourly time intervals, by comparing them, the movement of the trough can be concluded. Accordingly the trough came in at 3 o'clock in the afternoon (see top left panel of Fig. 4), then it moved towards the equator (see top right panel of Fig. 4) and later in the afternoon it moved back towards the pole (see bottom right panel of Fig. 4).

TOPEX/POSEIDON data show similar results. Vertical TEC values obtained from TOPEX/POSEIDON satellite data were plotted against geographic latitudes. It is evident on the latitudinal map constructed (see Fig. 5), that the TEC linearly increases towards the equator at mid latitudes, while at high latitudes the trough appears. Here, the features of initial building up of ionization and the equatorward trough wall are well defined. The equatorial anomaly is clearly visible at low latitudes.

The effects of auroral activity on GPS recordings and the magnetic activity dependence of the geographic location of the auroral oval

The signs of auroral activity are the evidence that the satellite beam traveled through the auroral oval. These appear on raw GPS data plots as phase scintillation (see Fig. 6) and on reduced GPS data plots as fine scale fluctuations of TEC (see left panel of Fig. 7).

By plotting the reduced GPS data in forms of 3 dimensional graphs, sections of the auroral oval can be mapped and interpreted in terms of K_p indices. As is known, the 3 hour K_p index is an indicator of magnetic activity. A magnitude of 3.0 indicates a medium magnetic disturbance, while a magnitude of 1.3 shows a magnetically quiet period. From the plots presented here (see Fig. 7) it is evident, that in a more disturbed period the auroral oval is situated at lower latitudes, while in a magnetically quiet period it is located at higher latitudes. It is already a well known fact (Akasofu and Allan 1964), that during magnetically disturbed periods the auroral oval expands and moves towards the equator. From these GPS observations, which are summarized in Table II, this statement can be confirmed.

Table II. Summary of measured parameters related to the sections of auroral oval mapped

Station	Geographic location (°S)	K_p
Hobart	43.2 – 43.8	3.0
Macquarie Island	52.8 – 56.2	1.3

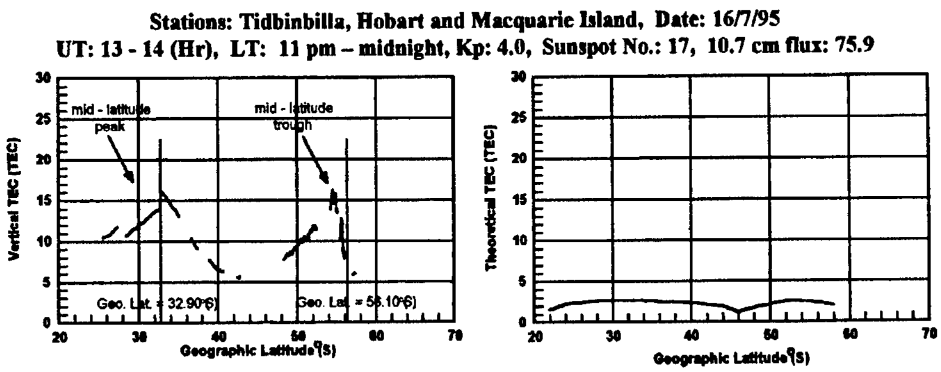

Fig. 11. An hourly graph of GPS TECs depicting various formations (left panel) and a PIM derived TEC curve constructed for the same time interval (right panel)

Nighttime TEC enhancements

The mid latitude ionosphere does not always decrease throughout the night, but shows anomalous increases or enhancements under a wide range of geophysical conditions. Although this fact has been long realized, the phenomenon of nighttime TEC enhancements is neither a familier feature of the mid latitude region nor a frequent topic in the literature. Recently Balan et al. (1991) reported this phenomenon observed in the northern hemisphere and explained its formation with the mechanism of large downflows of plasma in the topside ionosphere.

In this study, 1995 Tidbinbilla and Hobart GPS data showed nighttime TEC enhancements. Daily plots constructed for the month of April 1995 revealed anomalously high TEC values in the nighttime region culminating at 14 hour UT or midnight in local time (see top left panel of Fig. 8). The same phenomenon appeared on latitudinal plots as a well defined single peak formation (see top right panel of Fig. 8). Since this feature had a frequent occurrence in the months of April and May 1995, it appears on the monthly average plots and shows a well defined forward movement in time as the year progresses (see bottom panel of Fig. 8). TOPEX/POSEIDON data confirm these observations (see top panel of Fig. 9) and these are also evident of f_0F2 data (see bottom panel of Fig. 9) recorded from Canberra. TOPEX/POSEIDON plot also indicates conjugate increase in TEC.

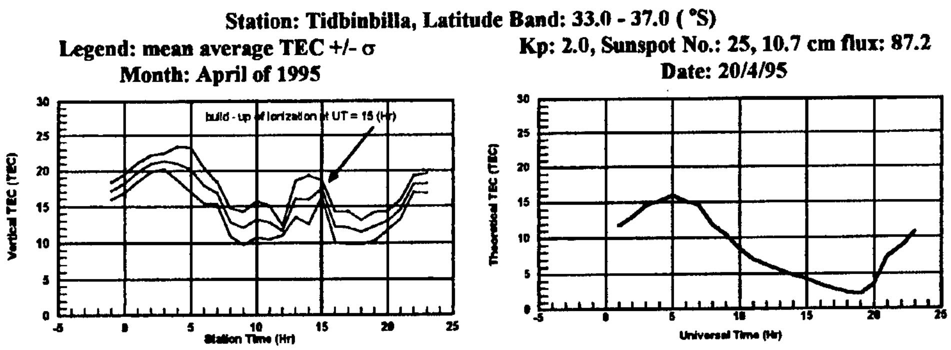

Fig. 12. Digital plots depicting a montly average GPS TEC curve with standard errors featuring a nighttime TEC enhancement (left panel) and a PIM derived daily TEC curve (right panel)

Theoretical TECs

In this study, the Parameterized Ionospheric Model (PIM) provided theoretical TEC values. PIM is a complex global ionospheric model that comprises several regional theoretical models. It generates parameterized outputs that can be fully controlled by specifying the input parameters of the relevant geophysical activities and spatial coordinates. The running of PIM requires the input of a small collection of geophysical parameters such as the daily values of sunspot number and 10.7 cm flux, and the appropriate K_p index. The model offers two options for plots, namely a daily TEC profile constructed for a certain location or an hourly latitudinal plot computed for an optional latitude range and for a certain time interval. For this study, PIM was run to compare some of the findings such as the mid-latitude trough (see Figs 10 and 11) and the nighttime TEC enhancement (see Figs 11 and 12). As is seen on the above illustrations, the model generated plots show little or no resemblance to the ionospheric/protonospheric TEC features observed.

Conclusion and future work

The GPS technique is a valuable tool to study the variability of the ionization of the ionosphere and plasmasphere. The GPS data analysis was useful in the investigation of small and large scale ionospheric formations and the results obtained are in a good agreement with findings of other ionospheric techniques. The ionospheric model called PIM is unsuitable for studies conducted for a low sunspot number time period, where the total content is the sum of ionospheric and protonospheric components. In future work, ionospheric and protonospheric processes can be separated and investigated individually in order to determine the region of origin of the features studied and also to explore the underlying physical processes responsible for their formations. All the results obtained can be used to update currently used ionospheric models.

Acknowledgements

This research is supported by an Australian Telecommunication and Electronics Research Board (ATERB) and an Antarctic Science Advisory Committee (ASAC) grant. I Horvath is a holder of an Australian Postgraduate Award. Special thanks are extended to M Hendy from AUSLIG for the GPS data, JPL for the GPS data and calibration and for the TOPEX/POSEIDON data, IPS for the f_0F2 ionosonde data and N Shilo from La Trobe University Australia for the IDL map. Thanks to P Doherty from Boston College USA, J Klobuchar for Phillips Laboratory USA and A Breed from Australian Antarctic Division for assistance and advice with this project.

References

Akasofu J, Allan R S 1964: *Plan. Space Sci.*, 12, 273–282.
Balan N, Bailey G J, Balachandran Nair R 1991: *Annales Geo.*, 9, 60–61.
Essex E A 1988: *Proc. of the Roy. Soc. of Tas.*, 122, 283–287.
Foster J C 1993: *J. Geoph. Res.*, 98, 1675–1689.
Imel D A 1994: *J. Geoph. Res.*, 99, 24895–906.
Lambert M, Cohen E A 1986: *Radio Sci.*, 21, 347–350.
Mallis M, Essex E A 1993: *J. Atm. Terr. Phys.*, 55, 1021–1037.
Muldrew D F 1965: *J. Geoph. Res.*, 70, 2635–2650.
Sharp G W 1966: *J. Geoph. Res.*, 71, 1345–1356.

Acta Geod. Geoph. Hung., Vol. 33(1), pp. 111–119 (1998)

DETERMINATION OF f_0F2 SHORT-TERM VARIATIONS FROM GPS TIME DELAY OBSERVATIONS

H SOICHER[1] and Z HOUMINER[2]

Reliable HF communications require propagation assessment. Such assessment could be facilitated with the monitoring of ionospheric characteristics by continuously available passive means, i.e., measurements of the total electron content (TEC) using satellite-emitted signals without a need for burdening the electromagnetic spectrum. With the Global Positioning System (GPS) providing instantaneous time delay, or equivalently, TEC, values when needed, an assessment of HF propagation may be available on a near realtime basis.

To assess this possibility a one year study of the correlation between TEC and f_0F2 using GPS time delay observations taken at Matera, Italy and f_0F2 measurements from Rome, Italy, was undertaken during 1995–1996. This is a period of minimum solar activity with sunspot numbers varying between 6–18. The observed correlation coefficient varied between 0.55 in the winter of 1996 to about 0.75–0.8 during the summer of 1995.

In addition to the seasonal variability of the correlation coefficient, a diurnal variability is also present with the coefficient normally maximizing during the day and minimizing in the predawn periods. The predawn minimum may be due to the contribution of plasmaspheric electron content. The correlation coefficient appears to increase with magnetic activity, indicating that TEC and f_0F2 behave similarly during magnetically active periods. Distribution of errors between measured f_0F2 values and predicted ones using a) standard predictions algorithms and b) TEC measurements converted to f_0F2 from a model of slab thickness, show that the errors are reduced when using TEC observations. The errors would be further reduced if the satellite subionospheric point would approach the location of the f_0F2 actual measurement.

Keywords: f_0F2; TEC; variability slab thickness

1. Introduction

HF radio communication depends on the ability of the ionosphere to return the radio signal incident on it back to Earth. Predictions of ionization levels in the various ionospheric regions are derived from models and are used as a basis for planning and frequency management of HF radio systems world-wide. The models permit the calculation of system parameters such as operating frequencies, signal strengths, signal-to-noise ratios, and multipath probability that can be used to describe the performance of HF radio systems. Uncertainties or inaccuracies in the models of the ionosphere have long been known to be one of the major causes if not the major cause, for inaccuracies in the calculated propagation characteristics. This is particularly true for those applications of ionospheric predictions involving timescales that are less than monthly average or monthly median.

To reduce average monthly RMS errors in predictions, adaptive techniques that use real-time observations to correct model biases have been devised. A method that

[1]US Army Communications-Electronics Command Space and Terrestrial Communications Directorate, Fort Monmouth, NJ 07703–5203, USA

[2]Asher Space Research Institute, Technion-Israel Institute of Technology, Haifa, 32000, Israel

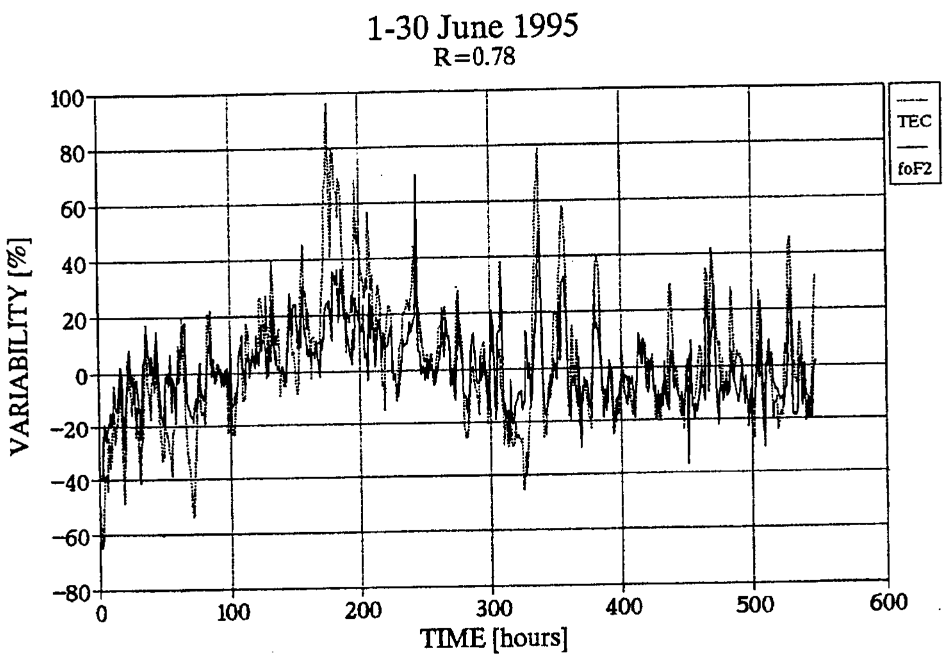

Fig. 1. Hourly values of variability of f_0F2 and TEC for June 1995. R is the cross-correlation coefficient at zero time lag

is potentially global in nature involves the monitoring of GPS signals which yield information on the ionospheric parameters along the propagation path and converting such information into the HF propagation parameters of interest. The advantage of monitoring GPS signals is the fact that it is passive for the potential user, and the existence of a global network of satellites affords the possibility of global coverage. The problem at hand is the conversion of integrated ionospheric parameters along the transionospheric path experienced by the GPS signal to the parameters along the path experienced by the HF sky wave up to the point of reflection from the ionospheric layers. A parameter of great importance in HF propagation is f_0F2, the upper frequency limit for ordinary mode HF vertical propagation, whose square is proportional to $N_{\max}$, the maximum electron density in the ionosphere. The transionospheric parameter of impòrtance is the total electron content (TEC), which is the integrated electron density along the propagation path of a satellite-emitted signal to the observer (TEC $= \int N ds$, where N is the electron density and ds is an element of distance along the path from observer to satellite). Since both TEC and $N_{\max}$ vary diurnally, seasonally, geographically, and in response to magnetic activity, it is expected that their ratio, the so-called slab thickness, τ, will vary to a lesser degree and hence can be modeled more easily. Global models of slab thickness updated with real-time measurements of TEC might possibly yield improved values of $N_{\max}$ and hence f_0F2 for HF propagation.

To test the efficacy of this hypothesis, one has to ascertain the correlation be-

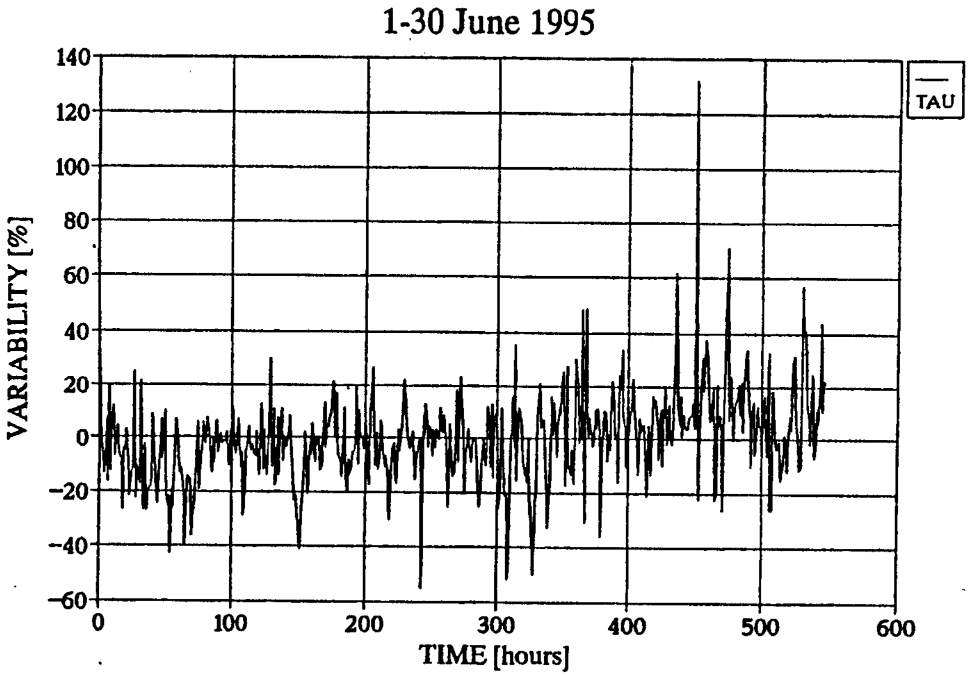

Fig. 2. Hourly values of the variability of τ (Slab Thickness) for June 1995

tween the TEC daily variability about the monthly mean and the f_0F2 variability. Further, diurnal, seasonal and response to magnetic activity effects on such correlation have to be assessed.

2. Experimental data

The f_0F2 data were deduced from vertical ionograms taken at Rome, Italy (41.9°N, 12.5°E) using the Digisonde 256 (Soicher et al. 1995). The GPS observations were taken at Matera, Italy, a site of the International GPS Service (IGS).

The equivalent TEC from the time delay measurements was determined only for satellites at elevations larger than 30° and having a subionospheric point along the line of sight within $\pm 5°$ of the latitude and longitude of the digisonde. The 5-min observed time delays were then corrected for satellite biases using the Jet Propulsion Laboratory (JPL) table of corrections (Wilson and Mannucci 1993), converted into vertical TEC (Klobuchar 1987) and averaged to obtain hourly values.

For each month of observations, the hourly values of the variability of both the TEC and f_0F2 were determined. The variability is calculated by subtracting the montly average value from each hourly value and dividing by the monthly average value. An example showing the hourly values of the variability of f_0F2 and TEC for the period 1–30 June, 1995 is shown in Fig. 1. This period is near the minimum phase of solar cycle 22. It can be seen that there is good correlation between the variability of f_0F2 and TEC.

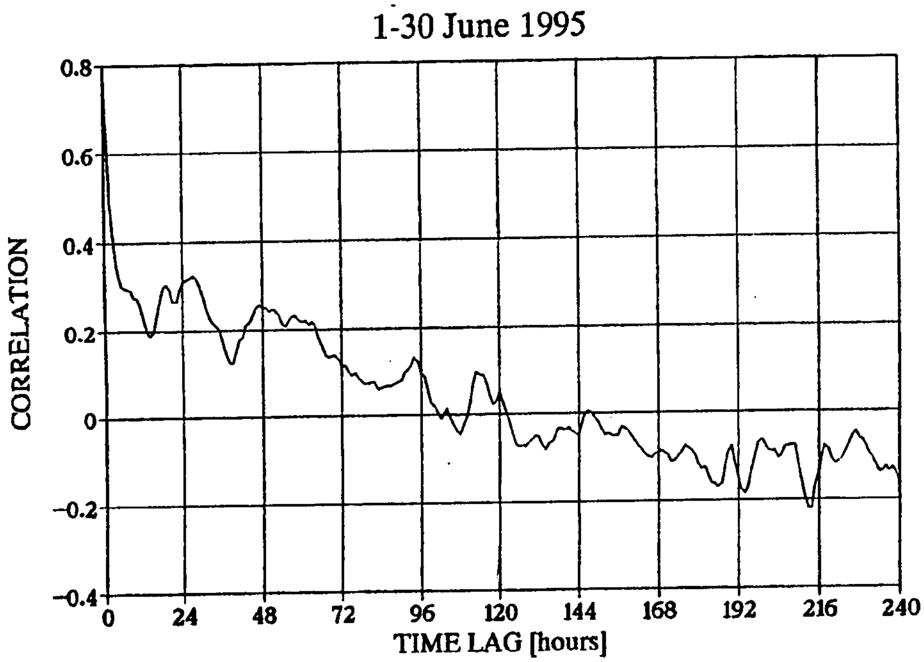

Fig. 3. Cross-correlation function of f_0F2 and TEC values of Fig. 1 (June 1995)

Another parameter of interest is the slab thickness, τ, which is proportional to the ratio TEC/$(f_o\mathrm{F2})^2$. The slab thickness can be calculated for each hour of observations and its variability determined in the same way as for TEC or f_0F2. The variability in τ for the period June 1995, is shown in Fig. 2. It can be seen that the variability is of the order of the corresponding variability of TEC or f_0F2.

3. Correlation results

The results of cross-correlation analysis on the f_0F2 and TEC variabilities depicted in Fig. 1 are shown for a portion of the time in Fig. 3. A maximum cross-correlation coefficient, R, of 0.78 occurs at zero time lag, and the coefficient reduced very quickly with time lag. It is thus shown that the correlation between f_0F2 and TEC is very good. A 24-hour periodicity, at least for the first 48 hours, is observed.

It can be seen from Fig. 1 that both the variations of f_0F2 and TEC are rather noisy on an hour-to-hour basis, which may be caused by measurements and data reduction errors rather than by physical phenomena. The main reason for these errors are (1) combining measurements from various GPS satellites, each with a different orbit and bias, which introduces errors (Klobuchar et al. 1994), (2) errors introduced by converting from oblique TEC measurements to vertical values, especially at times when there are large ionospheric horizontal gradients, and (3) real-time scaling of f_0F2 data, which introduces errors. The results of smoothing the variations in TEC and f_0F2 by a 3-hour running mean are shown in Fig. 4. It

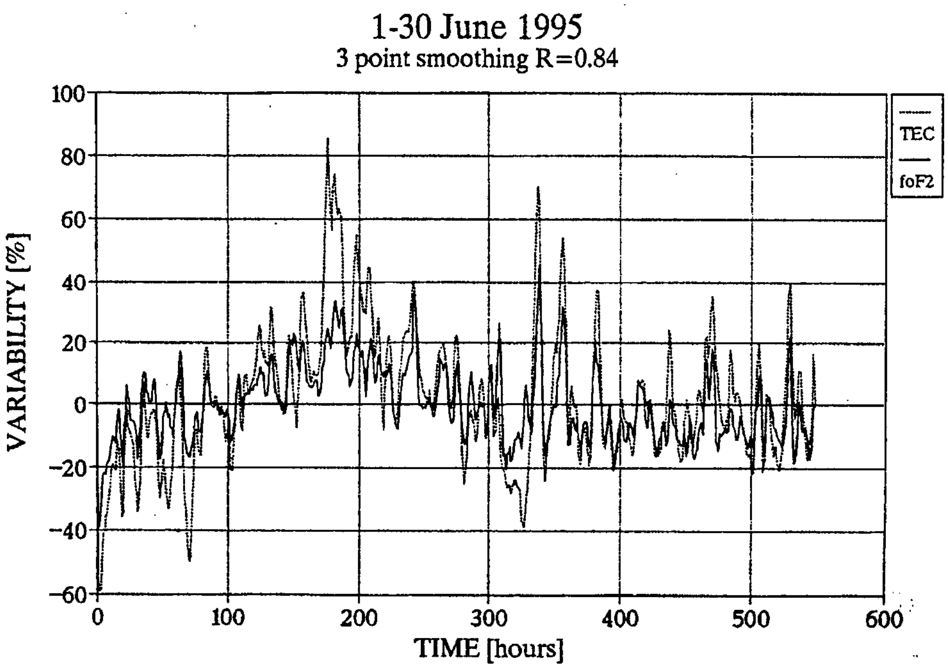

Fig. 4. Three-hour smoothing of the f_0F2 and TEC values of Fig. 1

can be seen that the correlation is improved (R of 0.84). This shows that indeed the data are noisy and that the correlation betwen TEC and f_0F2 is actually better than what the raw data indicate.

Cross-correlation results for the 12 months period, June 95 through May 96, for both the mean raw and the smoothed (3-hour running mean) are shown in Fig. 5. The overall trend is towards a $\sim$ 20% decrease in the cross-correlation coefficient, and this may reflect the corresponding decrease in sunspot numbers from 18 to 6.

The diurnal variations of the correlation coefficients for two summer periods, 1992 and 1995, are shown in Fig. 6. The 1992 period is near solar maximum phase, while the 1995 period is near the minimum phase. Each point in the figure represents correlation results for a 4-hour block (for example, the correlation at 0800 LT gives the results for the time block 0600–1000 LT). It can be seen that the diurnal behaviour is very similar for the two periods. There are minima, at about 0800 LT. A broad maximum in correlation occurs between 1200–2000 LT, with values as high as 0.85.

The similarity of the diurnal variation, especially at the predawn period minima, may be due to the minor role of plasmaspheric electron content in the correlation results. During solar maximum the plasmospheric content appears not to affect the correlation (Houminer and Soicher 1996).

The seasonal dependence of the diurnal variation of the correlation coefficient between the variability in TEC and f_0F2 is shown in Fig. 7. It can be seen that

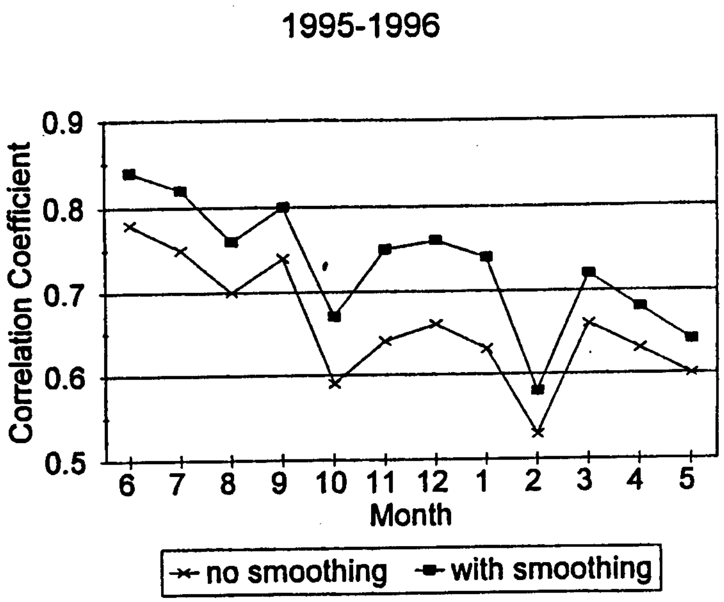

Fig. 5. Unsmoothed and smoothed mean monthly cross-correlation coefficient values of the 12-month period, June 1995 to May 1996

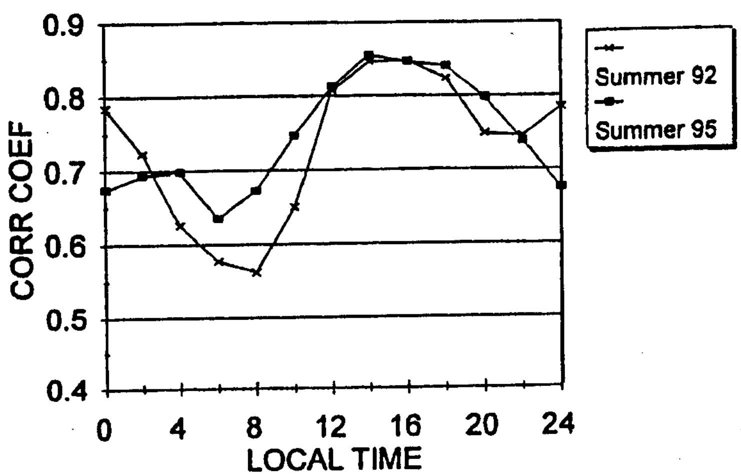

Fig. 6. Diurnal variation of the cross-correlation coefficient for f_0F2 and TEC values for the summer periods of 1992 and 1995. Each point represents correlation results for a 4-hour period

the correlation coefficient maximizes in summer, shows similar variation during the equinoxes and shows little variation during winter.

The ionosphere is known to vary substantially with geomagnetic activity. To ascertain whether magnetic activity has any impact on the cross-correlation of f_0F2

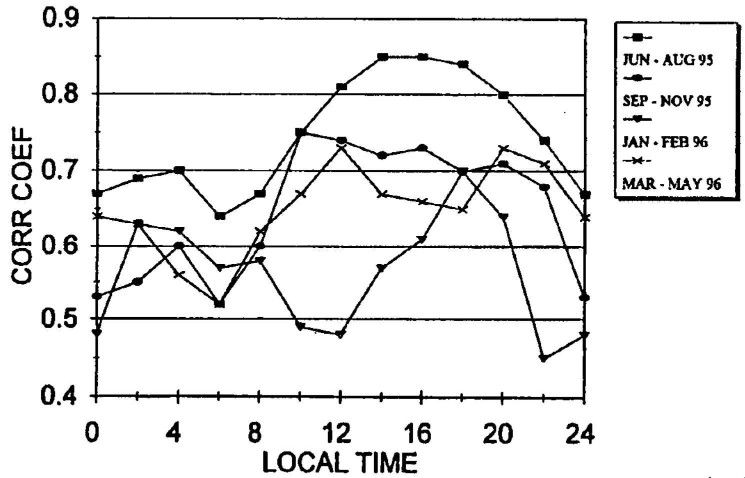

Fig. 7. Seasonal dependence of the diurnal variation of the cross-correlation coefficients for f_0F2 and TEC values. Each point represents correlation results for a 4-hour period

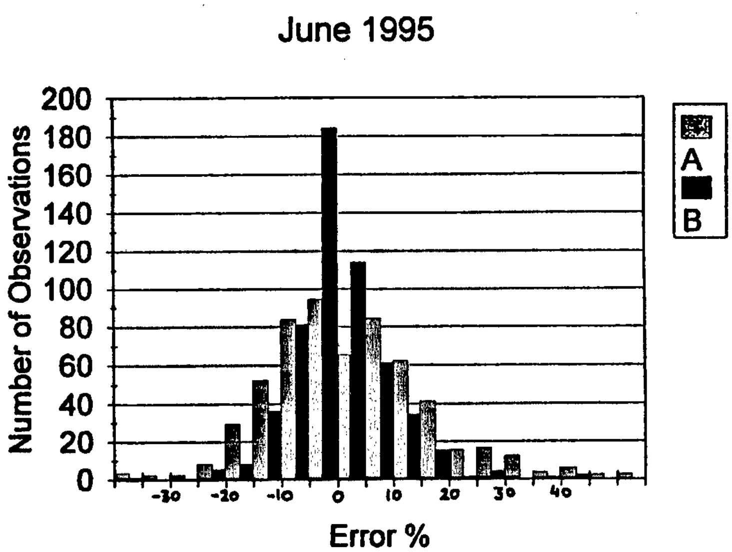

Fig. 8. Error distribution of f_0F2 calculated from TEC (dark bars) and obtained from standard model (light bars) from measured f_0F2 values (see text)

and TEC, data were compared between quiet and active periods. Table I shows selected periods with $32 < A_p < 57$ and $A_p < 8$. The correlation coefficient R for the selected period is compared with R^*, the monthly correlation coefficient containing the selected period.

It is seen that during the active periods the correlation coefficient is normally greater than that of the monthly one, whereas for quiet selected periods it is not

Table I. Cross-correlation coefficients R for selected time periods of quiet and active geomagnetic activity. R^* are the overal monthly coefficients which include the selected time periods

Dates	A_p	R	R^*
25–29 Sep 1995	41	0.80	0.74
03–08 Oct 1995	57	0.64	0.59
17–21 Oct 1995	34	0.63	0.59
18–23 Mar 1996	38	0.65	0.66
13–22 Apr 1996	32	0.74	0.63
04–15 Jun 1995	≤ 8	0.82	0.78
04–15 Jul 1995	≤ 8	0.77	0.75
25–29 Oct 1995	≤ 8	0.55	0.59
13–26 Nov 1995	≤ 8	0.58	0.64

necessarily so. The conclusion drawn is that magnetic activity affects TEC and f_0F2 in similar manner (Mendillo et al. 1972), thus maintaining high cross-correlation between the two.

The slab thickness, τ, is proportional to the ratio TEC/$(f_o\text{F2})^2$. It is expected that the variability of τ will be somewhat smaller than the variability of either the TEC or f_0F2 because of the good correlation between these two ionospheric parameters. Thus global models of the slab thickness, updated with real-time measurements of TEC obtained with the GPS network, might give improved values of f_0F2.

In order to explore this possibility, f_0F2 values for each hour were calculated using TEC obtained from the GPS time delay observations and slab thickness values from the global model of Fox et al. (1991). The error distribution for f_0F2 derived from standard prediction algorithms, and f_0F2 derived from measured TEC and the τ model are shown in Fig. 8. It is seen that the f_0F2 errors are smaller with the use of TEC measurements and the slab thickness model.

4. Conclusions

The high cross-correlation coefficient for f_0F2 and TEC in the one year data presented here raises the possibility that real-time TEC measurements may be used to update f_0F2 value determinations. The cross-correlation may even be higher if the geographic subionospheric point of TEC measurement is close to the geographic point of the f_0F2 measurement which introduces an error, in addition to the possible inherent measurement uncertainties. The correlation exhibits diurnal and seasonal variability reaching maxima during summer day and minima at all seasons during the predawn period. The data were taken near the minimum phase of the solar cycle, during which phase the plasmaspheric electron content was expected to be of the order of the ionospheric content at predawn periods and thus affect the correlation.

The fact that the correlation during the maximum phase (Houminer and Soicher 1996) is not markedly different from the correlation at minimum phase presented here, indicates that the plasmaspheric content does not impact the correlation in a significant way. The cross-correlation is high during magnetically active periods indicating that f_0F2 and TEC behave similarly in response to geomagnetic activity.

Global GPS Constellation can provide instantaneous time-delay, or TEC, values which could provide an instantaneous updating of f_0F2 models on a global basis as well as on a regional basis. The GPS signals are passive in nature to the user and, as such, do not burden the electromagnetic spectrum.

References

Fox M W, Mendillo M, Klobuchar J A 1991: *Radio Sci.*, 26, 429–438.

Houminer Z, Soicher H 1996: *Radio Sci.*, 31, 1099–1108.

Klobuchar J A 1987: Ionospheric time-delay algorithm for single frequency GPS users. IEEE Trans. Aerosp. Electron. Syst., AES-23, 325–331.

Klobuchar J A, Doherty P H, Bailey G J, Davies K 1994: In: Proceedings International Beacon Satellite Symposium, L Kersley ed., Univ. of Wales, Aberystwyth, 1–4.

Mendillo M, Papagianis M D, Klobuchar J A 1972: *J. Geoph. Res.*, 77, 4891.

Soicher H, Gorman F J, Tsedilna E F, Weitsman O V 1995: *Radio Sci.*, 30, 755–764.

Wilson B D, Mannucci A J 1993: Instrumental biases in ionospheric measurements derived from GPS data. Paper presented at ION GPS-93, Inst. of Navig., Salt Lake City, Utah

Acta Geod. Geoph. Hung., Vol. 33(1), pp. 121–128 (1998)

DETECTION OF IRREGULARITIES IN THE TOTAL ELECTRON CONTENT USING GPS MEASUREMENTS — APPLICATION TO A MID-LATITUDE STATION

R WARNANT[1]

The paper presents a very simple method allowing to detect automatically medium-scale travelling ionospheric disturbances and scintillation effects by observing the high frequency changes in the so-called geometry-free combination of GPS phase measurements. The method has been applied to the GPS measurements gathered at Brussels (mid-latitude European station) during more than 8 years: only a few scintillations were detected during this period but TIDs were very regularly observed. For this reason, we have computed statistics concerning the occurrence of TIDs. The results obtained are in good agreement with the conclusions of other independent studies.

Keywords: GPS; ionosphere; scintillation; TEC; TID; total electron content; travelling ionospheric disturbances

1. Introduction

Since a long time ago, the Global Positioning System has proved its usefulness for the study of the ionosphere. Indeed, GPS dual frequency measurements can be combined in order to compute the total electron content (Lanyi and Roth 1988, Warnant 1996). For example, the total electron content can be obtained by forming the so-called *geometry-free combination* $\Phi^i_{p,GF}$:

$$\Phi^i_{p,GF}(t_k) = \Phi^i_{p,L1}(t_k) - \frac{f_{L1}}{f_{L2}}\Phi^i_{p,L2}(t_k) \tag{1}$$

with

$\Phi^i_{p,L1}$, $\Phi^i_{p,L2}$ the $L1$, $L2$ carrier phase measurements made by receiver p on satellite i;

f_{L1}, f_{L2} the frequency of the $L1$, $L2$ carriers;

t_k epoch at which the measurement is made.

Equation (1) can be rewritten in function of the total electron content, TEC^i_p:

$$\Phi^i_{p,GF}(t_k) = -5.52 \cdot 10^{-17}\mathrm{TEC}^i_p(t_k) + N^i_{p,GF} \tag{2}$$

with

TEC^i_p the slant TEC measured along the path going from satellite i to receiver p;

$N^i_{P,GF}$ a real ambiguity.

[1]Royal Observatory of Belgium, Avenue Circulaire 3, B–1180 Brussels, Belgium, e-mail: R.Warnant@oma.be

In particular, it can be seen from Eq. (2) that the geometry-free combination also allows to monitor the evolution of the TEC in function of time, $\Delta\mathrm{TEC}_p^i(t_k)$:

$$\Delta\mathrm{TEC}_p^i(t_k) = 9.524 \cdot 10^{16} \frac{(\Phi_{p,GF}^i(t_k) - \Phi_{p,GF}^i(t_{k-1}))}{(t_k - t_{k-1})} \tag{3}$$

where $\Delta\mathrm{TEC}_p^i(t_k)$ is defined as:

$$\Delta\mathrm{TEC}_p^i(t_k) = \frac{\mathrm{TEC}_p^i(t_k) - \mathrm{TEC}_p^i(t_{k-1})}{(t_k - t_{k-1})}. \tag{4}$$

It is important to stress that the computation of $\Delta\mathrm{TEC}_p^i(t_k)$ does not require the estimation of the real ambiguity, $N_{p,GF}^i$, as long as no cycle slip occurs.

The TEC variations in function of the time can be divided in 2 classes:

— the regular gradients: the usual gradients observed in the TEC; for example, the TEC has a minimum value during the night and reaches its maximum around 1400 (local time). Consequently, there is a gradient depending on local time;

— the irregular gradients: gradients due to irregular ionospheric phenomena such as travelling ionospheric disturbances and scintillation effects.

Travelling ionospheric disturbances (or TIDs) appear as waves in the electron density (and consequently in the TEC) due to interactions between the neutral atmosphere and the ionosphere. They have a wavelength ranging from a few tens of kilometers to more than thousand kilometers. Their occurrence often cause important gradients in the TEC even on short distances. Scintillation effects are variations in phase and amplitude of a radio signal passing through small scale irregularities in the ionosphere. Scintillation effects are very often observed in the polar and equatorial regions and are sometimes detected in the mid-latitude regions.

In this paper, we present a method allowing to detect medium-scale travelling ionospheric disturbances (MSTIDs) and scintillation effects using GPS measurements. MSTIDs have horizontal wavelengths of several hundreds of kilometres, periods ranging from about 12 minutes to about 1 hour and horizontal phase speeds ranging from 100 to 300 m/s (Van Velthoven 1990).

2. The method

Travelling ionospheric disturbances and scintillation effects cause high frequency changes in the TEC. Consequently, these phenomena can be studied by detecting such changes in $\Delta\mathrm{TEC}_p^i$.

In order to do that, we filter out the low frequency changes in the TEC by modelling $\Delta\mathrm{TEC}_p^i$ using a low order polynomial. The residuals R_I of this adjustment (i.e. $\Delta\mathrm{TEC}_p^i$ - polynomial) contain the high frequency terms. In a similar way

Table I. Definition of the ionospheric variability

V_I	σ_{R_I} (TECU/min)
0	$0.00 \leq \sigma_{R_I} < 0.08$
1	$0.08 \leq \sigma_{R_I} < 0.10$
2	$0.10 \leq \sigma_{R_I} < 0.15$
...	...
8	$0.40 \leq \sigma_{R_I} < 0.45$
9	$\sigma_{R_I} \geq 0.45$

as Wanninger (1994), we define the ionospheric variability, V_I, using the standard deviation of the residuals R_I (Table I):

$$V_I = 0 \quad \text{when} \quad 0.00 \leq \sigma_{R_I} < 0.08 \text{TECU/min}$$

$$V_I = 1 \quad \text{when} \quad 0.08 \leq \sigma_{R_I} < 0.10 \text{TECU/min}.$$

In practice, the ionospheric variability is computed for every observed satellite, using periods of 15 minutes of measurements. When V_I is different from zero, we decide that an "event" is detected. Such an "event" is presented in Fig. 1. This figure displays the TEC gradients, Δ TEC, observed at Brussels on May 28, 1993. These gradients are caused by scintillations effects. Figure 2 shows the gradients observed in 3 GPS permanent stations operated by the Royal Observatory of Belgium. These effects are due to a (medium-scale) travelling ionospheric Disturbance. In fact, most of the "events" detected in Belgium are due to TIDs.

With a sampling interval of 30 seconds, 24 hours of GPS measurements in the RINEX format are stored in a file of which the size is ranging from 1.5 Mb to more than 2 Mb. To perform any long term study based on GPS measurements, it is thus indispensable to develop automatic data processing procedures. In particular, it is not realistic to imagine that an operator could screen the residuals to decide

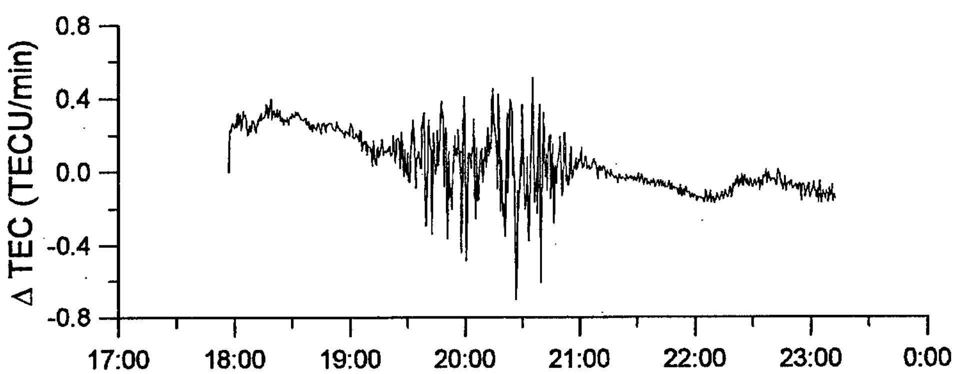

Fig. 1. Scintillations observed at Brussels on May 28 1993

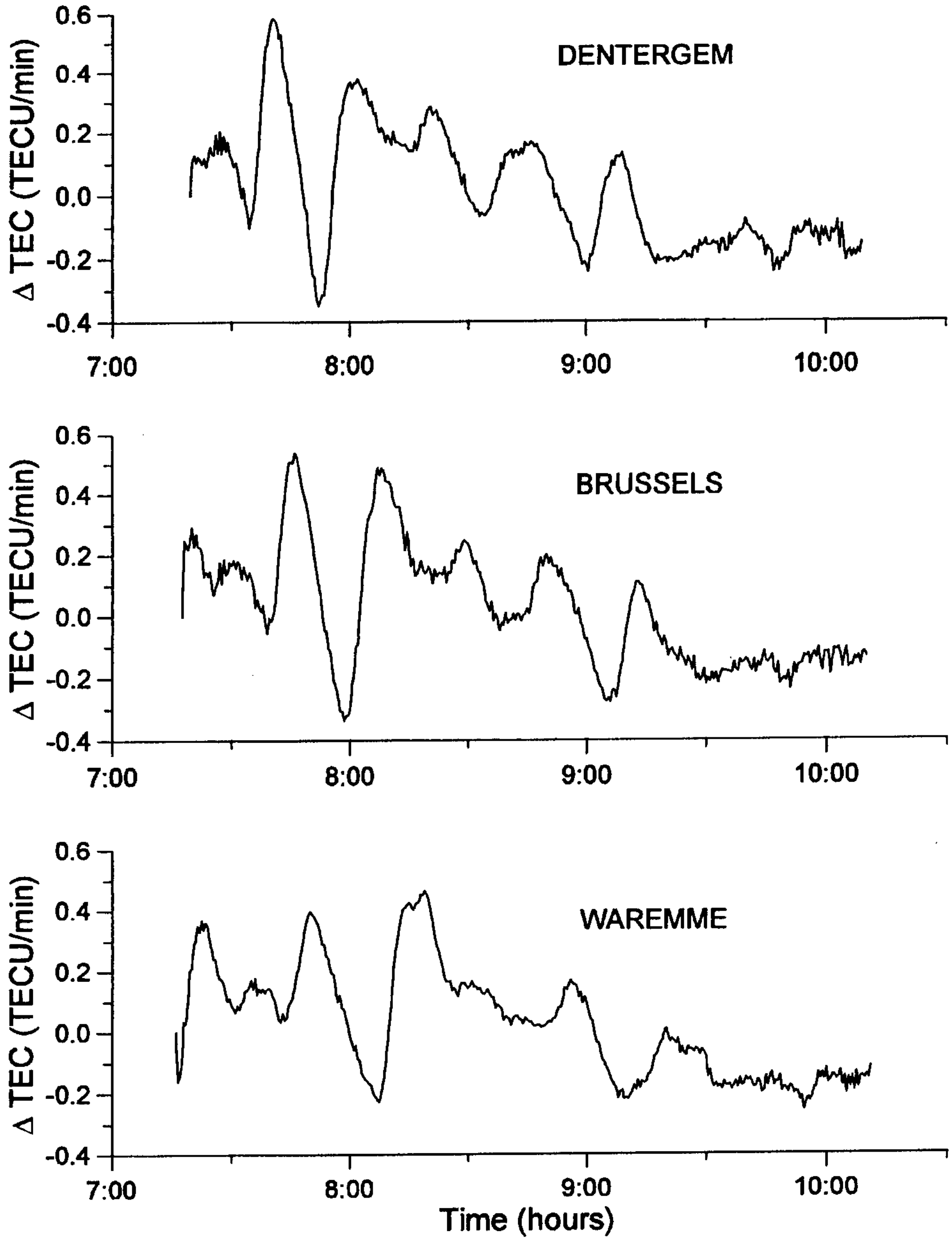

Fig. 2. TEC gradients due to a TID observed on October 30, 1994 in 3 Belgian stations

"manually" if a TID is present or not. For this reason, we must choose threshold values which will be used by the computer to take an automatic decision. The choice of 0.08 TECU/min as threshold value to decide if an event is taken into account comes from the fact that the multipath also gives rise to high frequency changes in the geometry-free combination. This site-dependent effect can reach several centimetres on phase measurements and has periods ranging from a few minutes to several hours depending on the distance separating the reflecting surface from the observing antenna (if this distance is shorter, the period is longer). The multipath effect being more frequent at low elevation, we have chosen an elevation mask of 20°. In the case of the Belgian permanent GPS network, a threshold value of 0.08 TECU/min is large enough to avoid to interpret multipath effects as ionospheric phenomena. This value should be valid for most of the GPS sites but should be applied with care in locations where the multipath is particularly important. An additional verification is then performed: the comparison of the ionospheric variability observed in neighbouring GPS stations allows also to distinguish between multipath and ionospheric phenomena: indeed, large residuals observed at the same time in different stations cannot be due to multipath.

Two other error sources can affect our method: cycles slips and phase surges. Cycle slips are jumps of an integer number of cycles which occur when the receiver loses lock on the satellite signal. In an automated data processing procedure, an uncorrected cycle slip could result in a σ_{R_I} above the threshold value even if no ionospheric perturbation is present.

Phase surges give rise to several successive jumps in the GPS phase measurements. These jumps are not integer numbers of cycles. For this reason, this error is much more difficult to detect. In addition, this effect is related to the receiver-to-satellite geometry: it means that a similar effect can be observed in several neighbouring GPS stations at the same time (Sleewaegen 1997). Nevertheless, these jumps can be identified because their period is always shorter (a few minutes) than the periods of ionospheric disturbances.

The choice of 15 minute periods to compute the ionospheric variability is due to the fact that most of the MSTIDs have periods ranging from 5 to 30 minutes. If we choose a too short period, the TID will not have the time to cause TEC changes large enough to be detected. On the other hand, if the period is too long, the large residuals in $\Delta\mathrm{TEC}_p^i$ due to the TID will be lost among the other residuals and the resulting σ_{R_I} will remain under the threshold of 0.08 TECU/min.

3. Results

The procedure outlined here above has been applied to a data set covering a period of more than 8 years: since May 89, GPS measurements have been regularly performed at Brussels. Since April 1993, the measurements are continuous. Three additional permanent stations are in operation since January 94 (Dentergem, Dourbes and Waremme); 3 new stations (Bree, Meeuwen and Membach) have been installed in 1997 (Fig. 3).

This experiment has allowed us to compute statistics concerning the occurrence

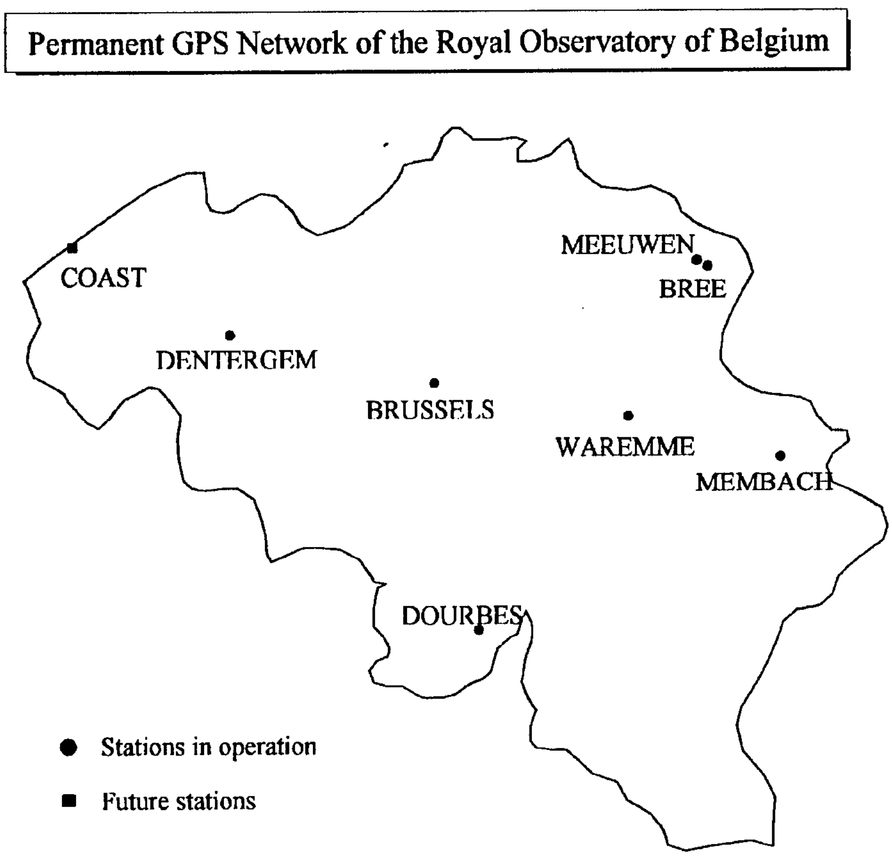

Fig. 3. The permanent GPS network of the Royal Observatory of Belgium

of TIDs above Belgium (i.e in a mid-latitude European station) and to answer the following questions: are TIDs unusual phenomena, do they appear during specific periods in the day, in the year, in the solar cycle, ... ? Figure 4 shows the statistics of the observed TIDs for two month: January 1994 and January 1997. This figure displays the number of TIDs encountered during these month in function of the time in the day. It means that a sum of all events occurring at a specific time (for example between 1000 and 1100) during a whole month is made.

Figure 5 shows the number of events (TIDs) detected from April 93 to May 97 as a function of the local time. The different levels of grey represent the number of events detected. By looking at this figure, several conclusions can be drawn concerning the number of detected TIDs:

— there is a main maximum between 1000 and 1600 (local time) during the winter;

— there is a secondary maximum during the night;

— it decreases with decreasing solar activity.

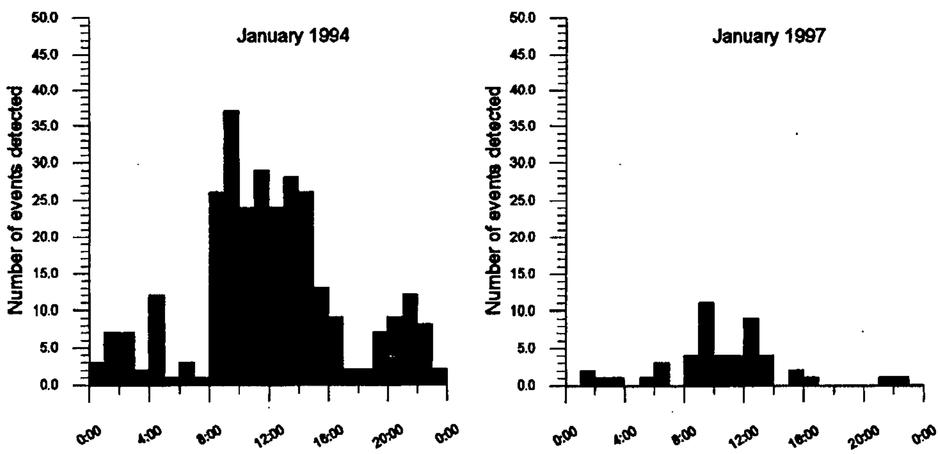

Fig. 4. Number of events detected as a function of local time in January 94 and January 97

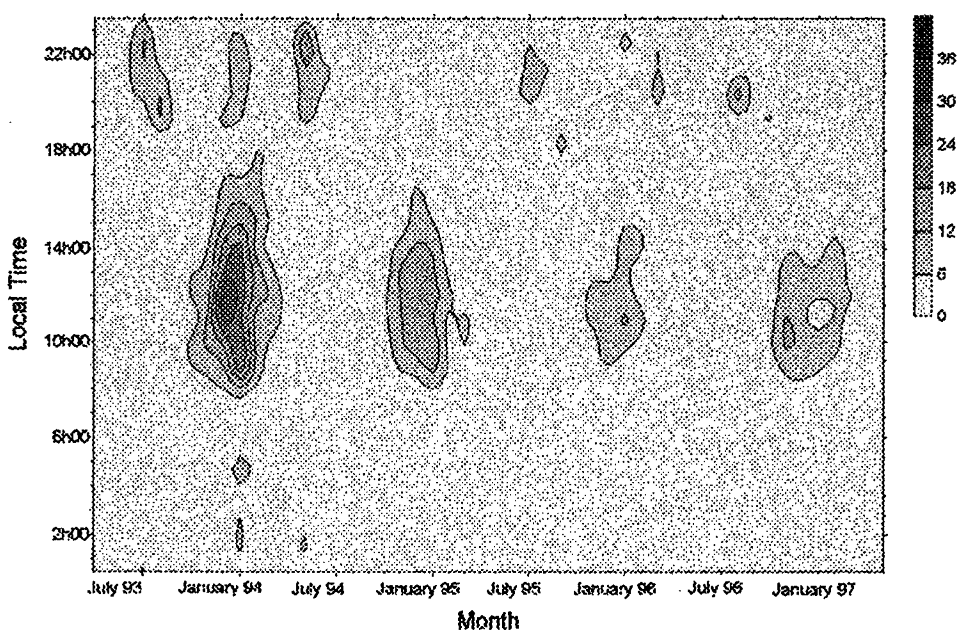

Fig. 5. Number of TIDs detected from April 93 to May 97 as a function of local time

The case of scintillation effects is different: only a few "events" are observed in one year. These results confirm the conclusions of previous studies performed by means of other independent techniques (see for example, Van Velthoven 1990).

4. Conclusion

The paper has presented a very simple method allowing to detect medium-scale travelling ionospheric disturbances and scintillation effects using the geometry-free combination of GPS carrier phase measurements. This method has been applied to the GPS measurements gathered in the Belgian GPS network since 1989. This experiment has allowed to compute statistics concerning the occurrence of TIDs and scintillations above Belgium. The results which are in good agreement with previous independent studies show that TIDs are very common phenomena at Brussels but only a few scintillation effects have been detected.

References

Lanyi G E, Roth T 1988: *Radio Science*, 23, 483–492.

Sleewaegen J M 1997: Personal communication, Royal Observatory of Belgium

Van Velthoven P J 1990: Medium-scale irregularities in the ionospheric electron content. Ph.D. Thesis, Technische Universiteit Eindhoven

Wanninger L 1994: Der Einfluß der Ionosphäre auf die Positionierung mit GPS. Ph.D. Thesis, Wissenschaftliche Arbeiten der Fachrichtung Vermessungswesen der Universität Hannover, Nr. 201

Warnant R 1996: Etude du comportement du Contenu Electronique Total et de ses irrégularités dans une station de latitude moyenne. Application aux calculs de positions relatives par le GPS. Ph.D. Thesis (in French), Série Géophysique (No. Hors-Série) de l'Observatoire Royal de Belgique, Bruxelles

Acta Geod. Geoph. Hung., Vol. 33(1), pp. 129–135 (1998)

COMMENTS ON PROTONOSPHERIC CONTENT — ATS-6 REVISITED

J K HARGREAVES[1]

The application of GPS observations to the determination of electron content has renewed interest in the question of how the electron content is distributed between the closer and more distant sections of the propagation path.

The ATS-6 radio beacon experiment of the mid-1970s enabled the electron content to be determined from both the modulation phase technique (which included the whole path out to 6.6 Re) and the Faraday effect (which gave an electron content biased towards the lower altitudes). The observations were also simulated using a mathematical model. Thus it was possible to consider the significance of the "protonospheric content" as the difference between the phase and the Faraday contents was usually known.

The paper presents results from those studies in the context of GPS work. It is shown that at certain times a significant fraction of the total content resides at high altitudes, and that if this is not taken into account significant errors can arise in the determination of the electron content.

Keywords: ATS-6; Faraday effect; GPS; protonosphere

1. Introduction

Since the GPS satellites are viewed over a range of zenith angles, it is usual to convert the electron content observed along a slant path to an equivalent vertical content so that the observations at different angles may be compared and converted to maps. The variation of electron content with the zenith angle is also used to determine the baseline of the measurement, which is uncertain due to the "bias" in each satellite transmitter. Since the zenith angle of the received ray depends on altitude (Fig. 1), the conversion to vertical requires that an effective height is assumed. The value of this effective height obviously depends on the distribution of ionization along the ray path.

2. The ATS-6 experiment

The only sustained experiment able to effect a separation between the ionospheric and protonospheric parts of the path was the radio beacon experiment on the geosynchronous satellite ATS-6 (Davies et al. 1972). Here, the term "ionosphere" is used for that part due to heavy ions, and the "protonosphere" is that due to protons. ATS-6 was launched in 1974, and was observed from several points on the Earth's surface over a period of several years, the satellite being located at three different longitudes at different times.

[1]Engineering Dept., University of Lancaster, England (also at Physics and Astronomy Dept., University of Central Lancashire, Preston, England

1217-8977/98/$ 5.00

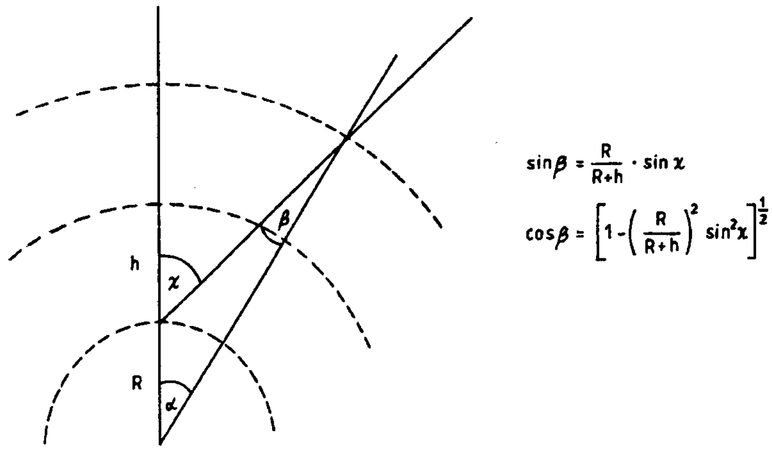

Fig. 1. Dependence with height of the zenith angle of an oblique ray. The correction factor from oblique to vertical electron content is $\cos\beta$

The ATS-6 beacon experiment measured the electron content by its effect on modulation phase — giving the total content over the whole path — and also by the Faraday effect — the rotation of the plane of polarization — which gives an electron content weighted by the geomagnetic field strength and therefore biased towards the lower (i.e. ionospheric) altitudes.

At Lancaster, England, observations were made for rather less than a year in 1975–1976, though both solstices and both equinoxes were included. It was a time of low sunspot numbers. Including data from an ionosonde (at Dourbes), three independent measurements were obtained, and these were combined to give three measured quantities:

— electron content (from the phase effect);

— slab thickness (electron content $/N_{\max}$, $N_{\max}$ being the maximum electron density of the layer from the ionosonde);

— and an "F-factor" derived from the ratio between the Faraday and phase effects.

Slab thickness was already a well established parameter, having been used for many years to quantify the thickness of the ionospheric layer: but F-factor was a new parameter, not previously available, which depended on the distribution of ionization between higher and lower levels and so represented the "average height" of the ionization. This was, of course, the reason for including the Faraday measurement on the beacon in the first place.

3. Data

Three parameters are still not very many, and a useful step in interpreting the data is to divide the electron content into two parts:

$$N_T = N_F + N_P\,, \tag{1}$$

where N_T is the total electron content measured from the modulation phase, and N_F is the electron content derived from the Faraday effect, proportional to

$$\int N f_L dl = \overline{f}_L \int N dl\,, \tag{2}$$

where f_L is the longitudinal component of the gyrofrequency and $\overline{f}_L$ is a selected "mean" value. $\overline{f}_L$ was taken as the value of f_L at height 380 km, and was 0.83 MHz for the Lancaster-to-ATS-6 raypath. This interpretation attributes all the Faraday effect to the lower region, and the remainder ($N_T - N_F = N_P$) is assumed to make no contribution to the polarization rotation. This part is commonly called the "protonospheric content", though that is not strictly the case and for this reason "residual content" may be a better term. Obviously, the value of $\overline{f}_L$ selected affects the value of N_P obtained.

F is measured from the ratio between the polarization and phase effects. It is that value of longitudinal gyrofrequency which gives the observed Faraday effect from the observed electron content (Davies et al. 1975). Hence,

$$\overline{f}_L N_F = F N_T\,, \tag{3}$$

$$N_P = N_T(1 - F/\overline{f}_L)\,, \tag{4}$$

$$N_P/N_T = 1 - F/\overline{f}_L\,. \tag{5}$$

In these equations N_T and F are determined from the data, $\overline{f}_L$ is assumed, and thus N_P and N_P/N_T may be obtained.

4. Modelling

To help to intepret the measurements in physical terms a programme of mathematical modelling was undertaken which included electron production, recombination, transport, the effect of thermospheric wind, and (in some cases) the conjugate hemisphere (Poulter et al. 1981, Sethia et al. 1985). One major question was the significance of the residual (or protonospheric) content. The model was set up for equinox conditions and the values of N_T, slab thickness, and F predicted from it were compared with the corresponding values observed in March 1976. The model was then used to see how much of the electron content resided above certain heights, and this was compared with the value of N_P, also from the model. It was found that for the raypath from Lancaster to ATS-6 N_P corresponded with the electron content above 2600 km, the same value applying throughout the 24 hours.

(The total slant content of H^+ was also calculated, which showed that N_P is about 0.6 to 0.7 of the slant H^+ content (depending on the time of day). Therefore 0.4 to 0.3 of the actual protonospheric content lies below 2600 Km, and this appears in the so-called ionospheric content N_F as measured in the experiment.

5. Measurements

Whether or not this matters in practice depends, of course, on the magnitude of the ratio N_P/N_T. Should that ratio be very small then the protonospheric contribution would be of little consequence anyway. Figure 2 shows the values of N_T, N_P/N_T and N_P for summer, winter and the equinoxes measured at Lancaster in 1975–1976. We note that N_P/N_T varies in antiphase with N_T during the day, leading to relatively small changes of N_P during the day. N_T varies considerably with the season, but the seasonal variation of N_P is smaller.

To emphasise the possible effect of the protonospheric content we consider the winter night, when N_P/N_T is at its largest. Then half the total content is in the protonosphere (i.e. above 2600 km). At other times of day and in other seasons the protonosphere holds a smaller fraction of the total, but it is still a significant fraction.

6. Equivalent vertical content

These were slant measurements, the elevation at the ground being 21° (zenith angle 69°). With reference to Fig. 1, the angle between the ray path and the vertical at height h is related to the zenith angle at the ground by

$$\cos\beta = [1 - (R/(R+h))^2 \sin^2\chi]^{1/2} . \tag{6}$$

R being the radius of the earth, $\cos\beta$ is the factor required to convert slant to vertical content at height h. Sample values are given in Table I for various h and χ. In brackets is given the ratio between the correction at h to the correction at 400 km, a typical "ionospheric" height. For example, if $\chi = 45°$ then content at 1 Re would be overcorrected by 25% if the factor for 400 km were used.

Taking $\chi = 69°$ and the values of N_F and N_P for winter night (each $5\cdot10^{16}$ m^{-2}), the first (assuming 400 km) is equivalent to $2.4\cdot10^{16}$ vertical and the second (assuming 2600 km) to $3.75\cdot10^{16}$. For the vertical content, therefore, we get $N_P/N_T = 0.61$. The protonospheric content is a larger fraction of the vertical total content than of the slant content.

7. Effect of a protonosphere on the determination of electron content using the obliquity of the ray in GPS measurements

Consider the electron content to be in two parts of the total vertical content I, a fraction P is in the protonosphere at height h_P and fraction $(1-P)$ is in the ionosphere at height h_i, see Fig. 3. The zenith angle at the ground is χ. The ionospheric content gives a slant contribution $(1-P)I/\cos\beta_i$, and the protonosphere contributes $PI/\cos\beta_P$, where β_i and β_P are the zenith angles for the ionosphere (height h_i) and protonosphere (height h_P). The total slant content is therefore $(1-P)I/\cos\beta_i + PI/\cos\beta_P$.

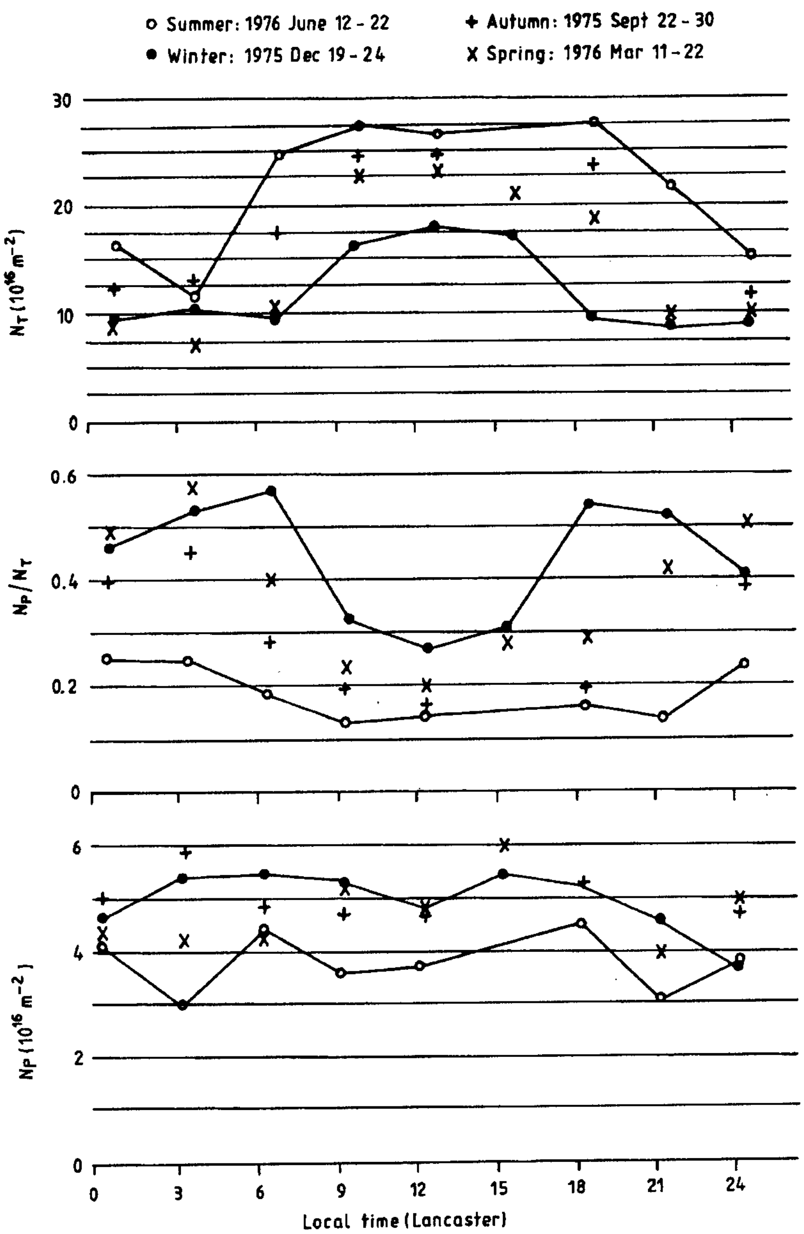

Fig. 2. Total (N_T) and residual (N_P) electron contents determined in the ATS beacon experiment, 1975–1976

Allowing for a bias B, which depends on transmitter and receiver hardware only, the electron content reading in the zenith is

$$R_0 = I + B \tag{7}$$

Table I. Values of the correction factor $\cos\beta$ as a function of layer height h and ground zenith angle χ

	$\cos\beta$ $(\cos\beta/\cos\beta_{400})$						
	h (km)	0	400	2000	2600	1 Re	2 Re
	$\left(\frac{R}{R+h}\right)^2$	1.0	0.885	0.579	0.504	0.250	0.111
χ°	$\sin^2\chi$						
15	0.0670	0.933	0.970 (1.0)	0.980 (1.01)	0.983 (1.01)	0.992 (1.02)	0.996 (1.03)
30	0.250	0.866	0.882 (1.0)	0.925 (1.05)	0.935 (1.06)	0.968 (1.10)	0.986 (1.12)
45	0.500	0.707	0.747 (1.0)	0.843 (1.13)	0.865 (1.16)	0.935 (1.25)	0.972 (1.30)
60	0.750	0.500	0.580 (1.0)	0.752 (1.30)	0.789 (1.36)	0.901 (1.55)	0.957 (1.65)
69	0.872	0.358	0.478 (1.0)	0.704 (1.47)	0.749 (1.57)	0.884 (1.85)	0.950 (1.99)

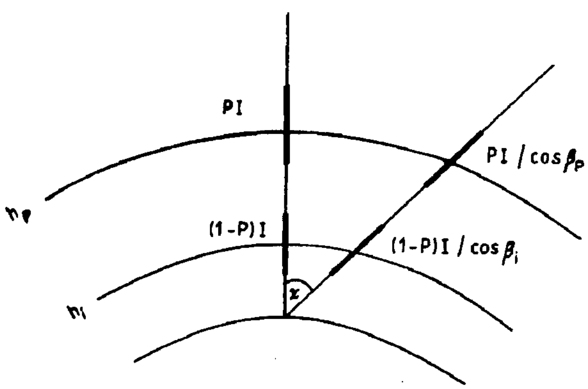

Fig. 3. A model of the electron content divided into discrete ionospheric and protonospheric parts

and at angle χ it is

$$\begin{aligned} R_\chi &= (1-P)I/\cos\beta_i + PI/\cos\beta_p + B \\ &= I\sec\beta_i + IP(\sec\beta_P - \sec\beta_i) + B\,. \end{aligned} \tag{8}$$

If it is assumed that all the ionization is in the ionosphere ($P = 0$),

$$R_\chi = I\sec\beta_i + B\,. \tag{9}$$

It is now possible to find both I and B. From (7) and (9),

$$I = (R_\chi - R_0)/(\sec\beta_i - 1)\,, \tag{10}$$

and

$$B = (R_0\sec\beta_i - R_\chi)/(\sec\beta_i - 1)\,. \tag{11}$$

But if the protonospheric content is significant, we get

$$I = \frac{(R_\chi - R_0)}{\sec\beta_i + P(\sec\beta_P - \sec\beta_i) - 1} \tag{12}$$

$$B = \frac{R_0[\sec\beta_i + P(\sec\beta_P - \sec\beta_i)] - R_\chi}{\sec\beta_i + P(\sec\beta_P - \sec\beta_i) - 1}. \tag{13}$$

If we neglect P, and derive the electron content from Eq. (10) when P is not actually negligible, the ratio between the estimated (I_E) and correct (I_C) electron content is (from Eqs 10 and 12),

$$\frac{I_E}{I_C} = \frac{\sec\beta_i + P(\sec\beta_P - \sec\beta_i) - 1}{\sec\beta_i - 1} = 1 + \frac{P(\sec\beta_P - \sec\beta_i)}{\sec\beta_i - 1}. \tag{14}$$

Since the second term is negative, the estimate is always to small. Note that the relative error is proportional to P.

Putting in sample values,

$$\chi = 45°,\ h_i = 400 \text{ km},\ h_P = 2600 \text{ km},$$
$$(\sec\beta_P - \sec\beta_i) = -0.1825,$$
$$\text{and } (\sec\beta_i - 1) = 0.3386.$$

Therefore the relative error is $-0.539P$.

Taking values of P from the ATS-6 results:

	P	% error
Worst case (winter and equinox night)	0.5	27
Best case (summer day)	0.15	10
Intermediate (winter day)	0.25	13

The error is reduced, but only slightly, by taking a smaller value of χ. The error in the electron content goes into the bias term (B).

8. Conclusions

At certain times a large fraction of the total electron content resides in the protonosphere at heights above 2600 km and well above the level of the heavy-ion ionosphere. This creates a difficulty in GPS-based measurements which depend on comparing observations made at different zenith angles to determine the baseline of the measurements (due to instrumental bias) and thereby obtain absolute results. If the protonospheric content is neglected, errors in the range 10 to 30% are possible.

References

Davies K, Fritz R B, Grubb R N 1972: *The Journal of Environmental Sciences*, 15, 31.
Davies K, Fritz R B, Grubb R N, Jones J E 1975: *Radio Science*, 10, 785.
Poulter E M, Hargreaves J K, Bailey G J, Moffett R J 1981: *Planet. Space Sci.*, 29, 869.
Sethia G C, Bailey G J, Moffett R J, Hargreaves J K 1985: *Planet. Space Sci.*, 33, 321.

Acta Geod. Geoph. Hung., Vol. 33(1), pp. 137–146 (1998)

PROTONOSPHERIC ELECTRON CONTENTS FROM GPS/NNSS OBSERVATIONS

N LUNT[1], L KERSLEY[1], G BISHOP[2], A MAZZELLA[2]

Transmissions from GPS and NNSS satellites have been used to determine the vertical total electron content (TEC) for observations made in the UK during June, November and December 1996. Differences between the TEC values obtained using GPS and NNSS arise from the influence of protonospheric electrons on the GPS signals. The GPS vertical TEC values were found to be greater than those calculated from NNSS, the difference representing the contribution from electrons in the high plasmasphere. The differences between the vertical electron content measurements vary on a diurnal basis, though no clear pattern has emerged from the limited sample of observations. The differences are larger for ray paths to the south than those to the north of the station with the magnitudes in the winter months being greater than those for summer.

Keywords: GPS; NNSS; protonosphere; TEC

1. Introduction

At some height in the ionised atmosphere, usually below about 1000 km altitude, there is a transition from an oxygen-dominated to a hydrogen-dominated plasma. The protonosphere extends from this transition height out to the plasmapause. It is often useful to treat the mid-latitude plasmasphere as consisting of winter and summer ionospheres linked by a common protonosphere that lies along the magnetic field lines joining the conjugate hemispheres. The ionospheres act as sources of plasma and the protonosphere as a reservoir. There is a field-aligned exchange of plasma between ionosphere and protonosphere on a diurnal basis, while in addition, the winter ionosphere benefits from plasma produced in the conjugate summer ionosphere (Hargreaves 1995).

Apart from the ATS-6 experiment in the 1970's, few line-of-sight electron content measurements of the protonosphere have been performed. During the European phase of the ATS-6 project, the group at Aberystwyth made line integral measurements of protonospheric contents by differencing group delay and Faraday rotation observations of signals from the ATS-6 satellite for about 9 months in 1975/1976. The measurements were made at a time near solar minimum and it was found that the slant protonospheric electron contents measured from Aberystwyth were usually in the range of $3\cdot10^{16}$ m^{-2} to $5\cdot10^{16}$ m^{-2} (Kersley and Klobuchar 1978). There was some evidence for a diurnal variation, but the most marked changes were found in the response to geomagnetic storms, where a rapid depletion of the protonospheric flux tubes around 1800 local time on the first day of the storm was followed by a slow recovery extending over some two weeks (Kersley and Klobuchar 1980).

[1]Department of Physics, University of Wales, Aberystwyth, SY23 3BZ, UK, Fax: +44 1970 622826, e-mail: nil95@aber.ac.uk
[2]USAF Phillips Laboratory, Hanscom AFB, MA 01731, USA

2. Experiment

The satellites used in the present study are from the Navy Navigation Satellite System (NNSS) and the Global Positioning System (GPS). The NNSS satellites are in circular polar orbits at an altitude of approximately 1100 km, with transmissions on 150 MHz and 400 MHz. The low Earth orbit of the NNSS satellites implies that the signals only pass through the ionosphere. The GPS satellites are in circular orbits of 20200 km altitude that are inclined at 55° to the equator. The GPS signals are transmitted on 1575.4 MHz and 1227.6 MHz. The GPS satellite orbits are essentially at about the plasmapause height. The lower boundary of the protonosphere was taken in this study to be at the NNSS orbit height of 1100 km.

A preliminary campaign was conducted during 1996 to investigate the possibility of making measurements of protonospheric electron content. Observations were made at the GPS site in Aberystwyth (52.4°N, 4.1°W) and at the NNSS sites in both Aberystwyth and Hawick (55.4°N, 2.8°W). Measurements from a total of sixty-nine days were obtained during the months of June, November and December where there were simultaneous observations of both GPS and NNSS transmissions.

3. Method

From the GPS transmissions it is possible, in principle, to make absolute slant TEC measurements by observing the difference in group delay of the two signals. However in practice, these measurements have contamination due to multipath reception of the signals. In addition, the observations are biased as a consequence of the unknown time delays introduced by the transmitter on each satellite and by the receiving system. Thus, to obtain absolute values of TEC along the ray path, it is necessary to calibrate the group delay measurements. A second way of estimating the electron content from GPS signals is to determine the phase difference of the carriers received at the two frequencies. These measurements are not subject to multipath effects to the extent of the group delay determinations, so that undisturbed, though relative, slant TEC is obtained. This relative record can be fitted to the absolute group delay measurement, so that smooth, but biased, absolute TEC can be obtained. Further processing is thus needed to obtain the absolute values.

The GPS data have been calibrated using the Self Calibration Of pseudoRange Errors (SCORE) procedure. Even though each GPS satellite is only above the horizon for a few hours, there are always at least four satellites visible at any time from anywhere on Earth. SCORE uses self-consistency constraints on the measurements made by the GPS receiver to build up the diurnal behaviour of the electron content from the individual satellite passes. This is done by converting the electron content measurements from slant to equivalent vertical TEC and converting from the GPS time when the measurements were made to the Ionospheric Penetration Point (IPP) local time for each satellite. An ionospheric height of 350 km is used for calculation of the vertical TEC and the IPP local time. For calibration SCORE requires maximum agreement in ionospheric measurements at IPP local time latitude conjunctions within a defined correlation region. A more detailed description

of the SCORE process is given by Bishop et al. (1996). SCORE uses GPS data from above 35 degrees elevation. This limitation removes the worst of the multipath contamination, which occurs at low elevations, and also confines the spatial extent of the ionosphere considered. Twenty-four hours of GPS observations are used in the SCORE procedure, so each day is treated in isolation. Since no test signals are used, and as each day is processed individually, there are no concerns in the SCORE procedure about the calibrations drifting with time once a receiver has been deployed in the field. In addition, no ionospheric models are used by SCORE, so that the method can respond freely to the actual conditions in the ionosphere. With the orbits of the GPS satellites inclined at 55 degrees to the equator, the ray paths from the space vehicles intercept an ionospheric region covering several degrees of latitude in extent, with the exact coverage depending upon the latitude of the receiving station. As a consequence, SCORE can produce plots for several, one degree wide latitudinal bands in the ionosphere. It is thus possible to study latitudinal behaviour over a limited range from a single station.

Absolute values of the vertical total electron content in the ionosphere can be obtained from observations of NNSS transmissions at two stations aligned in longitude but separated by a few degrees of latitude. The calibration technique for such observations has been described by Leitinger et al. (1975). In the present work an ionospheric height of 350 km has been used for calculation of the vertical TEC. The NNSS data are the vertical ionospheric TEC values, estimated at latitudes corresponding to the centre of the one degree wide bands. The time tags of the NNSS data were converted to IPP local time.

4. Results

Figure 1 shows the GPS and NNSS vertical TEC data from day 156 (early June) 1996 for the ionosphere over Aberystwyth. The form of the GPS record is that expected for vertical TEC above Aberystwyth for June. A "bite out" around midday can be seen, which arises from the effect of the neutral wind on the ionisation and the highest electron content is in the evening. The NNSS derived TEC values are consistently below the levels determined from the GPS data. By way of a comparison, Fig. 2 shows the GPS and NNSS vertical TEC data from day 358 (December) 1996. In December, the main peak is around midday and has a lower magnitude than the daytime maximum in June. The small enhancement in the GPS vertical TEC after midnight arises as a consequence of plasma flow from the protonosphere. The discrete values of NNSS vertical TEC measurements at the times of the satellite passes are lower in the main by several TEC units than the GPS record.

For similar observing geometries it would be expected that the GPS vertical TEC, T_{GPS} should be related to the NNSS vertical TEC, T_{NNSS} in a simple manner, like Eq. (1).

$$T_{\mathrm{GPS}} = T_{\mathrm{NNSS}} + P\,. \tag{1}$$

P is a positive quantity that indicates the level of protonospheric contamination of the GPS vertical TEC measurement. Thus an estimate the protonospheric content

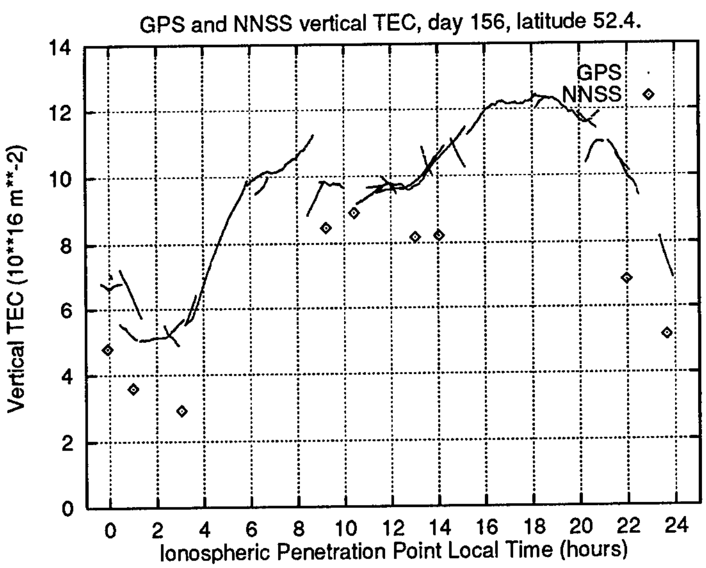

Fig. 1. GPS and NNSS vertical TEC for a day in early June 1996

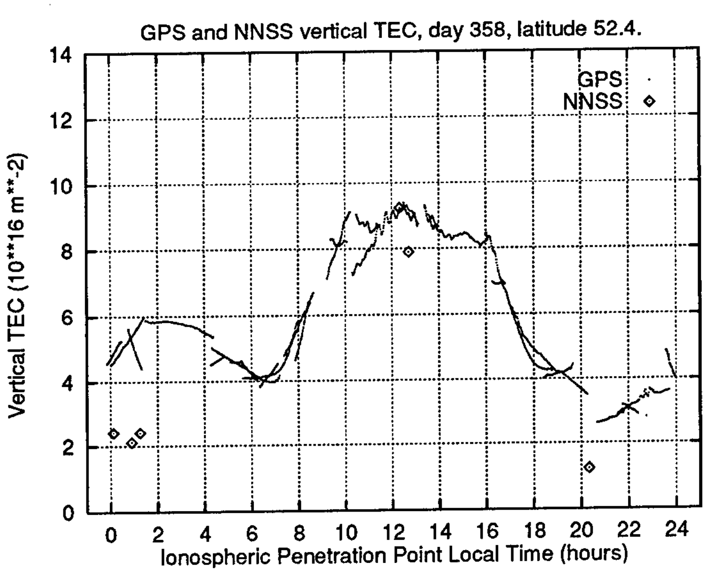

Fig. 2. GPS and NNSS vertical TEC for a day in mid-December 1996

can be attempted by differencing the GPS and NNSS data. Average GPS data were produced by averaging values from each latitude band for one hour periods of the IPP local time. The difference between the average GPS vertical TECs and any NNSS vertical TEC values that fell within the appropriate period were taken. When

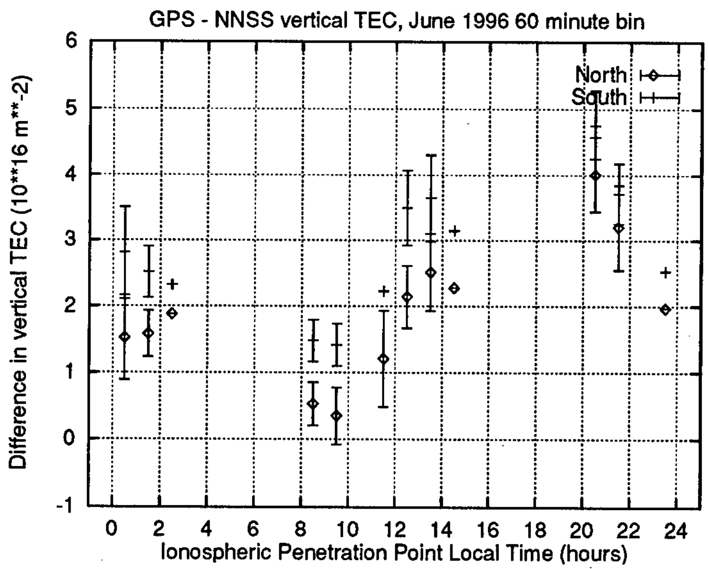

Fig. 3. Hourly average GPS minus NNSS vertical TEC for the 21 days of data available in June 1996

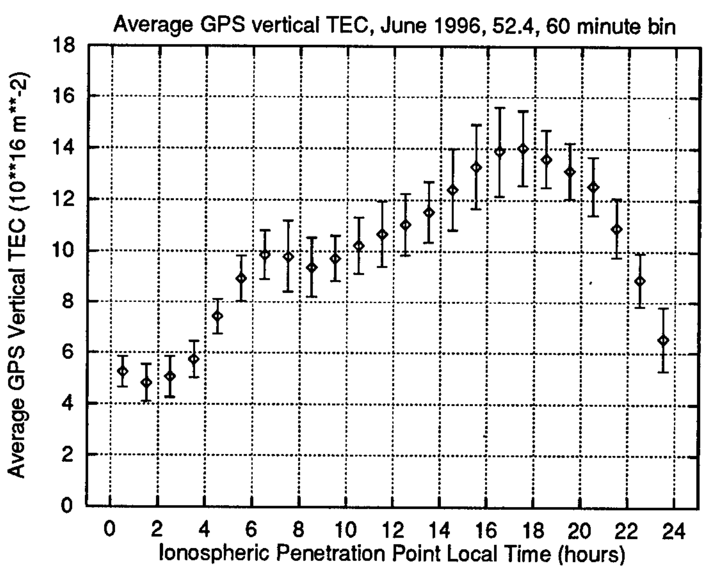

Fig. 4. Average GPS vertical TEC for the 21 days of data available in June 1996

looking at different ionospheric latitude bands using GPS, there is a contribution to each band from different L-shells. Those regions observed when looking in the overhead latitude band and that one degree to the north of Aberystwyth have been

grouped together as North measurements. Those regions observed when looking in a two degree latitudinal band to the south of the station have been grouped together as South measurements. It is expected that as GPS signals from the South region will have passed through lower protonospheric L-shells than those from the North region, so the protonospheric content to the South should exceed that to the North. Figure 3 shows the average of the difference between the GPS and NNSS vertical TEC measurements for the 21 days when both NNSS and GPS data were available in June 1996. The points with standard deviation error bars are those hourly average values where more than five NNSS passes were used to calculate the average. For observations to the South, the difference is always higher than for observations to the North, confirming the interpretation of the greater plasma content on the lower L-shells. A distinct minimum in the difference can be seen in the 8 to 10 IPP local time period, with maximum values apparently occurring well after midday, though lack of available NNSS passes limits the diurnal coverage of the plot. This variation in the value of the difference throughout the day does not relate directly to the average GPS values for the period shown in Fig. 4, which are dominated by the ionospheric variation.

Figure 5 shows the average of the difference between the GPS and NNSS vertical TEC data for 21 days of common measurements in November 1996. Here again for observations to the South the difference is always higher than for those to the North. The difference in electron content when looking to the South is generally about $4 \cdot 10^{16}\mathrm{m}^{-2}$ with little clear evidence of the form of a diurnal variation. However, in the period before midnight the differences looking North are much less then those of the South values. Results from a similar analysis for 27 days in December 1996 are shown in Fig. 6. The behaviour generally confirms that found in November, with larger separations between the two sets of measurements later in the day.

Another method of assessing the protonospheric contribution to the GPS observations is to perform a linear regression of GPS vertical TEC values on the corresponding NNSS TEC values. Equation (1) indicates that this linear fit should have a unity gradient and positive intercept. Figure 7 shows such an analysis for the data in the one degree latitude band above Aberystwyth in June 1996. It can be seen that the gradient in Fig. 7 is close to unity while the intercept is about $1.8 \cdot 10^{16}\ \mathrm{m}^{-2}$. Lines of unity gradient were fitted to the data for each monthly ionospheric latitude band and the intercepts calculated, the results of this analysis for June, November and December 1996 are shown in Fig. 8. It can be seen that the magnitude of the intercept increases with decreasing latitude. This result confirms the interpretation that ray paths at lower latitudes intersect flux tubes at lower L-shells containing proportionately greater electron content. It can also be noted that the values were greater in the winter months than for June.

The GPS measurements were made over a range of ionospheric latitudes so that it was possible to estimate the difference between the equivalent vertical GPS TEC for different latitude bands. The differences between the average GPS TEC for the band above Aberystwyth and those bands one degree to the south and to the north were obtained. The results plotted in Figs 9 and 10 are for June and December respectively, with error bars denoting the standard deviation of the

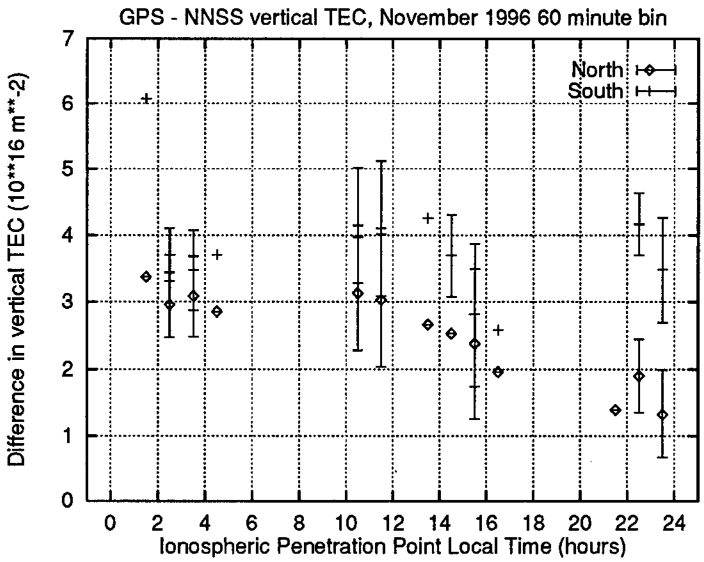

Fig. 5. Hourly average GPS minus NNSS vertical TEC for the 21 days of data available in November 1996

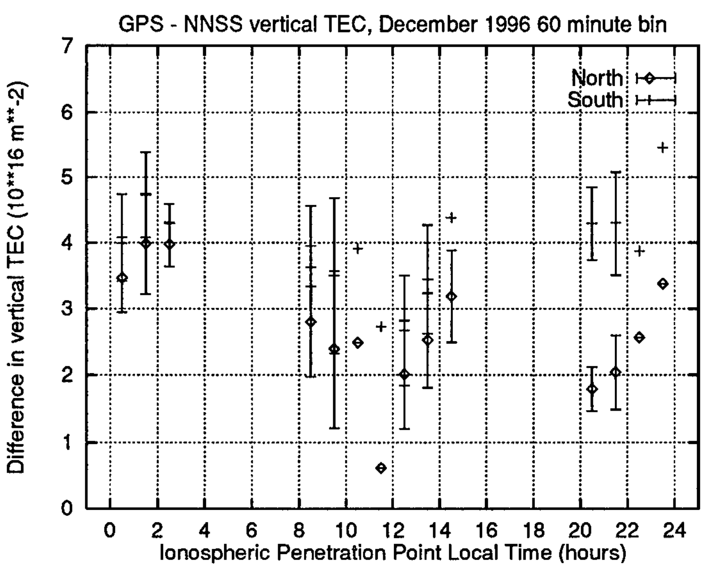

Fig. 6. Hourly average GPS minus NNSS vertical TEC for the 27 days of data available in December 1996

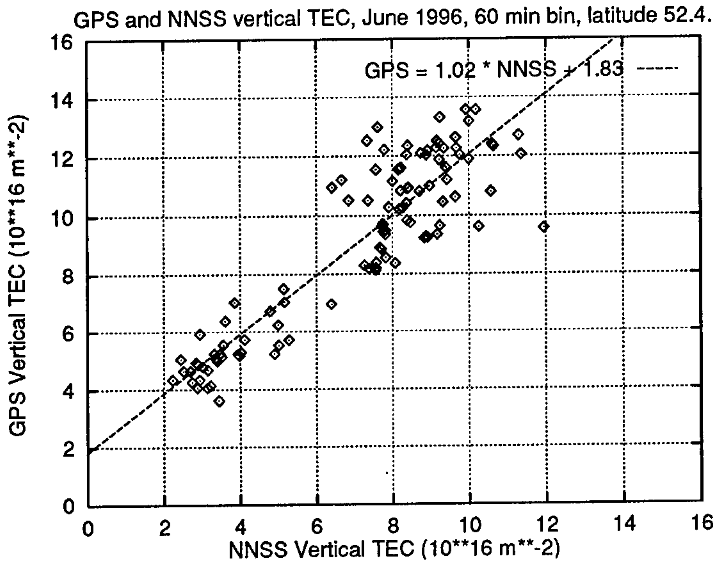

Fig. 7. Straight line fit through the GPS and NNSS vertical TEC values for data collected in June 1996 in the ionospheric latitude band over Aberystwyth

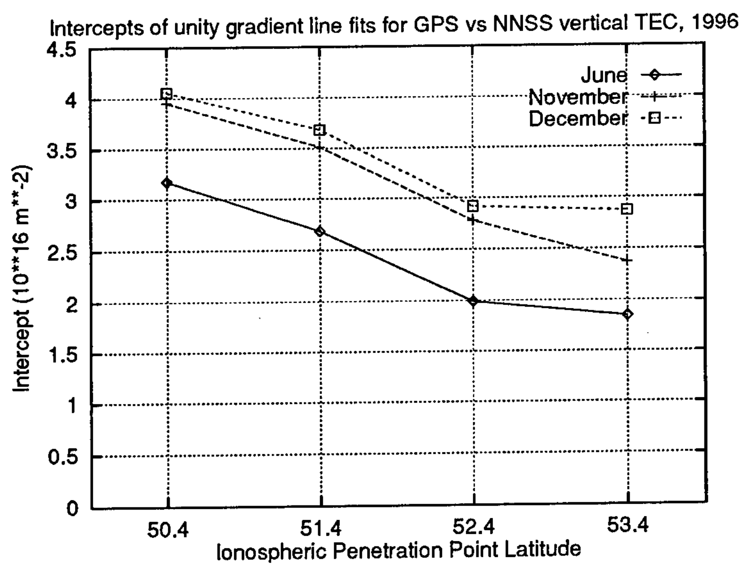

Fig. 8. Intercepts of unity gradient fits to NNSS vs GPS vertical TEC data for three months in 1996

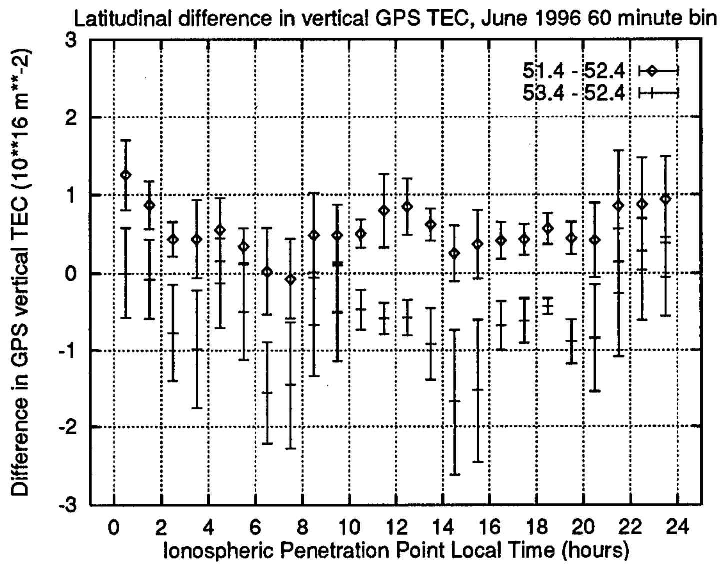

Fig. 9. Difference between the average GPS vertical TEC over Aberystwyth and the one-degree latitude bands to the north and south of the station for the 21 days of data available in June 1996

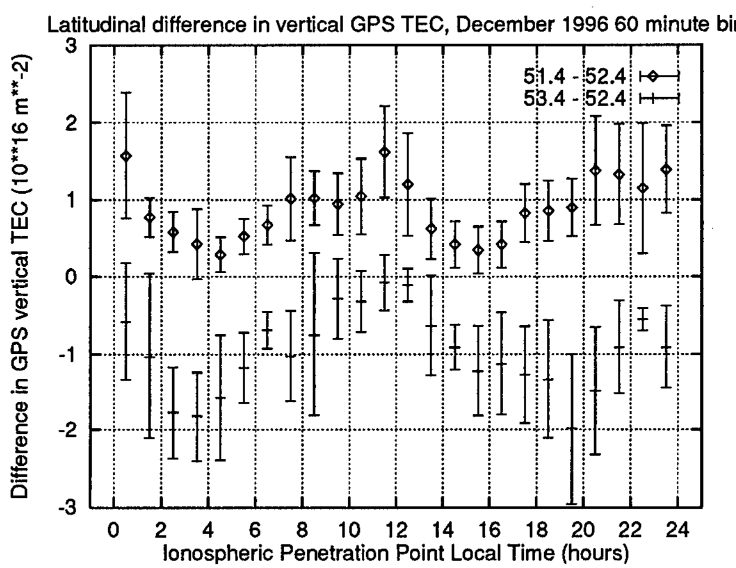

Fig. 10. Difference between the average GPS vertical TEC over Aberystwyth and the one-degree latitude bands to the north and south of the station for the 27 days of data available in December 1996

values. Again it can be seen that there is more electron content to the south, though it must be recognised that this estimate based on GPS measurements alone contains contributions from both ionospheric gradients and the influence of the protonosphere.

The results presented here are for solar minimum. It is possible that the protonospheric electron content may be greater at solar maximum so that better resolution of the difference in the vertical TEC between GPS and NNSS for the different latitudinal bands should become possible.

5. Conclusion

It has been shown that the difference between measurements of vertical TEC from GPS and NNSS satellites has the potential to monitor the electron content of the protonosphere. From this initial study it appears that the influence of the protonospheric electrons upon the GPS signals increases as the ionospheric intercept latitude of the GPS ray path decreases.

Studies of this kind are of importance not only to understand the physical behaviour of the protonosphere, but also for applications using GPS radio transmissions. For example, use of only a single frequency GPS signal for navigation purposes may require the effects of the ionosphere to be removed by an ionospheric model that has no protonospheric component. Further investigation is necessary to characterise the protonospheric electron content and its variation both for geophysical understanding and for propagation applications.

Acknowledgements

The work at Aberystwyth has been supported by the EOARD, London and the UK Particle Physics and Astronomy Research Council. Nicholas Lunt acknowledges support of a University of Wales, Aberystwyth Postgraduate Studentship.

References

Bishop G, Mazzella A, Holland E, Rao S 1996: In: Proceedings of IEEE 1996 Position Location and Navigation Symposium (PLANS), Atlanta, GA, USA, 145–152.

Hargreaves J K 1995: The Solar Terrestrial Environment: an Introduction to Geospace-the Science of the Terrestrial Upper Atmosphere, Ionosphere and Magnetosphere, Cambridge University Press, UK

Kersley L, Klobuchar J A 1978: *Geophys. Res. Lett.*, 5, 123–126.

Kersley L, Klobuchar J A 1980: *Planet. Space Sci.*, 28, 453–458.

Leitinger R, Schmidt G, Tauriainen T 1975: *J. Geophys.*, 41, 201–213.

Acta Geod. Geoph. Hung., Vol. 33(1), pp. 147–153 (1998)

A COMPARISON BETWEEN THE TEC COMPUTED USING GPS AND IONOSONDE MEASUREMENTS

R WARNANT[1] and J C JODOGNE[2]

At Dourbes (in Belgium), an ionosonde operated by the Royal Meteorological Institute of Belgium produces an electron concentration profile up to the maximum of the F2 layer. The Royal Observatory of Belgium has installed a Turbo Rogue GPS receiver on the same site. The ionosonde measurements are used to compute the ionospheric electron content (IEC) above Dourbes: in a first step, numerical integration of the measured bottomside electron concentration profile gives the bottomside part and in a second step, analytical integration of a Chapman function modelling the topside electron concentration profile gives the topside part; the parameters of the Chapman function are evaluated using the information contained in the measured bottomside profile. This IEC is compared with the TEC obtained by GPS on a period of 2 years (1995 and 1996). We show that the results of both methods are in very good agreement: the mean and the standard deviation of the differences between the TEC (GPS) and the IEC (ionosonde) computed for this period are respectively 0.46 TECU and 1.72 TECU.

Keywords: GPS; ionosonde; ionosphere; TEC; total electron content

1. Introduction

A long time ago, the dual frequency radio signals emitted by the NNSS satellites have been used to measure the total electron content (Leitinger 1975). As these satellites are reaching the end of their life, geophysicists have to rely on another way to compute the TEC.

GPS code and phase measurements can also be processed in order to estimate the TEC with a precision of 2–3 TEC units (Warnant 1997).

At Dourbes (Belgium), a Turbo Rogue GPS receiver is collocated with an ionosonde operated by the Royal Meteorological Institute of Belgium. In this paper, we make use of this collocation to compare the GPS TEC with the ionospheric electron content (IEC) obtained from ionosonde measurements. The results of the comparison between two completely independent methods gives an indication of the GPS TEC accuracy.

2. GPS TEC determination

At the Royal Observatory of Belgium, a procedure has been developed in order to compute the TEC from GPS measurements. This method is explained in details in Warnant (1996) and Warnant (1997). In this paragraph, we only summarize the main steps of the procedure.

[1]Royal Observatory of Belgium, Avenue Circulaire 3, B–1180 Brussels, Belgium, e-mail: R.Warnant@oma.be

[2]Royal Meteorological Institute, Avenue Circulaire 3, B–1180 Brussels, Belgium, e-mail: J-C.Jodogne@oma.be

The TEC computation procedure is based on the so-called geometry-free combinations of GPS code ($P^i_{p,GF}$) and phase ($\Phi^i_{p,GF}$) measurements:

$$P^i_{p,GF} = P^i_{p,L1} - P^i_{p,L2} \tag{1}$$

$$\Phi^i_{p,GF} = \Phi^i_{p,L1} - \frac{f_{L1}}{f_{L2}}\Phi^i_{p,L2} \tag{2}$$

with
$P^i_{p,L1}$, $P^i_{p,L2}$ the $L1$, $L2$ code measurements made by receiver p on satellite i;
$\Phi^i_{p,L1}$, $\Phi^i_{p,L2}$ the $L1$, $L2$ carrier phase measurements made by receiver p on satellite i;
f_{L1}, f_{L2} the frequency of the $L1$, $L2$ carriers.

These equations can be rewritten in function of the total electron content, TEC^i_p:

$$P^i_{p,GF} = -1.05 \cdot 10^{-17}\mathrm{TEC}^i_p + (DG_p - DG^i) \tag{3}$$

$$\Phi^i_{p,GF} = -5.52 \cdot 10^{-17}\mathrm{TEC}^i_p + N^i_{p,GF} \tag{4}$$

with
$N^i_{P,GF}$ a real ambiguity;
TEC^i_p slant TEC measured along the path going from satellite i to receiver p;
DG^i, DG_p the satellite i and receiver p differential group delays.

In practice, the TEC is extracted from Eq. (4); the ambiguity $N^i_{P,GF}$ is solved with the following combination of geometry-free code and phase measurements:

$$P^i_{p,GF} - \lambda_{L1}\Phi^i_{p,GF} = (DG_p - DG^i) - \lambda_{L1}N^i_{p,GF} \tag{5}$$

with λ_{L1} the $L1$ carrier wavelength.

To be able to solve the ambiguity $N^i_{P,GF}$ from Eq. (5), we have to estimate the so-called receiver and satellite differential group delays; the existence of these biases is due to the fact that the two GPS frequencies undergo different propagation delays inside the receiver and satellite hardware. The uncertainty on these biases is the largest error encountered when computing the TEC with GPS measurements; they are obtained from Eq. (3) where the TEC is modelled by means of a simple polynomial in latitude and local time. In this procedure, we assume that the ionosphere is a layer of infinitesimal thickness located at a height of 350 km; the intersection between the satellite line of sight and this layer is called the ionospheric point; as GPS satellites are observed with different elevation angles, the TEC values computed using GPS measurements are representative of the state of the ionosphere at the ionospheric points. All these ionospheric points have a latitude and a longitude (or a local time). For this reason, GPS measurements allow to compute TEC profiles in function of latitude and longitude (or local time). For example, 24 hours of observations collected at Brussels in Belgium (latitude = 50.8°N, longitude = 4.4°E) allow to compute the TEC from 35° to 60°N in latitude and from 20°W to 25°E in longitude.

In this work, we compare the TEC obtained using GPS observations and vertical sounding measurements. For this reason, we have to compute a GPS TEC value representative of the ionosphere above the observing GPS station. In order to do that, we apply the following procedure:

1. We select all the TEC values corresponding to an ionospheric point of which the latitude, L_{iono}, is given by:

$$L_{\text{sta}} - 1.5^\circ \leq L_{\text{iono}} \leq L_{\text{sta}} + 1.5^\circ$$

   with L_{sta}, the latitude of the observing station.

   As the height of the ionospheric point is 350 km, this selection means that we restrict the geographic dispersion to ±175 km from the ionospheric station. This is to be compared with the correlation distance of ±200 km generally admitted in ionospheric studies.

2. We compute the mean of all these TEC values for 15 minute periods.

3. Ionospheric electron content computation

An ionosonde measures, $N(h)$, the electron concentration profile as a function of the altitude, h, up to the peak of the F2 layer. This part is called the bottomside profile; the electron concentration profile above the peak of the F2 layer is called the topside profile. As the topside profile cannot be measured by the ground-based ionosonde, it has to be modelled up to the altitude of the GPS satellites (i.e. 20 200 km).

Several analytical functions were tried: parabola, Epstein functions, Chapman functions. The determination of the function parameters is not trivial as no protonosphere indice is internationally recognised. The use of information from the bottomside seems to give adequate results (Wang et al. 1994). The simplest way is to normalize the function by the value of the maximal concentration. The Epstein and Chapman functions appear to give very similar results as they produce almost the same profile. In practice, the topside profile, $N_T(h)$, is modelled using a Chapman function as it is "more" related to the physics:

$$N_T(h) = N_{\max} \exp(1 - z - \exp(-z))$$

with
$z = \dfrac{(h - h_{\max})}{H_T}$
$h_{\max}$, $N_{\max}$ the altitude and the density at the maximum of the F2 Layer
H_T is the topside profile scale height.

The remaining parameter, the scale height, is obtained using information coming from the bottomside profile. Many ways to fix it were explored. The method adopted takes care of the fact that near the top, the scale height does not change significantly as the temperature remains constant. H_T is chosen as the mean of the scale heights computed at 3 points of the bottomside profile: these points are located at 88%, 90% and 92% of $N_{\max}$.

4. Results

GPS and ionosonde derived TEC have been compared in a period of 2 years (1995 and 1996). Figures 1 and 2 show GPS and ionosonde TEC for 6 days. All the differences TEC (GPS) minus IEC (ionosonde) for the years 1995 and 1996 are plotted in Fig. 3. Figure 4 shows that these differences are normally distributed. The mean and the standard deviation of these differences computed for these two years are respectively 0.46 TECU and 1.72 TECU.

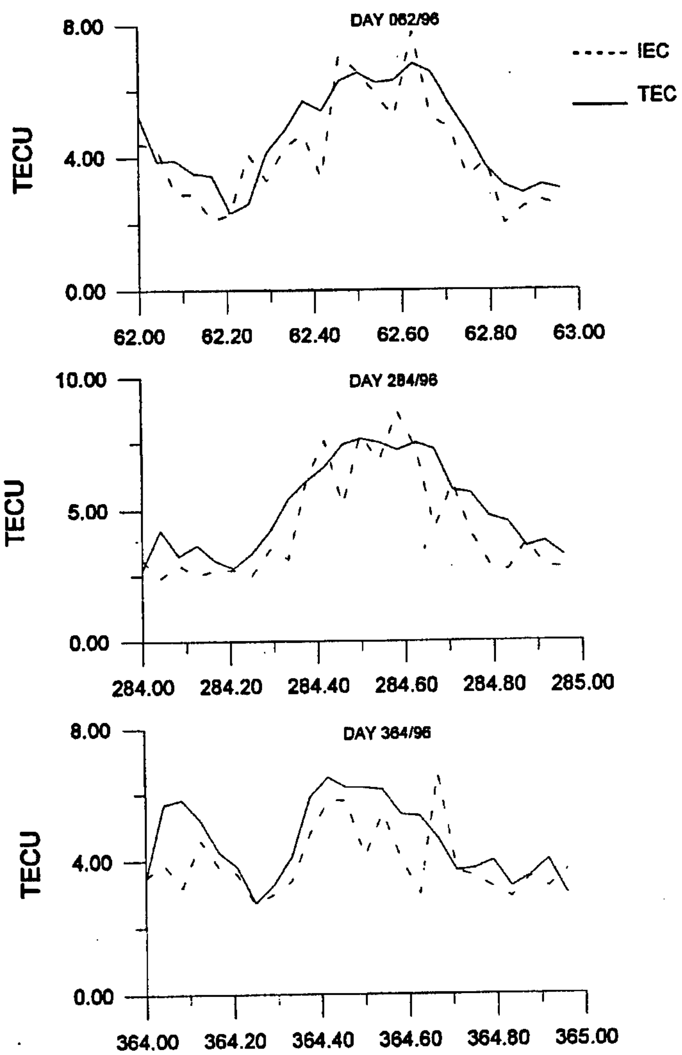

Fig. 1. Comparison between TEC and IEC for 3 days (days of year 062, 284, 364) in 1996

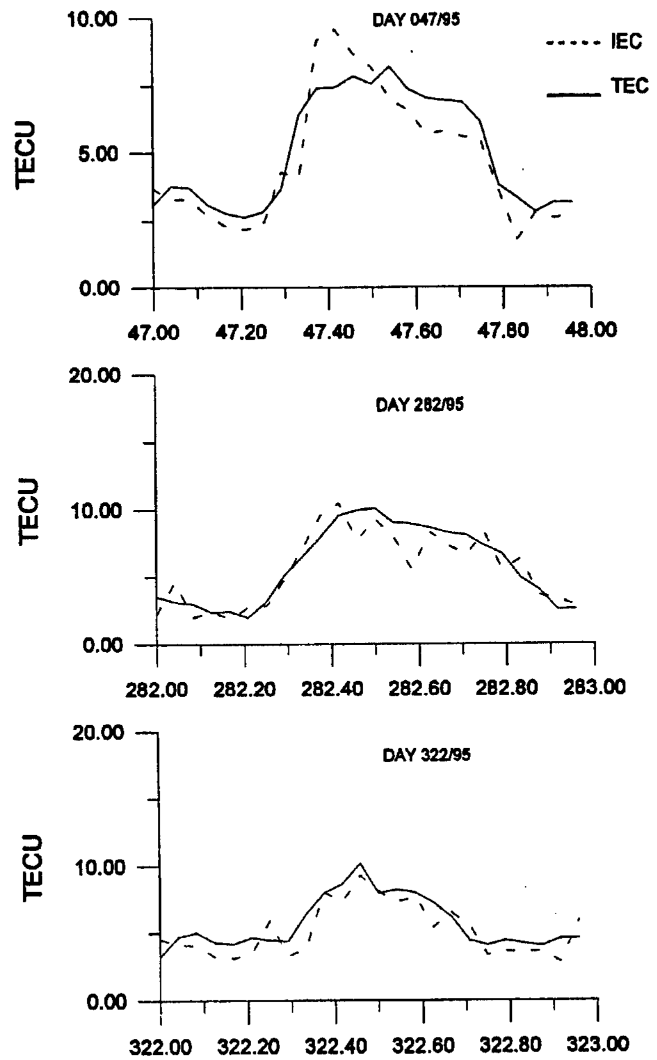

Fig. 2. Comparison between TEC and IEC for 3 days (days of year 047, 282, 322) in 1995

5. Conclusions

In this paper, we give an estimation of the GPS TEC accuracy by comparing it with the IEC computed from ionosonde measurements: the mean and the standard deviation of the differences TEC-IEC computed for two years (1995 and 1996) are respectively 0.46 TECU and 1.72 TECU. The IEC is obtained by integration of the electron concentration profile up to the altitude of the GPS satellites. The bottomside profile is measured by the ionosonde; the topside profile is modelled by a Chapman function; the parameters of this function are computed from information measured by the ionosonde:

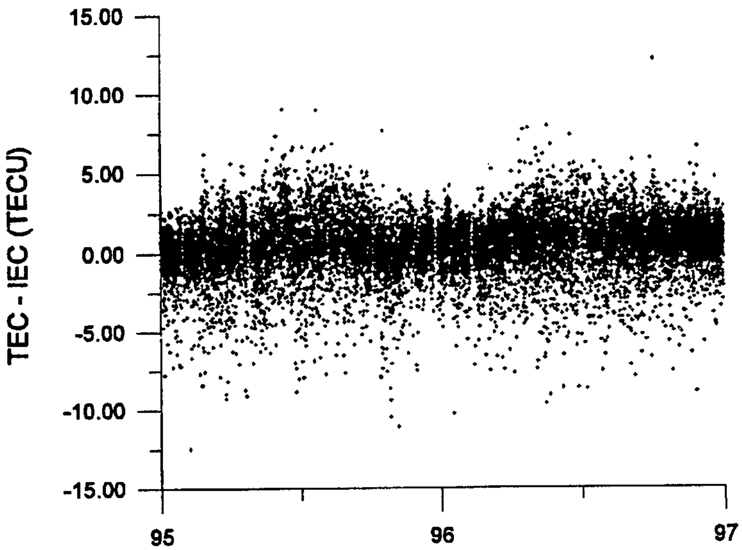

Fig. 3. Difference TEC-IEC during 2 years

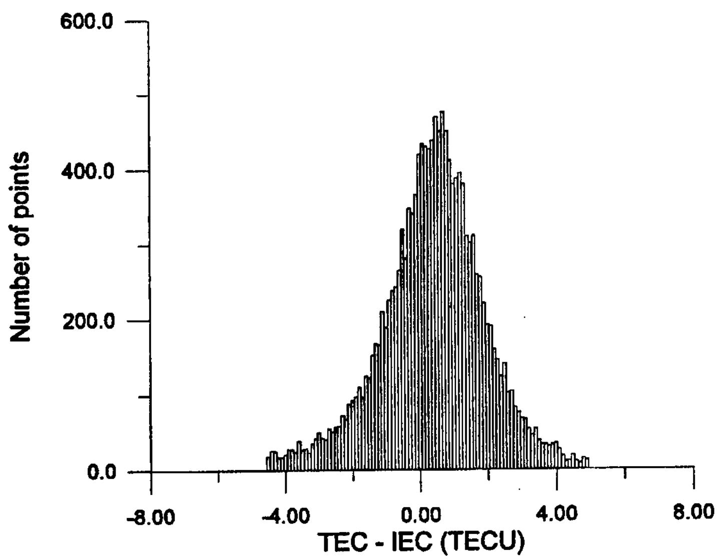

Fig. 4. Distribution of the differences TEC-IEC

1. the scale height is chosen as the mean of the scale heights computed at 3 points of the bottomside profile: these points are located at 88%, 90% and 92% of $N_{\max}$.
2. The function is normalized by the value of maximal concentration.

References

Lanyi G E, Roth T 1988: *Radio Science*, 23, 483–492.

Leitinger R, Schmidt G, Taurianen A 1975: *J. Geoph. Res.*, 41, 201–213.

Wang C, Huang X, Reinisch B, Klobuchar J 1994: In: Proceedings of Beacon Satellite Symposium '94, L Kersley ed., Univ. of Aberystwyth, U.K., 290–293.

Wanninger L, Sardón E, Warnant R 1994: In: Proceedings of Beacon Satellite Symposium '94, Dépt. of Physics of University of Aberystwyth ed., 13–16.

Warnant R 1996: Etude du comportement du Contenu Electronique Total et de ses irrégularités dans une station de latitude moyenne. Application aux calculs de positions relatives par le GPS, Ph.D. Thesis (in French), Série Géophysique (No. Hors-Série) de l'Observatoire Royal de Belgique, Bruxelles

Warnant R 1997: Reliability of the TEC computed using GPS measurements. The problem of hardware biases. *Acta Geod. Geoph. Hung.* (present issue)

INSTRUCTIONS TO AUTHORS

Manuscripts should be sent to the Editorial Office (address see above). Articles not published or submitted for publication elsewhere are only accepted.

Manuscripts should be typewritten in duplicate or on disk (LATEX*.tex files or Word for Windows Documents or text-only ASCII files) with a written copy, or via E-mail (LATEX*.tex files or text-only ASCII files).

Manuscripts should include the following components which should be presented in the order listed (tables and illustrations should be separated in case of manuscripts on disk, too).

1. Title, name(s) of the author(s), affiliation, dateline, abstract, keywords
2. Text, acknowledgements
3. References
4. Footnotes
5. Legends
6. Tables
7. Illustrations

1. The *affiliation* should be as concise as possible and should include the complete mailing address of the authors. The *date of receipt* will be supplied by the editors. The *abstract* should not exceed 250 words and should clearly and simply summarize the most important methods and results. 5–10 significant expressions describing the content are used as *keywords.* Authors may recommend these keywords.

2. The *text* should be in English and as short and clear as possible. In case of typewritten manuscripts, please note the following:

— avoid possible confusion between o, O (letters) and 0 (zero), l (letter) and 1 (one), ν (Greek nu) and u, v (letters), etc.
— explain ambiguous and uncommon symbols by making marginal notes in pencil
— formulas are to be numbered consecutively with the number in parentheses to the right of the formula. Text references to the equations may then be made by the number in parenthesis. The word equation in this context is to be abbreviated to Eq. and Eqs in the plural
— the International System of Units (SI) should be used.

3. *References* are accepted only in the Harvard system. Citations in the text should be as:

...(Bomford 1971)...or Bomford (1971)...

...(Brosche and Sündermann 1976)...

...(Gibbs et al. 1976b)...

The list of references should contain names and initials of all authors (the abbreviation et al. is not accepted here): for journal articles, year of publication, the title of the journal in abbreviated form, volume number, first and last page. For books or chapters in books, the title is followed by the publisher and place of publication.

All items must appear both in the text and in the list of references.

4. *Footnotes* should be typed on separate sheets.

5. *Legends* should be short and clear. The place of the tables and figures should be indicated in the text, on the margin.

6. *Tables* should be numbered serially with Roman numerals. Vertical lines are not used.

7. All the *illustrations* should contain the figure number and author's name in pencil on the reverse. The most important point with figures is clearness. Photographs and half-tone illustrations should be sharp and well contrasted. Colour photographs will be accepted, but the extra cost of reproduction in colour must be borne by the authors (approx. US$ 280 per page).

Only original papers will be published and a copy of the Publishing Agreement will be sent to the authors of papers accepted for publication. Manuscripts will be processed only after receiving the signed copy of the agreement. Information is sent to the first author if no other wish is expressed.